Ultra-thin solid oxide fuel cells: materials and devices

A dissertation presented

By

Kian Kerman

to

The School of Engineering and Applied Sciences

In partial fulfillment of the requirements

for the degree of

Doctor of Philosophy

in the subject of

Applied Physics

Harvard University

Cambridge, Massachusetts

April 2014

Shriram Ramanathan **Kian Kerman**

Ultra-thin solid oxide fuel cells: materials and devices

ABSTRACT

Solid oxide fuel cells are electrochemical energy conversion devices utilizing solid electrolytes transporting O^{2-} that typically operate in the 800 – 1000 °C temperature range due to the large activation barrier for ionic transport. Reducing electrolyte thickness or increasing ionic conductivity can enable lower temperature operation for both stationary and portable applications. This thesis is focused on the fabrication of free standing ultrathin (<100 nm) oxide membranes of prototypical O^{2-} conducting electrolytes, namely Y_2O_3-doped ZrO_2 and Gd_2O_3-doped CeO_2. Fabrication of such membranes requires an understanding of thin plate mechanics coupled with controllable thin film deposition processes. Integration of free standing membranes into proof-of-concept fuel cell devices necessitates ideal electrode assemblies as well as creative processing schemes to experimentally test devices in a high temperature dual environment chamber. We present a simple elastic model to determine stable buckling configurations for free standing oxide membranes. This guides the experimental methodology for Y_2O_3-doped ZrO_2 film processing, which enables tunable internal stress in the films. Using these criteria, we fabricate robust Y_2O_3-doped ZrO_2 membranes on Si and composite polymeric substrates by semiconductor and micro-machining processes, respectively. Fuel cell devices integrating these membranes with metallic electrodes are demonstrated to operate in the 300 – 500 °C range, exhibiting record performance at such temperatures. A model combining physical transport of electronic carriers in an insulating film and electrochemical aspects of transport is developed to determine the limits of performance enhancement expected via electrolyte thickness

reduction. Free standing oxide heterostructures, i.e. electrolyte membrane and oxide electrodes, are demonstrated. Lastly, using Y_2O_3-doped ZrO_2 and Gd_2O_3-doped CeO_2, novel electrolyte fabrication schemes are explored to develop oxide alloys and nanoscale compositionally graded membranes that are thermomechanically robust and provide added interfacial functionality. The work in this thesis advances experimental state-of-the-art with respect to solid oxide fuel cell operation temperature, provides fundamental boundaries expected for ultrathin electrolytes, develops the ability to integrate highly dissimilar material (such as oxide–polymer) heterostructures, and introduces nanoscale compositionally graded electrolyte membranes that can lead to monolithic materials having multiple functionalities.

TABLE OF CONTENTS

LIST OF KEY SYMBOLS

Symbol	Descriptor	Units
V_{OC}	open circuit voltage	V
R	universal gas constant	J/(mol K)
T	temperature	°C or K
n	number of electrons transferred	-
F	Faraday's constant	C/mol
σ_i	ionic conductivity	S/cm
E_a	activation energy	J or eV
E	electric field	V/cm
k	Boltzmann constant	eV/K
j	current density	A/cm^2
η_a	activation overpotential	V
η_Ω	Ohmic overpotential	V
η_c	concentration overpotential	V
α	charge transfer coefficient	-
D	diffusion coefficient	cm^2/s
h	electrolyte thickness	m
V	voltage	V
σ_0	residual film stress	Pa
σ_{TM}	thermo-mechanical stress	Pa
E_m	elastic modulus	Pa
υ	Poisson's ratio	-
σ_e	electronic conductivity	S/cm

Acronym	Full name
SOFC	solid oxide fuel cell
MCFC	molten carbonate fuel cell
PAFC	phosphoric acid fuel cell
PEMFC	polymeric electrolyte membrane fuel cell
AFC	alkaline fuel cell
YDZ	yttria-doped zirconia
GDC	gadolina-doped ceria
OCV	open circuit voltage
TPB	triple phase boundary
MEMS	micro-electromechanical system
SEM	scanning electron microscopy
TEM	transmission electron microscopy
XRD	x-ray diffraction
XRR	x-ray reflectivity
SAED	selected area electron diffraction
LSCF	$La_{0.6}Sr_{0.4}Co_{0.8}Fe_{0.2}O_{3-\delta}$
BSCF	$Ba_{0.5}Sr_{0.5}Co_{0.8}Fe_{0.2}O_{3-\delta}$
XPS	x-ray photoelectron spectroscopy

LIST OF FIGURES

ACKNOWLEDGEMENTS

The PhD is a long journey, which if done correctly, directs one towards an unwavering path of intellectual enlightenment. In traveling the winding road to this dissertation I am indebted to my ever supportive academic guides David Clarke, Mike Aziz, Frans Spaepen, and most importantly my advisor, Shriram Ramanathan. The technical assistance behind my development is the result of mentorship from past group members (Bo-Kuai Lai, Changhyun Ko, and Quentin Van Overmeere), center for nanoscale systems staff members (David Bell, Adam Graham, and Yuan Liu), associates at Rutgers (William Simon, Koray Akdogan, and Ahmad Safari), and John Baniecki at Fujitsu laboratories. I am proud to have published with many of these scholars. I thank the members of the Ramanathan group for their assistance during this work.

Logistically, the diligence of the group administrator (LaShanda Banks) and academic office staff (Tricia Jacome, Lisa Frazier, and William Walker) is truly appreciated.

Funding from the Department of Defense through the NDSEG program and the National Science Foundation (grant no. CCF-0926148) is gratefully acknowledged.

My graduate school experience would not be whole without talented and well-rounded colleagues (Brian Huskinson, Adrian Podpirka, William Bonificio, Roger Diebold, Matt Pharr, Sieu Ha, and Rafael Jaramillo) that made classes, research, and everything in between more pleasant.

To the Jersey crew that has unconditionally supported me through this period, my gratitude is simply inexpressible. To Mom and Bita, you have been the light escorting me forward.

In the end, none of this is quite as important as it may have once seemed.

For my father

Page intentionally left blank.

1 INTRODUCTION

1.1 Background

The greenhouse effect, first hypothesized by Svante Arrhenius in 1896, states that changes in CO_2 levels in the atmosphere could substantially alter the earth's surface temperature.[1] According to the Intergovernmental Panel on Climate Change in the time period between 1970 and 2004, CO_2 annual emissions have increased by over 80%.[2] This increase is primarily associated with the usage of fossil fuels, commonly designated for electricity generation, automotive transport, and commercial applications. The most common method of electricity generation is by combustion of fuels, generating heat, which is then used to drive a mechanical turbine thereby generating electrical energy from stored chemical energy as depicted in Figure 1.[3] For example, the combustion of natural gas, which is mostly comprised of methane (CH_4), is given by $CH_4 + 2O_2 \rightarrow 2H_2O + CO_2$. This reaction is largely exothermic and can drive the mechanical turbine by heating a boiler. Internal combustion engines operate on a similar principle, albeit directly converting chemical energy directly mechanical energy.

Figure 1- 1: General diagram for electricity production

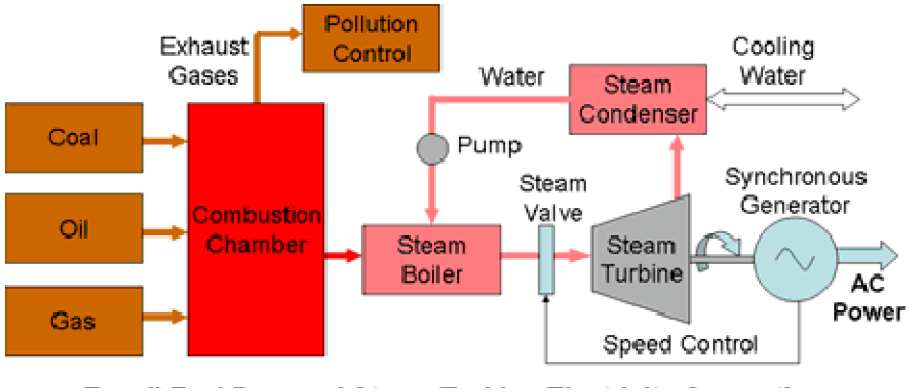

A high level engineering flow diagram depiction of the components used during electricity generation.[3]

Due to energy transfer during the chemical-mechanical-electrical transfers, these processes are inherently limited by thermodynamics and therefore the most efficient sequence, the Carnot cycle. This cycle consists of two isothermal processes and two adiabatic processes, resulting in a metric of theoretical efficiency given by $\eta_{Carnot} = \frac{T_H - T_C}{T_H}$ where T_H and T_C represent the high and low temperatures in the process, respectively. For the example in Figure 1, these would correspond to the boiler and condenser temperatures, respectively. Currently, state of the art electricity power plants operate at approximately 35 – 45% efficiency,[4] limited by the thermal reservoirs. They also produce harmful anthropogenic gases as by-products.

Fuel cells are devices that electrochemically convert chemical energy sources directly to electricity, first introduced in 1839 by Sir William Grove.[5] They are not limited by the thermodynamic limitations described above. Therefore, the theoretical efficiency (η_{FC}) can be simply expressed the ratio of useful work extracted to heat input, $\eta_{FC} = \frac{\Delta G}{\Delta H}$. For natural gas, the net electrochemical reaction is the same as that of combustion, though there is direct energy transfer. Using tabulated thermodynamic data,[6] this process has a theoretical conversion efficiency of 92%. In practice, efficiencies of fuel cells range from 40 – 60%.[7] The deviation from theoretical efficiency is due to intrinsic loss mechanisms in fuel cells and large scale system considerations. There are many variations of fuel cells, though the operation principals are similar. Figure 2 shows a diagram of the types of fuel cells that have been of particular relevance thus far.[8] This thesis and associated experimental work is focused on SOFCs.

Figure 1- 2: Types of fuel cells

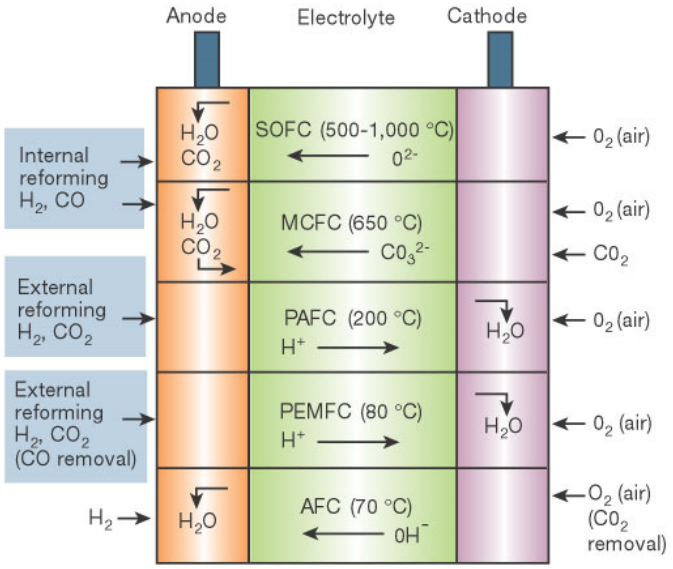

Fuel cells are often characterized by the mobile ionic species in the electrolyte and active temperature range.[8] *Figure used with permission from Nature publishing group.*

1.2 Principles of solid oxide fuel cells

As shown in Figure 2, all fuel cells operate with three components, namely an anode, cathode, and electrolyte. The anode and cathode are electrodes having nomenclature derived from the Greek 'anodos' and 'kathodos' which mean 'a way up', and 'descent', respectively. This nomenclature refers to the migration of electronic charge carriers in the electrodes. Hence, the anode typically preforms oxidation where electrons leave the electrode, while the reduction occurs at the cathode and electrons flow into the electrode. SOFCs are differentiated by transport of O^{2-} through the solid oxide electrolyte and subsequent high temperature regime of operation. They have traditionally been targeted for large scale energy production (kW – MW), for stationary applications. In addition, ultrathin membrane based electrolytes developed in this thesis open possible applications in the mobile space, discussed in Section 1.3.

1.2.1 Oxygen transport

Ionic transport was first observed by Walther Nernst in 1900,[9] and later understood from a fundamental atomic perspective by Carl Wagner.[10] In a cubic crystal or polycrystalline materials, such as those in this thesis, ionic conductivity reduces from a tensor quantity to a scalar and can simply be expressed by $\sigma_i = \left(\frac{A}{T}\right) \exp\left(\frac{-E_a}{kT}\right)$ where A is a material specific constant and E_a is an activation barrier.[11] This relationship follows from Ohm's law for oxygen vacancy conduction, $\sigma_i E = n_v N q v_i$, where E is electric field, n_v is the fraction of vacant sites, N is the number of sites per unit volume, $q = 2e$, the charge of an oxygen vacancy moving, and v_i is the velocity of the carrier. Using the fact that ionic mobility (μ_i) is defined as $\mu_i = \frac{v_i}{E}$ and the Nernst-Einstein relationship allows the derivation of the aforementioned expression for σ_i, which importantly indicates a direct correlation of σ_i with vacancy concentration and an exponential dependence on temperature. This is the main reason for tailoring doped oxide materials and the operation of SOFCs at elevated temperatures up to 1000 °C, respectively. Figure 3 shows a survey of some typical O^{2-} conductors for reference.[12]

Figure 1- 3: Oxygen ion conductivity of select materials

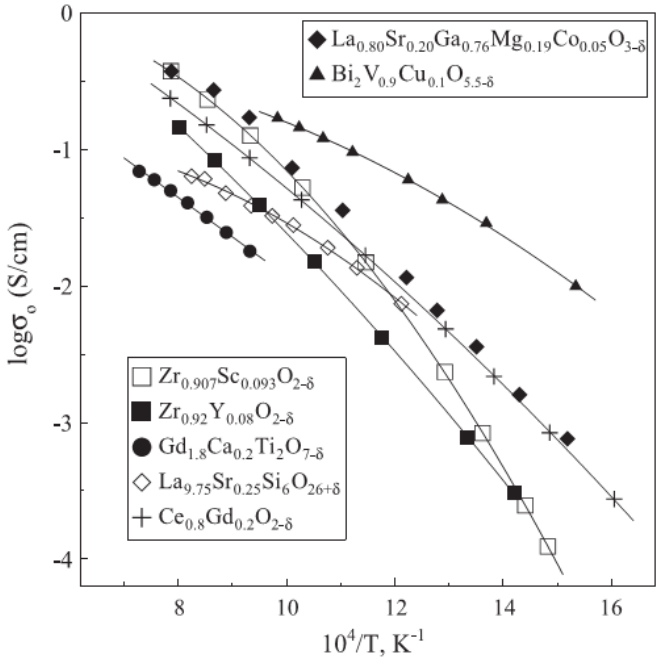

An Arrhenius plot showing the oxygen ion conductivity of several oxide materials. Plotted in this fashion, the slope of these curves represents the activation barrier E_a *in the text. Figure used with permission from Elsevier.*

The SOFC electrolyte must operate across a varying chemical potential due to the oxygen partial pressure (p_{O_2}) range between the anode and the cathode. Typical operation conditions result in environments of $10^{-19} < p_{O_2} < 10^{-1}$ atm. Therefore, in order to satisfy the requirement of remaining electronically insulating, the electrolyte must remain in the electrolytic domain, i.e. the electronic conductivity should not strongly depend on temperature or p_{O_2}. This type of conduction behavior can be visualized in a Brouwer diagram shown in Figure 4.[13]

Figure 1- 4: Oxide Brouwer diagram

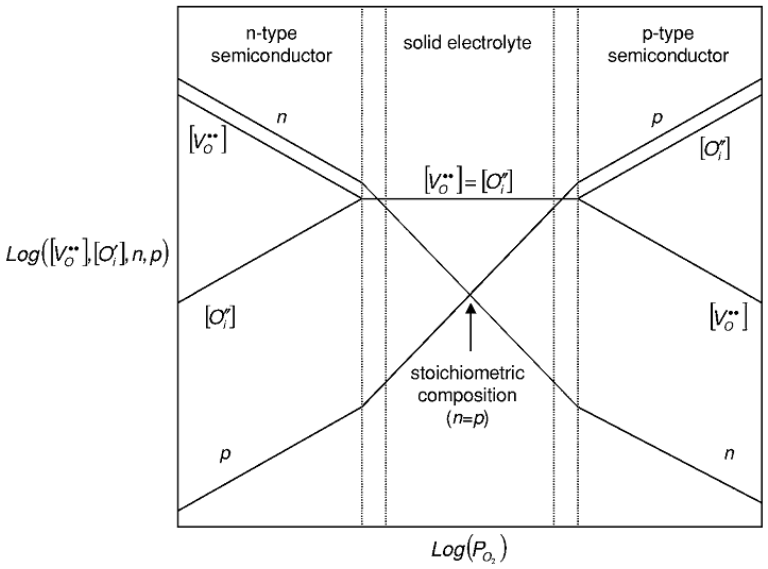

A general Brouwer diagram that summarizes the behavior of defects as a function of environment in an oxide with intrinsic anion Frenkel defects (oxygen leaves lattice site and sits at an interstitial site). Figure used with permission from Springer publishing.

Aliovalently doped ZrO_2 is one of the most widely studied solid electrolyte systems as it is known to have a wide electrolytic domain and is mechanically resilient under harsh environments. ZrO_2 takes the cubic fluorite structure, with Zr remaining in the 4^+ valence at the 8 coordinated sites. Doping of 3^+ cations of comparable ionic radius, such as Y_2O_3, results in an increase in the number vacant oxygen lattice sites as a result of the electroneutrality condition, $Y_2O_3 \xrightarrow{ZrO_2} 2Y'_{Zr} + 3O_o + V_O^{\cdot\cdot}$; which can maximize the overall σ_i at optimal doping concentrations.[14] Dopant concentrations above the ideal fraction can lead to vacancy ordering and hinder σ_i.[15] As shown in Figure 3 a wide variety of oxygen-ion conductors exist, each having its own merits and pitfalls.[12, 16] This thesis is primarily concerned with the physical scaling of Y_2O_3-doped ZrO_2 (YDZ) and Gd_2O_3-doped CeO_2 (GDC), as they are classic electrolyte materials well studied in bulk form. GDC is similar in structure and electroneutrality conditions of the dopant, but exhibits an ionic conductivity

nearly an order of magnitude higher than YDZ over a similar temperature range. However, unlike YDZ, GDC has a narrower electrolytic domain owing to the stability and co-existence of Ce^{3+} and Ce^{4+}.[17, 18] This aspect in relation to experimental study and electrolyte functionality is discussed in Chapter 5.

1.2.2 Fuel cell characteristics

While the materials, environments, and power output of particular fuel cells may vary, the electrical characteristics are similar. A typical fuel cell current-voltage curve is shown in Figure 5, showing the key loss mechanisms that contribute to reduced operating efficiency.

Figure 1- 5: Typical fuel cell current-voltage curve

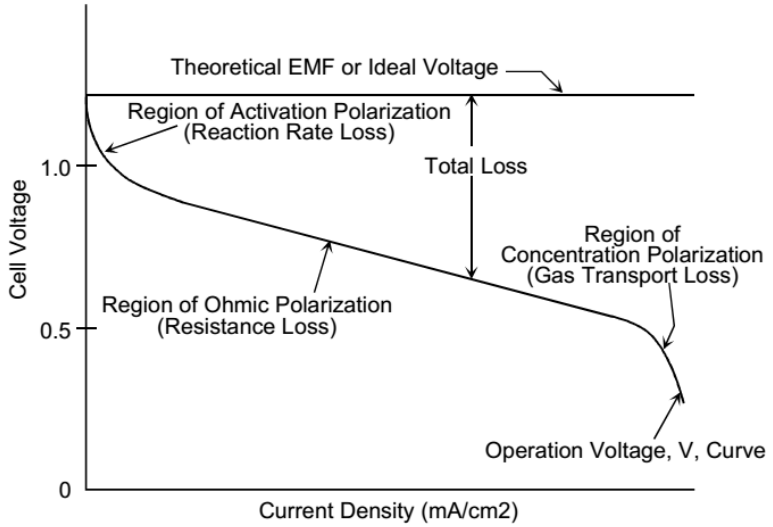

The three main loss mechanisms of fuel cells are depicted in this plot, showing deviation from the expected ideal voltage as a function of extracted current density.

For an ideal fuel cell with a known redox couple, the OCV is modified by the operating conditions through the Nernst equation. For an example relevant to SOFCs with gaseous hydrogen and oxygen, $V_n = V_{OC} + \frac{RT}{nF}\ln\left(\frac{p_{H_2}\sqrt{p_{O_2}}}{p_{H_2O}}\right)$ where V_{OC} is the equilibrium voltage for a given redox couple

under standard partial pressures; R, T, n, and F represent the universal gas constant, temperature, number of electrons transferred, and Faraday's constant, respectively. For a SOFC operating at high temperature having reactant activities of 1, partial pressures of hydrogen (p_{H_2}), oxygen (p_{O_2}), and water vapor (p_{H_2O}) are used for the gaseous species. As shown, when current is driven from the cell this voltage decays from the expected value. The three components of loss are predominantly related to the three aforementioned physical components of the cell, i.e. the cathode, electrolyte, and anode. Therefore, cell voltage can be expressed by, $V_{cell} = V_n - \eta_a - \eta_\Omega - \eta_c$, where V_n is the Nernst potential, and η_a, η_Ω, and η_c are voltage losses (i.e. overpotentials) corresponding to the activation, Ohmic, and concentration processes, respectively. Each of the components is described in the following sub-sections.

1.2.3 Activation overpotential

The activation overpotential is the first loss encountered when driving current in the fuel cell. It is related to the potential barrier for driving a particular electrochemical reaction at the cathode surface which originates from charge transfer processes. From the most general perspective, the relationship between driving voltage and subsequent kinetic reaction rate, thus electronic current, can be expressed by the concentration independent Butler-Volmer equation,[19-21] $\eta_a = \left(\frac{RT}{n\alpha j_{0,c}}\right)\ln\left(\frac{j}{j_{0,c}}\right) - \left(\frac{RT}{n(1-\alpha)j_{0,a}}\right)\ln\left(\frac{j}{j_{0,a}}\right)$. In this formalism, n, j, and α represent the number of electrons transferred in the process, current density, and charge transfer coefficient, respectively. α is a measure of the symmetry of the potential barrier which faces the forward and reverse electrochemical reaction and takes a value of 0.5 for an ideally symmetric relationship.[22] The exchange current density, j_0, is a measure of the current that flows for a given reaction on a particular electrode when there is no driving voltage. Therefore it can take different values at the

anode, $j_{0,a}$, and cathode, $j_{0,c}$. This value is dependent on the catalyst material, ambient atmosphere, and reactant. It can be experimentally determined using a Tafel plot, which is a linear approximation at large overpotential values of the Butler-Volmer equation.[23] In summary, the activation loss occurs at low driving voltages and is strongly dependent on the reactant/catalyst interface.

1.2.4 Ohmic overpotential

The Ohmic overpotential is meant to encapsulate the sum of all Ohmic resistances in the cell, i.e. ionic resistance in the electrolyte, electric resistance in electrodes, current collectors, and contact resistance. Ionic resistance is much larger than the other components and dominates the overall behavior. The ionic flux through the electrolyte can be driven by a concentration gradient or the applied voltage. Assuming a linear approximation for the concentration gradient, the ionic flux is, $j_i^c = zFD\frac{c_0}{h}$ where $z = \frac{q}{F}$ and represents the charge of a carrier ion per mol, D is the diffusion coefficient, c_0 is the initial concentration of vacancies, and h is the electrolyte thickness. Similarly, with a linear approximation for the potential gradient, the voltage driven ionic flux is given by, $j_i^v = \sigma_i\frac{V}{h} = \frac{N_i q^2 D}{RT}\frac{V}{h}$ with N_i representing the concentration of vacancies and V representing voltage. If $N_i = c_0$ and these expressions are equated, a minimum voltage required to satisfy the concentration gradient can be obtained, $V = \frac{RT}{q}$. At 500 °C with O^{2-} as the charge carrier, a driving voltage of approximately 67 mV is required to overcome the concentration driven flux. As shown in Figure 5, typical driving voltages are much larger than this value. Thus, the voltage driven ionic current is most important.

By rearranging the expression for voltage driven ionic flux as, $V = j_i^v\left(\frac{h}{\sigma_i}\right)$, it can be deduced that the electrolyte ionic resistance takes the form of Ohm's law, with the resistance being directly

proportional to h. Reducing the electrolyte thickness to enable low temperature operation by decreasing the ionic resistance has long been considered a worthy goal,[24, 25] however, the experimental tools and implementations are only starting to reach frontiers necessary to probe such conjectures. The work in this thesis is primarily concerned with physically reducing h as much as possible to minimize the loss from this mechanism, thus allowing SOFC operation at reduced temperatures using classic, non-exotic electrolyte materials such as YDZ and GDC. In summary, this loss occurs at intermediate driving voltages and is dominated by electrolyte resistance which scales inversely with σ_i and directly with h.

1.2.5 Concentration overpotential

The final loss mechanism is most significant at high current densities and is a result of mass transport limitations. In other words, the reactants cannot reach the electrode surface at a rate that is competitive with electronic current extraction. This loss mechanism is related to gas diffusion through porous electrodes, making it strongly dependent on electrode microstructure and fuel flow rates. A simple approximation for the voltage loss can be expressed by, $\eta_a = \frac{RT}{nF}\ln\left(1 - \frac{j}{j_L}\right)$ where j_L is the limiting current density. The limiting current occurs when the surface concentration of the reactant on the electrode goes to zero. It can be modeled using, $j_L = \frac{nFDC_B}{\zeta}$ where C_B and ζ represent the bulk concentration of the gaseous species and the diffusion layer thickness, respectively. Tortuosity in porous electrodes require rigorous mathematical models to accurately estimate triple phase boundary (TPB) lengths,[26] i.e. the active lengths in which the electrode, electrolyte, and reactive gas are all in contact, enabling charge transfer. Experimental methods attempting to address and elucidate this complexity are only recently being explored.[27, 28] While this loss is appreciable and of consequence for systems with finite fuel flow, it is not observed in the

experimental results presented in this thesis. As such, additional discussion on the complexity in modeling and interpretation of this mechanism is deferred to other studies.[29, 30]

1.3 SOFCs with nanoscale oxide membranes

As described in Section 1.2.4, in order to minimize the Ohmic overpotential, an electrolyte with a thickness as small as practically possible is desirable. Traditional methods of producing oxide electrolytes for SOFCs are by solid state processing techniques, such as powder pressing and sintering. These processes lead to thicknesses on the order of 10 μm. Moving towards thinner dimensions requires ceramic slurry based approaches such as tape casting, which may produce thickness on the order of 1 μm. Processing in this fashion requires high temperature furnaces (1400 °C), which can be costly and detrimental for multiple material interfaces. To move into the nanoscale regime, a bottom up approach is necessary. For example, thin film growth and subsequent removal of the underlying substrate enables the movement into the 100 nm range. Additionally, deposition of oxide materials can be carried out at vastly lower processing temperatures (30 – 600 °C), making integration of vastly different material systems possible. Electrical probing of this thickness regime is made possible by the fabrication of stable oxide membranes. Unique experimental challenges and scientific questions are consequently established, which are discussed below. Figure 6 shows a schematic timeline of the physical advances made in state-of-the-art SOFC electrolyte scaling demonstrations and possible future limits at the tunneling barrier.[31-33]

Figure 1- 6: Progress in electrolyte thickness reduction

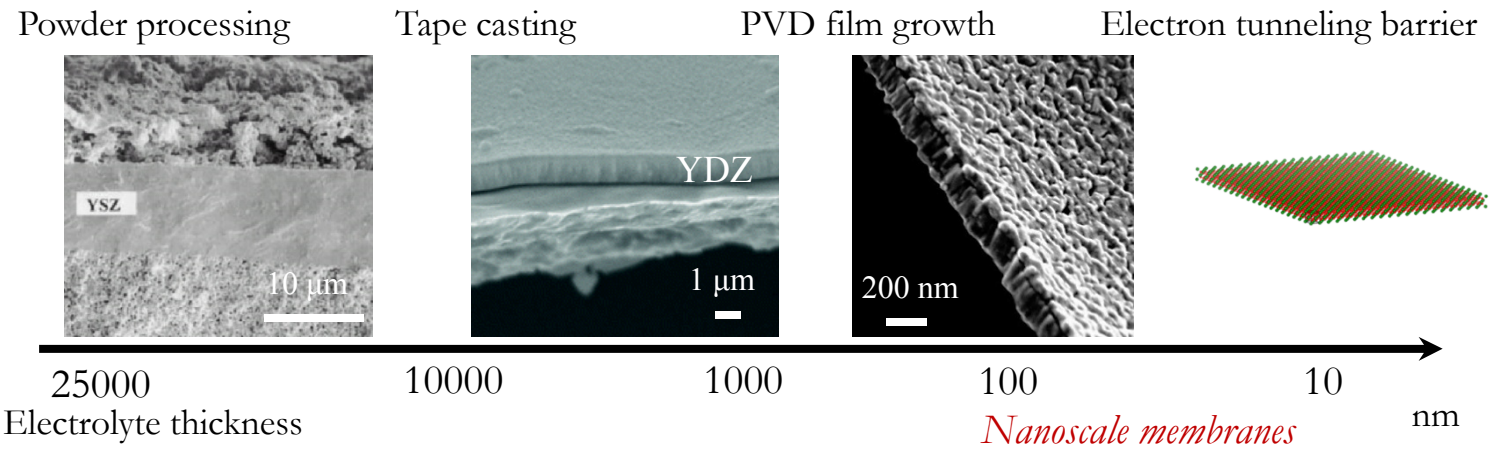

A representation of the progress in scaling solid oxide electrolyte thickness starting with state-of-the-art thin film SOFCs from Lawrence Berkeley National Lab in 1998 (left) moving towards probing of the ultimate limit of atomic layers (right).[31-33]

Growth of stoichiometric, chemically pure, and mechanically robust YDZ and GDC thin films for SOFC applications is a difficult challenge, only recently being pursued in the last decade.[34] Methods of film growth and individual processing subtleties have been reviewed elsewhere.[34-36] While every technique has intrinsic benefits and downfalls, the main challenges from the perspective of forming a nanoscale oxide membrane for high performance SOFC operation can be broadly grouped by mechanical and chemical aspects, discussed below.

1.3.1 Mechanical challenges

From a mechanical perspective, to probe the ultrathin limits of electrolyte thickness reduction requires the formation of free standing oxide membranes;[37, 38] i.e. thin films that are unsupported by a substrate. Oxides are an inherently brittle class of materials.[39] In order to stabilize such structures the mechanics of thin plates must be considered. Initial design aspects utilized boundaries stemming from conditions for film buckling and a Weibull analysis of failure

probability.[40, 41] While these analyses are useful ways to understand the underlying fundamental mechanical considerations for a free standing film structure, they did not have any experimental validation. Optical images of robust free standing YDZ membranes at various side lengths are shown in Figure 7.

Figure 1- 7: Scaling of free standing YDZ membranes

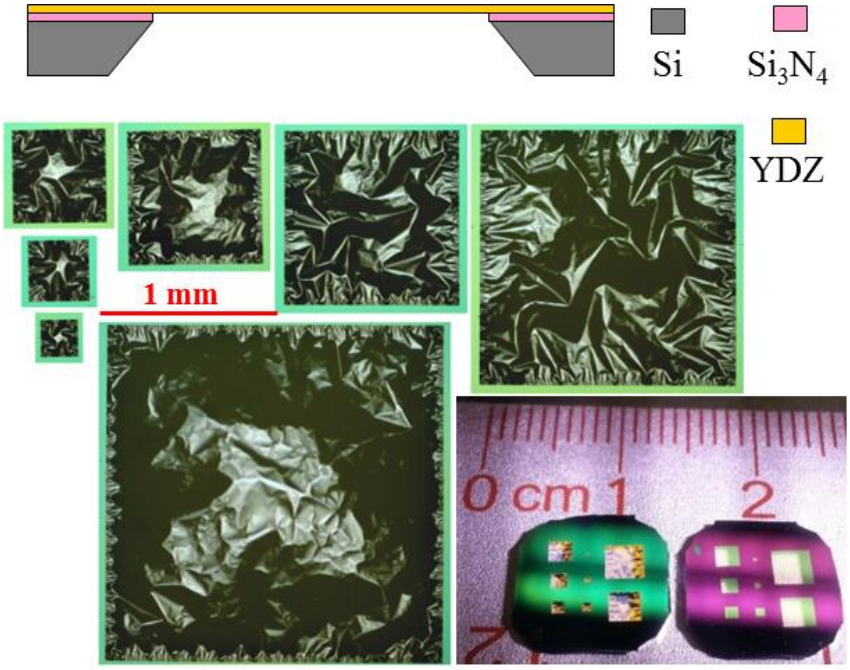

A schematic of the free standing structure is shown in the top portion, while optical micrographs of free standing YDZ are shown in the main panel. The bottom right inset shows two test chips with membranes released (green) from the patterned Si_3N_4 support and un-released (purple) YDZ thin films.

As experimentally demonstrated, buckling is not a failure mechanism, but rather a necessity for stabilizing such thin brittle structures. Therefore, a modified mechanical design space in the post-buckled regime was introduced.[42, 43] Work on the origin of the buckling patterns and elastic stability of the membranes have also been carried out.[33, 44] For a given side-length and film thickness, the key experimentally controllable parameter for determining membrane mechanical stability is the residual

film stress (σ_0). Consequently, from a processing perspective understanding the influence of growth parameters on film stress is essential for fabricating mechanically stable structures.[45, 46] Film processing effects on σ_0 and resulting membrane characteristics are presented in Chapter 2.

As described previously, SOFCs must operate at elevated temperatures for adequate O^{2-} conductivity. While reducing the electrolyte thickness can reduce temperatures from the 800 – 1000 °C range into the 300 – 500 °C range, thermomechanical stress (σ_{TM}) must also be considered. For an isotropic film on a substrate, the thermomechanical stress is given by $\sigma_T = \int_{T_1}^{T_2} \frac{(\alpha_f - \alpha_s)E_f}{1-\upsilon_f} dT$ where α_f, α_s, and $\frac{E_f}{1-\nu_f}$ represent the linear expansion coefficient of the film, substrate, and biaxial modulus of the film, respectively. [47] Using expansion coefficients of α_{YDZ}~6-8 ppm K^{-1} and α_{Si}~2-4 ppm K^{-1} and an elastic modulus of ~200 GPa, [48-50] in the 25 – 500 °C temperature range, σ_T is on the order of several hundred MPa for YDZ films on Si. Therefore, film stress in the membrane must be tuned accordingly to result in stable elastic buckling configurations and prevent rupture by thermomechanically induced stress changes.

1.3.2 Chemical challenges

Regarding chemical aspects, stoichiometry and defects are the key overarching issues of relevance. At reduced thicknesses YDZ and GDC can exhibit properties incommensurate with bulk counterparts, partially due to chemical inhomogeneity. Early work on the enhancement of ionic conductivity (σ_i) in YDZ and CeO_2 thin films hinted at the difference in stoichiometry between nanocrystalline films and their bulk counterparts.[51] Recent studies have shown that σ_i of GDC thin films with thickness comparable to grain size (20 nm) is over four times higher than that of bulk and can be attributed to reduction of grain boundary resistance in conjunction with Gd dopant segregation.[52] Dopant distribution in GDC, and hence transport behavior, has been shown to be

largely influenced by annealing conditions in controlled oxygen partial pressures.[53] An enhancement of σ_i in YDZ films (1000 nm thickness) having grain size of 30 – 50 nm was observed at unexpectedly low Y_2O_3 doping concentrations, ascribed to the extension of the cubic phase below equilibrium doping levels expected from the bulk phase diagram due to nanocrystalline grain structure.[14] These complexities lead to unexpected defect distributions which can be detrimental to SOFC devices integrating nanoscale oxide membranes. For example, in Pt|YDZ|Pt fuel cells OCV values deviating largely from the expected potential have been reported for mechanically stable membranes.[42, 54, 55] This behavior was ascribed to atomic scale defects, potentially arising from the issues discussed above, and pin-hole type voids in thin films. The latter mechanism can be controlled by meticulous multilayer membrane designs.[56, 57] Chemical–mechanical interplay, such as the effect of non-stoichiometry on elastic modulus, is also of concern since the electrolyte membrane must operate across a difference of ~10^{20} atm in partial pressure of oxygen. GDC is known to have p_{O_2} dependence of mechanical properties.[58, 59]

In summary, the dimensionality reduction of electrolyte thickness introduces complex mechanical and chemical issues for material fabrication. Therefore, detailed understanding of the effects of processing on properties and creative fabrication schemes are necessary to demonstrate the advantages of thin film electrolytes in SOFCs.

1.3.3 State of the art

Overcoming the aforementioned challenges to fabricate stable free standing oxide membranes and proof-of-concept SOFCs has been a worldwide effort.[37, 38] A schematic summary of the main experimental research approaches in the field and structures on Si is summarized in Figure 8. Alternative designs using other substrates, such as glass, have also been demonstrated.[60]

Additionally, different etching methods, such as deep reactive ion etching, have also been utilized in creating device structures.[37, 38]

Figure 1- 8: Experimental platforms using oxide membranes

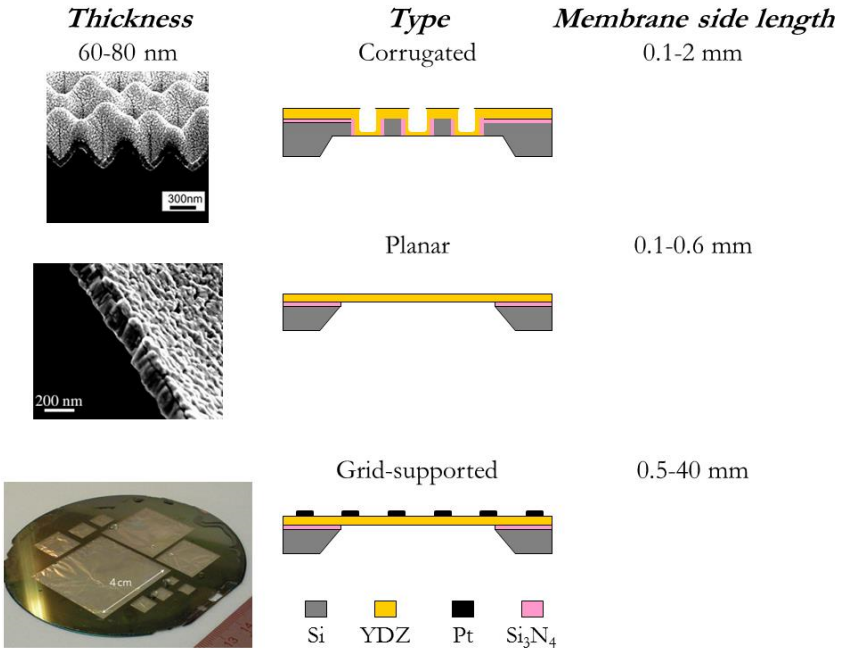

A survey of the types of experimental structures used to integrate ultra-thin electrolyte components into SOFCs.[33, 61, 62] *Image for corrugated and grid supported membranes used with permission from the American Chemical Society and Nature Publishing Group, respectively.*

Proof-of-concept Pt|YDZ|Pt devices are used to evaluate the oxide membrane SOFC. A summary of the maximum power density (P_{max}) of such structures is shown in Figure 10.[38]

Figure 1- 9: Power density of reported Pt|YDZ|Pt SOFCs

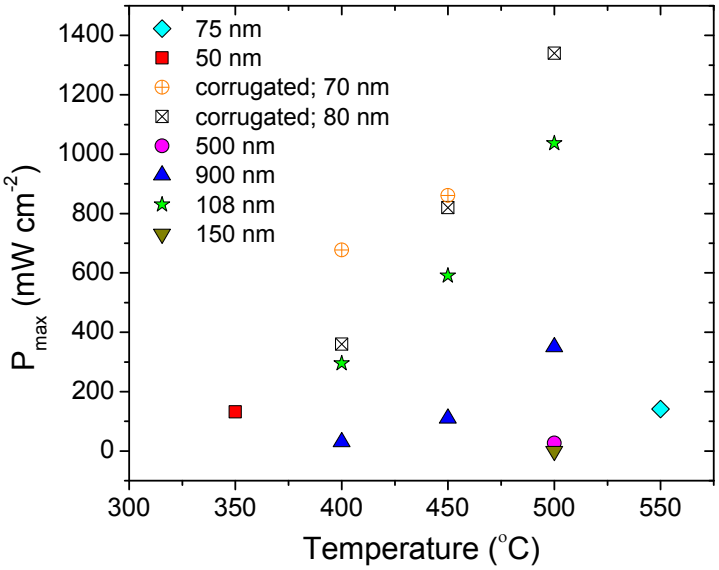

The reported maximum power density of some planar Pt|YDZ|Pt SOFCs in the literature with electrolyte thickness marked. The data is largely scattered and the origin of this behavior is explored in Chapter 3.

Using nanoscale oxide membranes as electrolytes in SOFCs promises the ability to operate at temperatures in the 300 –500 °C range by reducing ionic resistance. This type of reduction coupled with the lightweight nature of thin film based devices opens up the possibility of moving SOFCs into the portable power space as smaller and lighter energy conversion devices, provided the accompanying balance of plant aspects can be scaled accordingly. The integration of oxide membranes in SOFCs as a micro-electromechanical system (MEMS) power source requires a wide-spanning collaborative effort. This ongoing journey has manifested itself in private ventures,[63] in addition to collaborative academic work.[64-66] An enclosed thin film SOFC system utilizing butane as fuel targeted for rapid recharging of mobile devices has been developed.[63] Researchers have also established a battery replacement system with a thermally enclosed thin film based SOFC power source.[65]

1.4 Outline of Thesis

This thesis is sectioned into four chapters that combine select relevant studies towards advancing oxide membranes for SOFC application and future fundamental studies. Chapter 2 considers processing effects on residual film stress and evaluation of buckling patterns for free standing membranes. This work is reported in the literature in ACS Nano 7, 10895 (2013) and J. Power Sources 222, 359 (2013). Chapter 3 moves into proof-of-concept SOFC demonstrations using a model Pt|YDZ|Pt system, based on work reported in J. Appl. Phys. 115, 174307 (2014) and J. Power Sources 196, 2608 (2011). Chapter 4 extends these devices towards incorporating an oxide cathode, thus creating free standing oxide heterostructures. These results are reported in J. Power Sources 196, 6214 (2011) and J. Power Sources 195, 5185 (2010). Chapter 5 describes two experimental approaches developed to synthesize mechanically and chemically stable electrolyte membranes with new functionality, then integrating the materials with symmetric Pt electrodes similar to those in Chapter 3. The studies in this chapter are reported in J. Power Sources 202, 120 (2012) and Adv. Energy Mater. 2, 656 (2012). In Chapter 6, the studies described in this thesis are briefly summarized and future research directions are discussed. The Appendix is meant to serve as a handy resource for researchers working in this area, providing experimental procedures and tips developed during the course of this work. Some aspects of the Appendix are discussed in J. Mater. Res. 29, 320 (2014).

2 THERMO-MECHANICAL CONSIDERATIONS

2.1 Introduction

From an electrochemical perspective, the thin electrolyte membrane must not have an electronically conductive path through the thickness and it must be defect free to avoid electronic shortage or reactant mixing, respectively; either of which can be detrimental to high performance application and safety. Furthermore, in reducing the thickness to the nanometer scale, mechanical stress, stability, and survivability must also be investigated. Preliminary geometrical constraints of thin self-supported membranes for such applications deemed buckling as mechanical failure.[40] By considering non-linear stress analysis it was later suggested that a larger design space in the post-buckling regime exists, however, only bounds for stable near-threshold, i.e. first and second buckling modes, were considered.[42] There has been much research on thin film SOFCs utilizing oxide membranes,[37, 38] mostly without consideration for the higher order buckling modes. A recent investigation addressed the commonality of buckling in oxide membranes used for thin film SOFCs.[44] However, quantitative numerical modeling was limited to compressions in the 0.5 – 300 MPa range. The residual compressive stress of yttria-doped zirconia (YDZ) thin films sputtered at room temperature has been reported to be greater than 500 MPa for thicknesses below 100 nm.[67] In this chapter, we present a combination of numerical and experimental results that addresses the stable configuration of such self-supported oxide membranes and includes a spatial distribution of calculated principal stresses which are useful for failure analysis. We further present scaling behavior at relevant compressions that is broadly applicable to self-supported membranes across a wide size range.

Understanding the interplay between materials synthesis, mechanics and functionality of ultra-thin oxide membranes is a substantial challenge. Internal stress (σ_0) in the oxide film is a crucial

component for the design of self-supported membranes.[42, 68, 69] In polycrystalline thin films σ_0 is related to many factors including film thickness, deposition technique, and post-processing parameters. Kapton, a versatile polymer often used in aerospace applications due to its thermal stability and dielectric properties, is currently of interest as a resilient mechanical material for miniaturized autonomous robotics.[70] Integrating nanoscale oxide membranes on such a platform could enable ultra-light weight sensing and energy conversion devices. However, Kapton and comparable polymer systems have drastically different physical properties than oxides. For example, Kapton has a glass transition temperature of ~360 °C, whereas YDZ has a melting temperature of over 2000 °C; similarly, the thermal expansion coefficient of Kapton is five times larger than YDZ in the 25 – 300 °C range. Creating a stable self-supported oxide membrane on a polymer platform with significantly different physical properties requires crystalline films with tunable internal stress. In this chapter, we present a low temperature thin film processing technique that results in crystalline films and can be used to independently control the stress state. Ultra-light weight membranes can subsequently be integrated as symbiotic 'skins' on miniaturized robotic systems, functioning as power sources or sensors. We demonstrate integration of YDZ onto a Kapton support to form a functional thin film solid oxide fuel cell (TF-SOFC) operable below the polymer glass transition temperature. Our approach demonstrates new routes of integrating structural power sources on autonomous systems of growing interest in diverse engineering disciplines.

2.2 Methods

2.2.1 Background for numerical simulations

Buckling of a compressed square plate at small strains can be analyzed by the energy method of classical stability analysis. With clamped boundary conditions, the critical biaxial buckling stress is $\sigma_{cr} \approx \frac{4.39}{(1-\upsilon^2)} E_m \left(\frac{L}{h}\right)^{-2}$ and out-of-plane amplitude after buckling is given by $w_{max} \approx 0.52\sqrt{\frac{\sigma_0}{E}}L$,

where L, h, E_m and ν represent edge length, thickness, modulus of elasticity and Poisson's ratio, respectively.[71] However, the classical analysis describes only the first buckling mode for the magnitude of the residual stress, $\sigma_0 \geq \sigma_{cr}$, just above the critical buckling threshold. In thin film membranes σ_0 is typically much higher than σ_{cr} and post-buckling far from the threshold must be considered. For $\sigma_0 \gg \sigma_{cr}$ the compressive stress of the membrane relaxes by buckling in the vicinity of the clamped boundary.[71, 72] The basic principle of the stress relaxing boundary layer is best understood by a simple scaling analysis. In-plane compression relaxes over a width δ by out-of-plane buckling. The buckling has a wavelength λ; amplitude $A \sim \lambda\sqrt{\frac{\sigma_0}{E_m}}$; curvatures $C_{\parallel} \sim \frac{A}{\lambda^2} \sim \frac{\sqrt{\sigma_0/E_m}}{\lambda}$ and $C_{\perp} \sim \frac{A}{\delta^2} \sim \frac{\lambda\sqrt{\sigma_0/E_m}}{\delta^2}$ in directions parallel and perpendicular to the boundary, respectively; in plane energy per unit length of the boundary $S \sim \frac{h\delta{\sigma_0}^2}{E_m}$; and bending energy $B \sim E_m h^3 \delta\left(C_{\parallel}^2 + C_{\perp}^2\right) \sim h^3\delta\left(\frac{\sigma_0}{\delta^2} + \frac{\lambda^2\sigma_0}{\delta^4}\right)$. Minimizing the sum of in-plane and bending energy, $U = S + B$, by requiring $\frac{\partial U}{\partial \delta} = \frac{\partial U}{\partial \lambda} = 0$ yields $\lambda \sim \delta \sim \frac{h}{\sqrt{\sigma_0/E_m}}$. The wavelength of buckling is coarsened by a series of periodic steps moving from the boundary layer towards the interior of the membrane.

Quantitative modeling of the elastic membrane buckling was carried out using a square lattice similar to previous studies on compressed sheets.[73, 74] Each square was divided into triangles along the diagonal and the position of the triangle nodes was used to determine in-plane strain. Compression of the membrane was implemented by imposing a biaxial in-plane strain $\frac{\sigma_0(1-\nu)}{E_m}$ in the flat initial configuration. Buckling amplitude of the membranes can be large, but gradients of out-of-plane displacement are still small, which implies that deformation patterns are functions of a scaled stress $\tilde{\sigma}_0 = \frac{\sigma_0}{E_m}\left(\frac{L}{h}\right)^2$ parameter, assuming a fixed Poisson ratio, ν = 0.3. This greatly simplifies the

numerical task since $\frac{L}{h}$ can be fixed and only σ_0 need be varied to cover the whole experimentally relevant parameter range. A lattice of 320 x 320 sites having $\frac{L}{h} = 1000$ was used. The role of the residual stress was studied by gradually increasing σ_0 from zero to $\sigma_0 = 0.047E_m$, which corresponds to $\tilde{\sigma}_0$ increasing from zero to $\tilde{\sigma}_0 = 4.7 \times 10^4$.

2.2.2 Experimental aspects

All films were grown by radio frequency magnetron sputtering (AJA International) from a 2 inch diameter, 8 mol% YDZ target (Plasmaterials Inc.) at 100 W in an Ar environment. Growth pressure was controlled using an adaptive pressure regulator controlling a throttle valve. Growth rate was approximately constant with pressure. The growth temperature for films grown without substrate heating was estimated by using an interferometer during growth and verified by placing a thermocouple on the substrate holder immediately (less than five minutes) after growth. Internal stress in the films was determined by measuring wafer curvature changes (Toho FLX-2320-S) and using Stoney's equation,[75] $\sigma_0 = \frac{E_s}{1-\nu_s}\frac{\Delta K}{6}\frac{h_s^2}{h_f}$ where $\frac{E_s}{1-\nu_s}$, ΔK, h_s, h_f, are the substrate biaxial modulus, change in curvature, substrate thickness, and film thickness, respectively. Film thickness and growth rate were obtained by low angle reflectivity using a coupled scan in the $0.4° < 2\theta < 3°$ range using a step size of 0.002° with parallel beam optics (Bruker D8, Cu anode). Phase information was gathered by fixing Ω=1° and scanning from $20° < 2\theta < 70°$ with a step size of 0.01°. Surface morphology and roughness for samples on Si_3N_4/Si samples was measured in tapping mode (Asylum) using Al/Si cantelevers (Asylum AC160TS). YDZ samples on Kapton were imaged in contact mode, with Al/Si cantilevers (Pointprobe FMR-10). Images of film surfaces were taken (Zeiss Ultra-Plus) using a charge compensating electric charge dissipater and the in-lens detector at an accelerating voltage of 3 kV. Out-of-plane deflection was determined using a laser confocal

microscope (Olympus LEXT OLS4000). Micro fabrication methods were used to photolithographically pattern and etch a Si_3N_4/Si wafer. 30 wt% KOH was used to etch Si, while a mixture of CF_4 and O_2 (15/12) was used to etch Si_3N_4. 180 μm Kapton was bonded to custom made carbon-fiber composites using an acrylic adhesive (Pyralux® by DuPont™). The structure was then laser cut to an assembly of self-supported Kapton. After YDZ growth, this support was etched in a mixture of CF_4 and O_2 (30/100) to form self-supported YDZ.

2.3 Film processing

The initial structural x-ray characterization of the polycrystalline films is shown in Figure 1a. It can be seen that the YDZ films are phase pure, (111) textured, and of cubic (Fm-3m) nature (indexed to ICDD 030-1468). The out of plane lattice parameters were extracted by Gaussian fitting of peaks to determine exact 2θ values, which were then used to calculate d-spacing using Bragg's law. The results are plotted in Fig. 1b-d as a function of thickness.

Figure 2- 1: XRD of YDZ films with varying thickness

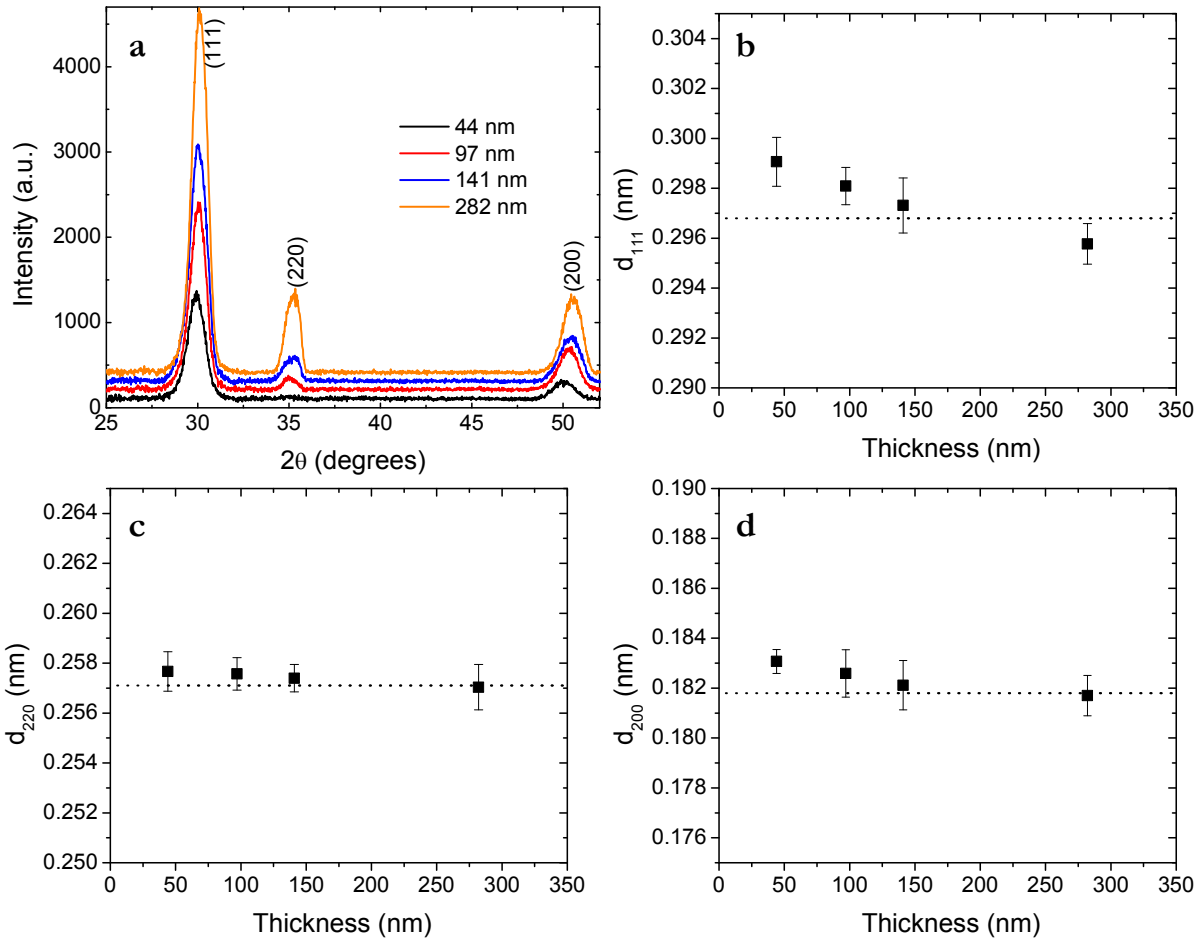

(a) *X-ray diffraction patterns of select YDZ films showing the single phase crystallinity, indexed to ICDD-030-01468. The out-of-plane lattice parameter of* ***(b)*** *(111),* ***(c)*** *(220), and* ***(d)*** *(200) as a function of film thickness with dashed lines depicting the ICDD lattice parameter value. Error bars correspond to ±3 standard deviations.*

From these figures it appears that there is thickness dependence of lattice constant likely due to residual stresses in the film. Anion non-stoichiometry can also cause lattice constriction and hence deviation from the expected lattice constant. All samples were grown under congruent conditions, discounting this reason for the observed behavior. Annealing the films at high temperature could change the concentration of oxygen vacancies, but would also change the internal stress state and peak positions. Therefore, this characterization was done on as-grown films. Since the films are not

coherently strained to the substrate, the origin of these residual stresses can be related to atomic peening during initial stages of film growth.[76, 77] From the tabulated value (ICDD 030-1468) for YDZ, the unstrained lattice parameter is also plotted as a dashed line. Out-of-plane lattice parameters appear larger than that of bulk YDZ, implying that there is in-plane compression in the films. Using a least squares linear fit to each of the three families, the expected unstrained thickness can be estimated by weighing the respective cross-over thickness by the relative intensity of each peak. An average thickness value of ~240 nm is estimated to be nearly stress free.

Figure 2 shows the total residual film stress (σ_0) as a function of thickness for as-deposited YDZ films. All films exhibit compressive σ_0 with monotonically decreasing magnitude as the thickness increases. Based on the approximate estimation of strain state from the x-ray results in Figure 1, it was expected that the films thicker than ~240 nm would be nearly strain free. As seen in Figure 2, this is not exactly the case. One possibility for this slight discrepancy is that only three orientations were used to make this assertion, but since the film is polycrystalline all orientations play a role in strain behavior of the film. Additionally, it is known that there can be error in lattice parameter estimations at low diffraction angles since a small measurement error can result in a large lattice parameter miscalculation. The slope of the linear fit to each family appears to reduce as the diffraction peak position increases in angle, therefore the rough strain free thickness estimation from this method may be an underestimate. The last consideration is that the method of wafer curvature becomes inappropriate at very small curvatures, or low film stress, therefore the error associated with smaller stresses becomes a substantial fraction of the actual value.[78]

Figure 2- 2: Intrinsic film stress as a function of YDZ thickness

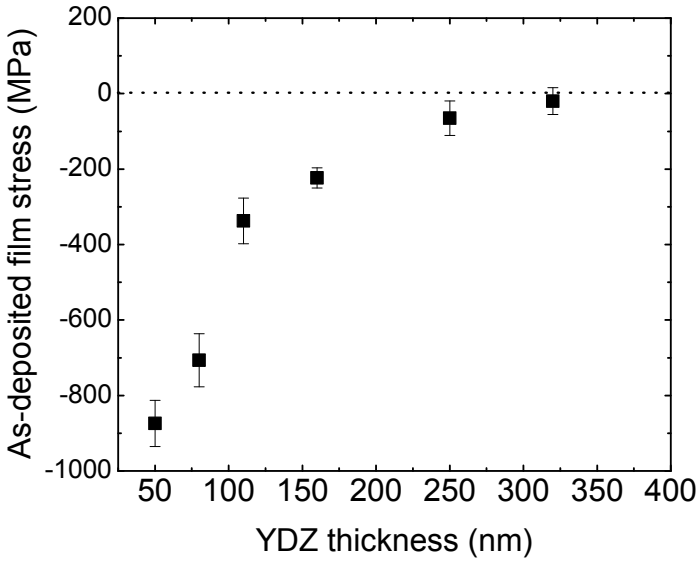

The average internal stress measured in as-deposited YSZ films measured by wafer curvature as a function of thickness is shown. Growth temperature and pressure was 550 °C and 0.58 Pa, respectively. Error bars correspond to ±3 standard deviations for average values plotted.

Thus far, we have considered the temperature and pressure independent intrinsic stress of YDZ films as a function of film thickness. The trends presented above agree well with previous work on sputtered YDZ films and the fundamental mechanism of increased surface chemical potential of atoms during polycrystalline film growth, which leads to macroscopic compressive stresses.[67, 79] However, the previously described elastic scaled stress parameter, $\tilde{\sigma}_0 = \frac{\sigma_0}{E_m}\left(\frac{L}{h}\right)^2$, depends on both σ_0 and $\left(\frac{L}{h}\right)^2$. Based on the approach for making free standing membranes, L is controllable. It is noted that this simple model is purely elastic. Therefore, it does not take statistical failure into account. For example, arbitrarily increasing L, all else constant, scales $\tilde{\sigma}_0$. As discussed in Section 2.4 below, for a given set of boundary conditions (L=160 μm in the discussion below), this parameter can be used to determine regions of membrane stability. However, as the dimensionality

of L increases, so does the probability of failure due to the increase likelihood of a critical defect in the film. Therefore, this simple model may not be adequate to describe the possibility of failure at increased membrane side lengths. In an effort to mitigate failure by stress control, independent control of σ_0 is desirable. Figure 3 shows the intrinsic stress of YDZ films having h~100 nm grown at two different temperatures and various working pressures. All films were fully crystalline and additional characterization of these films including morphology and surface roughness are reported in Ref. 45.

Prior work on the effects of various parameters on sputtered film stress for elemental metal systems show that the origin of σ_0 can be either extrinsic or intrinsic.[80, 81] The former is thermally induced by virtue of substrate and film having different expansion coefficients, while the latter is either impurity or atomic peening induced.[81] Compressive stress indicates that the thermally induced extrinsic component is small, as one would expect a tensile contributed based on the differences in coefficient of thermal expansion between Si and YDZ. The dominance of the intrinsic component is also supported by roughly comparable values of σ_0 for films processed at 550 °C and 30 °C. For the latter, there is cross-over in stress from compressive to tensile at P~0.55 Pa. This is a result of the increasing scattering events at high pressure, leading to multi-directional velocity components of ions reaching the film surface.[81] Films grown at 550 °C appear to approach this cross-over at a slightly higher deposition pressure, likely related to elevated surface temperature. The ability to produce compressive internal stress in the oxide film is a desirable condition to fabricate robust self-supported membranes that do not rupture from tensile fracture upon external perturbations.

Figure 2- 3: Intrinsic YDZ film stress as a function of pressure

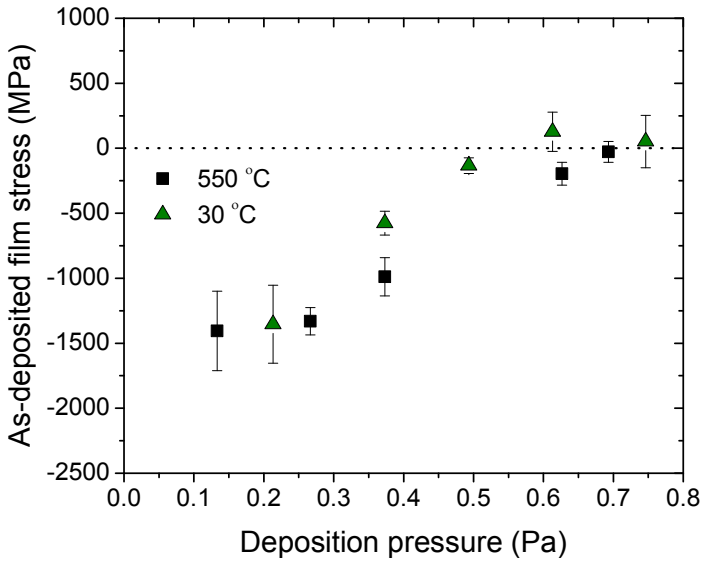

Internal stress measured by wafer curvature changes for 100 nm thick YDZ films on Si_3N_4/Si substrates with error bars corresponding to ±3 standard deviations obtained from 12 measurements on each wafer.

Previous studies on reactively sputtered YDZ reported deposition pressure dependence of internal stress for ~250 nm thick films.[67] We point out some key differences between our observations and that of Ref. 67. As previously shown, the internal stress of YDZ is a function of thickness at constant pressure. Therefore, for a given thickness, the functional dependence of internal stress on deposition pressure may not necessarily be compared. In Ref. 67 there is a sharp cross-over pressure at P ~ 1.33 Pa and the lowest deposition pressure studied is P ~0.66 Pa. In this work, we demonstrate for the first time the ability to control the internal stress in the very narrow deposition pressure range of $0.13 < P < 0.7$ Pa. Finally, there are variations in reported values of internal stress for YDZ, likely due to the subtle differences of specific deposition conditions. These subtleties become of extraordinary importance when fabricating free standing membrane structures since regions of elastic stability for buckled self-supported membranes are directly proportional to

σ_0, which as we show here, can be quite sensitive to deposition pressure, among other important parameters.[33, 44]

2.4 Membrane buckling

The preceding section was concerned with YDZ films bound to a substrate. Figure 4 shows a schematic outline of the process used to fabricate free standing membrane structures from these films, which will be discussed in this Section and the basis for fuel cell devices. In the membrane configuration, there is a defined area in which the underlying substrate support is removed from below the film. This square area, having side length L=160 μm, forms the free standing oxide membrane. Upon release from a substrate support, thin films form clamped membranes that buckle. This is a result of in-plane strain energy in the film being converted to out-of-plane bending energy in the membrane. For high orders of buckling, *i.e.* beyond a single buckled wavelength along boundary layers, the periodicity and amplitude of deformations along the clamped boundary are closely related to the internal stress.

Figure 2- 4: Schematic of membrane processing

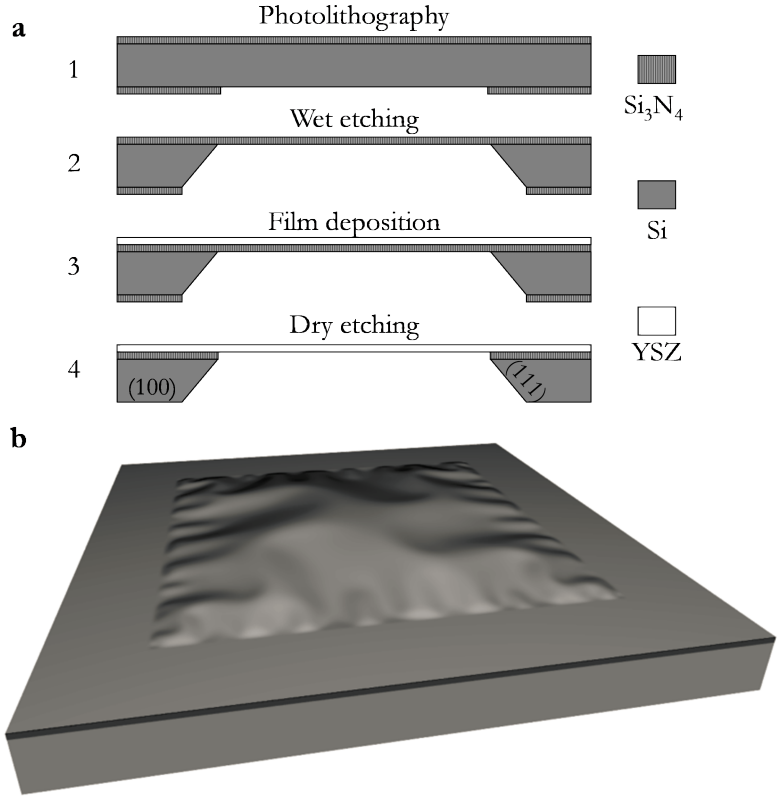

(a) *Schematic of wet etching process flow used to create the free standing membranes and* ***(b)*** *3-D computational simulation of the buckling expected from such a membrane.*

It is favorable for membranes to remain in a compressive regime throughout SOFC operation to prevent tensile stress induced failure, either by stress relaxation or thermally induced stress. Figure 5 shows some optical and confocal micrographs of membranes of varying YDZ thickness and therefore varying intrinsic stress states.

Figure 2- 5: YDZ membranes of varying thickness

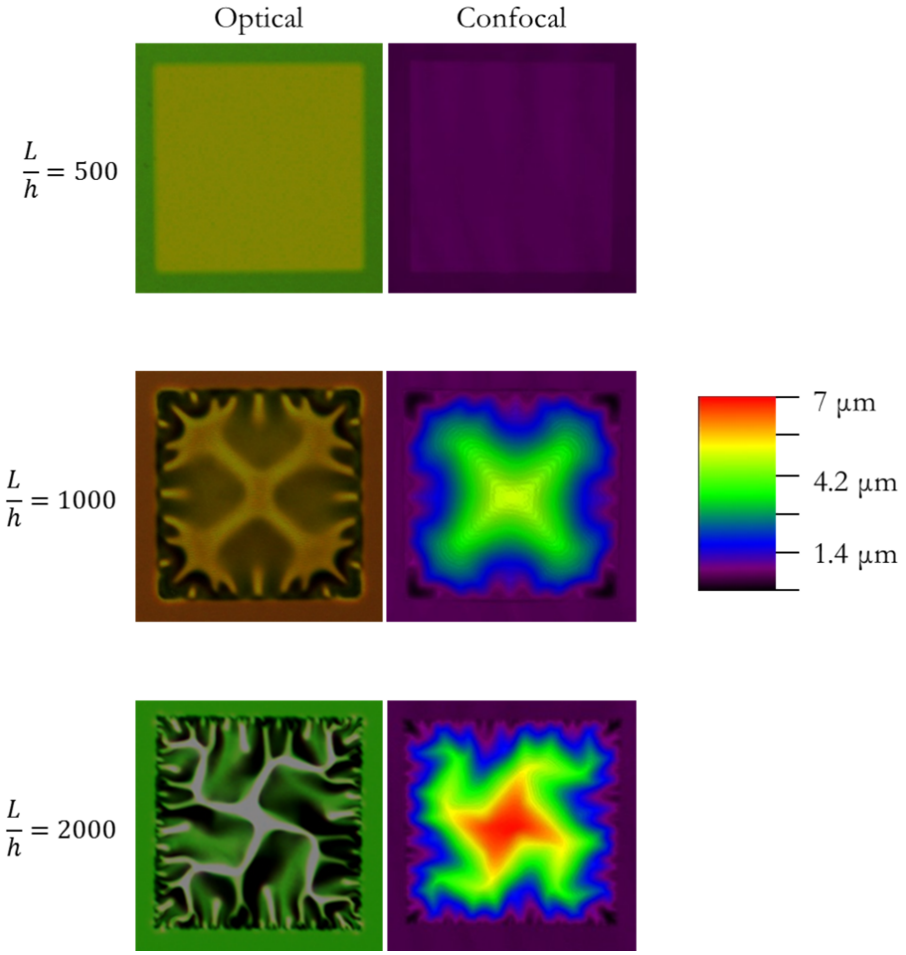

Experimental optical and confocal micrographs of free standing YDZ membranes, 160 μm in side length with varying $\frac{L}{h}$ *indicated. Here, the internal YDZ stress is modified by film thickness. Beyond a critical value of* $\frac{L}{h}$*, buckling patterns tend towards the swastika-like pattern.*

Figure 6a shows a numerical simulation of the expected membrane buckling formation for the ground-state configuration, i.e. the highest compressive stress. Buckling induced by compressive internal stress inevitably causes tensile stresses along the periodic ripples. For square membranes having L~160 μm, numerical simulations shown in Figure 6b indicate the maximum tensile stress generated from buckling is comparable to σ_0.[33]

Figure 2- 6: Simulation of YDZ membranes

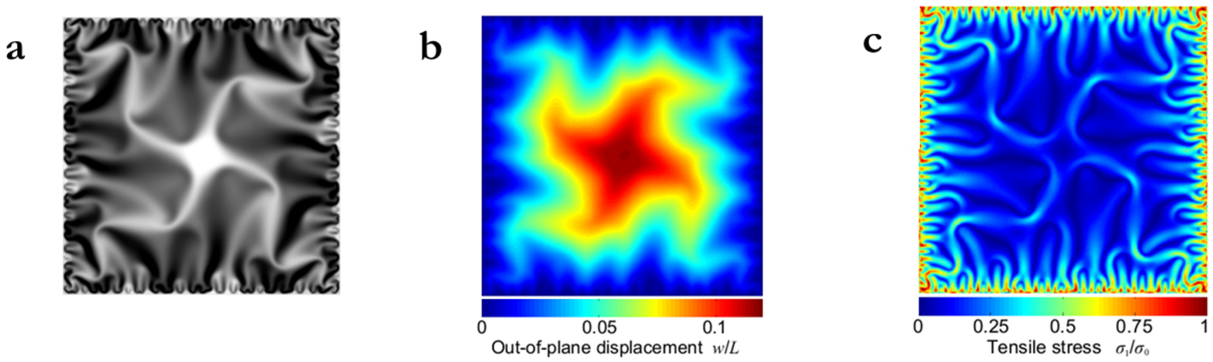

(a) *Modeling configuration of a bound YDZ membrane with scaled biaxial stress* $\tilde{\sigma}_0 = \frac{\sigma_0}{E}\left(\frac{L}{h}\right)^2 = 4.7 \times 10^4$, ***(b)*** *out-of-plane displacement of the free standing membrane, and* ***(c)*** *the distribution of tensile stress normalized to* σ_0. *(a) and (b) can be compared to optical and confocal experimental observations, respectively.*

The simulation and experimental results are quite similar, confirming that a simple elastic theory suffices to understand how the patterns are formed. The simulated buckled configuration at small $\tilde{\sigma}_0$, immediately after first buckling, is symmetric with respect to diagonal reflections. However, the symmetric configuration persists only up to $\tilde{\sigma}_0 \approx 4 \times 10^2$, beyond which the pattern changes to a swastika-like appearance. Further increase of $\tilde{\sigma}_0$ in simulations does not change the pattern in the interior of the membrane; though the amplitude increases and wavelength at the boundary refines. This appears to corroborate the classic work on mechanical response of micro-machined Si_3N_4 square membranes done by Ziebart et al.[68] Their work shows the transition to the swastika-like pattern at pre-strain that corresponds to $\tilde{\sigma}_0 \approx 3 \times 10^2$ and the pattern persists with sharpened refinements as the strain is increased. The out-of-plane amplitude in the ground-state configuration is approximated well by the above expression for w_{max} even when $\sigma_0 \gg \sigma_{cr}$.

As shown, not all membranes display the swastika kind of pattern after the Si_3N_4 support has been removed. In some instances the diagonal reflection symmetry is roughly retained. During

simulations a similar pattern was obtained by incrementing $\tilde{\sigma}_0$ rapidly, thereby allowing less time for full elastic relaxation to occur. The symmetric pattern obtained has slightly higher deformation energy than that of the swastika configuration and is metastable. Therefore, if this pattern is observed in the $\tilde{\sigma}_0 > 10^3$ regime, it is likely that the membrane may further deform to achieve the most energetically stable configuration. We also simulated membranes constrained to reflection symmetry at constant σ_0, finding up to 5% higher deformation energy than the ground state. These findings are confirmed by experimentally observed configurations of YDZ, where the swastika-like pattern is seen after repeated heating cycles and for membranes as thin as 27 nm.[82, 83]

Figure 7 shows the resulting membrane configurations when independently scaling σ_0 by using deposition pressure at constant $\frac{L}{h}\left(\frac{160\,\mu m}{100\,nm}\right)$. Of note is that even samples grown at ~0.7 Pa are buckled though the magnitude of σ_0 is small. This is a result of controlling σ_0 independent of h, allowing $\frac{L}{h}$ to remain large enough to observe buckled configurations.

Figure 2- 7: YDZ membranes at constant $\frac{L}{h}$

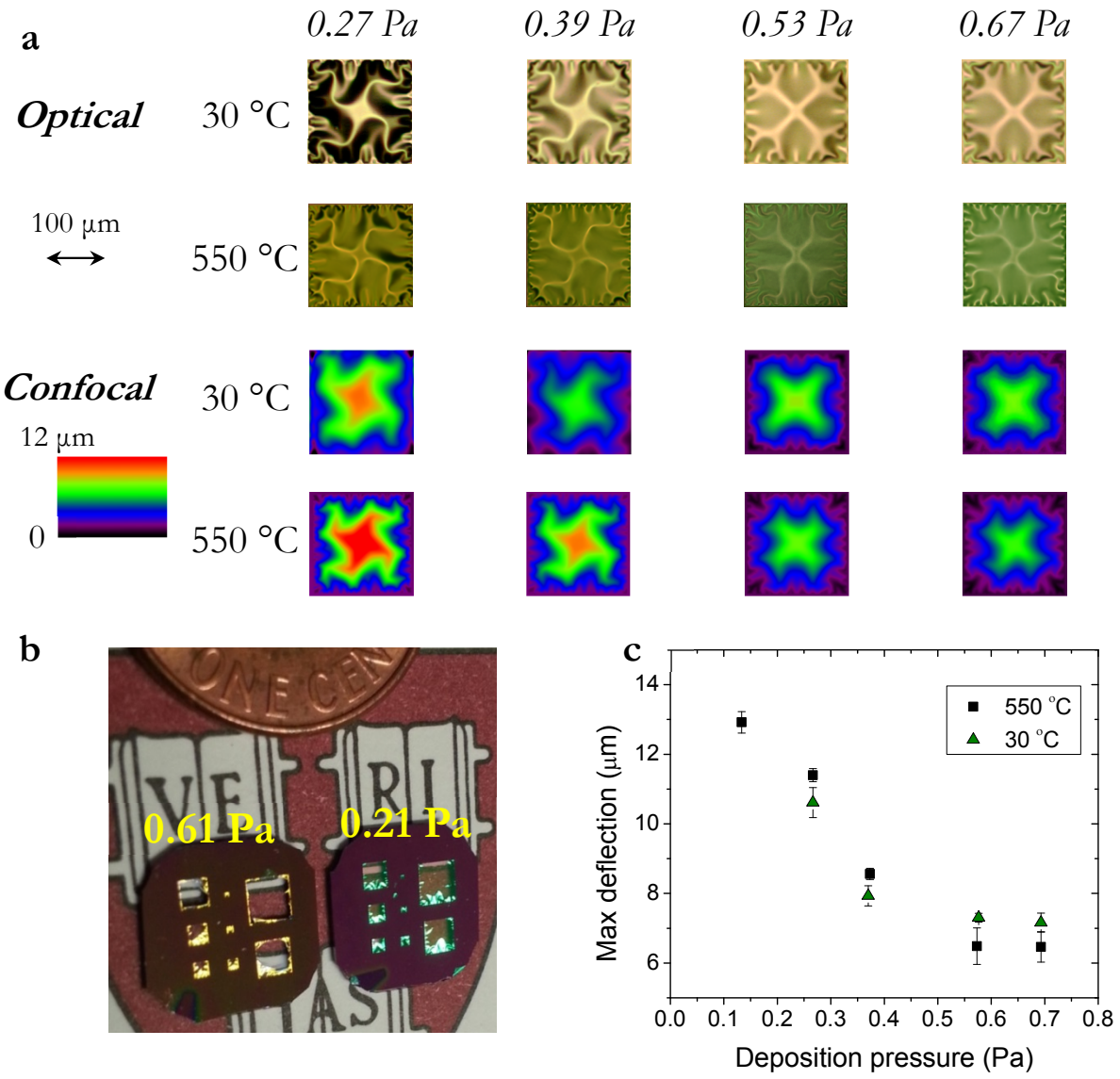

(a) *Optical and confocal images of self-supported YDZ membranes having fixed* $\frac{L}{h}\left(\frac{160\ \mu m}{100\ nm}\right)$ *and corresponding deposition pressures.* ***(b)*** *Two test chips with self-supported YDZ films grown at 30 °C using different deposition pressure spanning side lengths of 0.15 – 2.5 mm demonstrating stress controlled scalability.* ***(c)*** *The maximum deflection of membranes shown in (a) as a function of deposition pressure as measured by confocal microscopy. A monotonic decrease in deflection of the buckled membranes corroborates the decrease in compressive stress with increasing pressure.*

The buckling configurations are strikingly similar for both deposition temperatures, confirming the ability to independently control internal stress and form stable membrane structures for a given aspect ratio at temperatures as low as 30 °C. This is a key result that allows the realization of suspended membranes on polymeric substrate Kapton, since scaling σ_0 using h at constant pressure requires unreasonable thicknesses or leads to unstable flat membranes.[13, 17] Figure 7b exhibits the utility of this process by comparing two samples grown at low temperature and different pressure having eight different side lengths, hence changing $\frac{L}{h}$ at constant h, and independently controlling σ_0. As shown, if σ_0 is adequately compressive, scalable self-supported YDZ membranes grown at 30 °C can be fabricated on the millimeter length scale without any additional support layers. Figure 7c shows out-of-plane deflection data for the membranes, which can potentially be used for calculating local stress on the membrane and possibly predicting failure.

While we do not measure the evolution of intrinsic film stress as a function of temperature, thermal cycling tests in the 25 – 500 °C range were carried out to evaluate the survival rate of membranes having varying initial stress states. Previous work suggests a significant relaxation of σ_0 for various annealing conditions,[67] but compression can remain provided the magnitude of σ_0 is large enough initially. Membrane survivability after repeated thermal cycles is an adequate indication of whether the stress state change has caused mechanical failure. Figure 8 shows the survival rate of YDZ membranes with constant $\frac{L}{h}\left(\frac{160\,\mu m}{100\,nm}\right)$ and different values of σ_0 grown at 30 °C. As shown, the membrane survival rate increases monotonically with increasing compressive film stress. This is likely due to the fact that larger σ_0 counteracts any thermal stress relaxation as well as the thermomechanically induced stress from substrate-film expansion mismatch. It is noted, however, the survival behavior of films grown at 30 °C and 550 °C differs. Films grown at high temperature are more resilient and exhibit a perfect survival rate until 0.58 Pa, where 96% is seen. The increased

robust character of these membranes with respect to those grown at 30 °C is likely a result of microstructural stability. In addition to robust mechanical behavior, the electronic behavior of the membranes with an oxygen partial pressure gradient is important for fuel cell operation. Electrochemical behavior of the membranes, i.e. ionic conductivity during operation, does not appear to vary with σ_0 based on fuel cell measurements,[45] though the membranes with the highest compressive stress (lowest deposition pressure) exhibit a less than ideal open circuit voltage perhaps due to non-critical defects.

Figure 2- 8: Survival rate of thermally cycled YDZ membranes

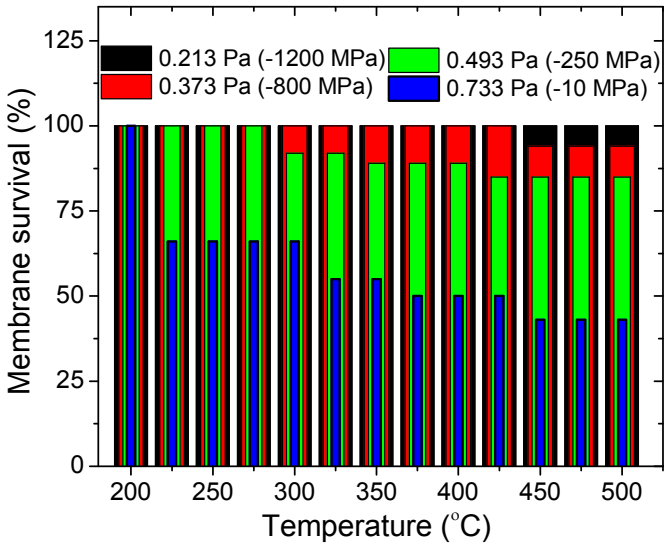

Mechanical survival statistics (minimum of 18 samples) of free standing YDZ membranes fabricated at 30 °C on micromachined Si platforms for several deposition pressures with approximate residual stresses marked, as a function of temperature. The rupture was monitored optically at 10 °C intervals, temperatures were recorded on heating, and rounded down to the nearest 25 °C.

2.4.1 Monolithic membrane integration

Although values of σ_0 for YDZ films on Kapton may not be exactly the same as YDZ grown on Si_3N_4/Si control samples described above, the functional dependence on deposition

pressure and mechanical resilience likely remains. Thus, by growing crystalline YDZ films at low temperature, oxide membranes capable of functioning as electrolyte membranes on polymeric substrates can be realized. A thin polymer support is generally not suitable as a substrate on its own due to a lack of rigidity. As shown in Figure 9a, an as-grown YDZ film on bare Kapton creates a non-planar structure, which leads to macroscopic cracks unsuitable for gas-tight, dense, and mechanically robust membrane structures. Substrate curling is a direct result of the internal stress of the oxide film, discussed previously. To overcome this inherent difficulty, a polymer adhesive was used to bond Kapton onto a carbon fiber scaffold. This particular support was selected due to its mechanical resilience and current use as a structural material in the development of bio-inspired insect-like robots.[70] The structure cannot be cleaned by traditional substrate methods (*i.e.* organic solvent rise and N_2 dry) as this may decompose the polymeric components or reduce the effectiveness of the adhesive. Therefore an *in-situ* Ar plasma treatment to remove adsorbed contaminants on the structure immediately preceding YDZ growth was used. Atomic force microscopy images of the bare Kapton surface before and after Ar plasma treatment indicated negligible surface morphology changes. Etching of Kapton to release the free-standing oxide membrane is recommended by DuPont using a mixture of potassium hydroxide, ethanol, and water. However upon using this formulation, we encountered a severe reaction shown in Figure 9b. Therefore, a dry etching procedure was devised to remove the support without damaging the structure and maintaining the mechanical integrity of the YDZ membrane. Based on the understanding of membrane mechanics and experimental control of internal film stress, some representative successful examples of self-supported oxide membranes on Kapton are shown in Figure 9d–e. The buckling patterns appear to differ from those described on a rigid substrate, implying that interface stress coupling is of importance when studying this aspect. The membranes

are stable upon thermal cycling in the 25 – 300 °C range and enable monolithic fuel cell devices that can operate below the polymer glass transition temperature.[45]

Figure 2- 9: Integration of YDZ membrane onto polymer

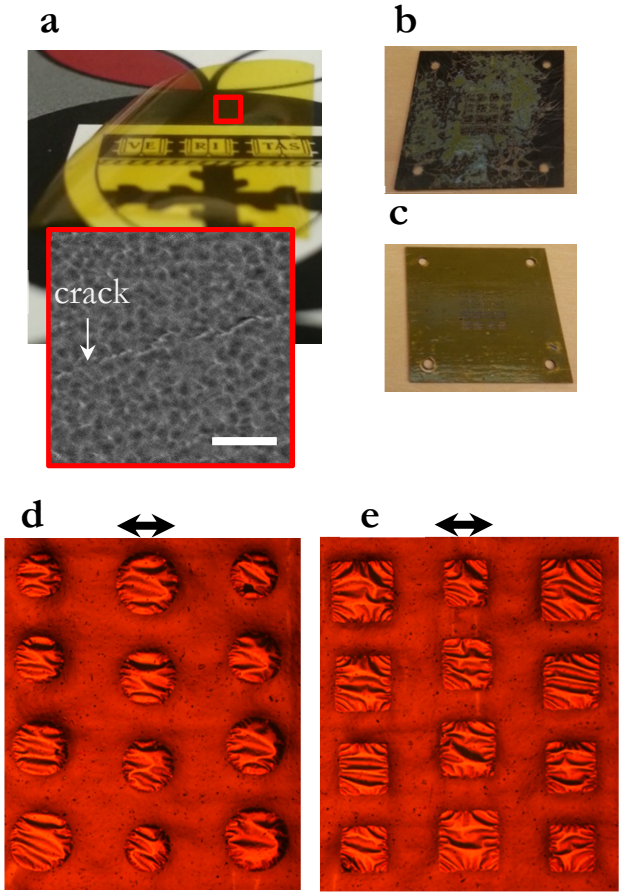

(a) *Curling of a piece of Kapton after YDZ deposition with an inset showing a SEM image of YDZ microstructure showing a planar crack on the surface. The white scale bar is 200 nm;* ***(b)*** *a 10×10 cm test structure of YDZ/Kapton/adhesive/carbon fiber depicting the catastrophic nature of wet etching and* ***(c)*** *successful dry etching protocol;* ***(d)*** *circular and* ***(e)*** *square YDZ membranes on a Kapton test structure after release. The arrow scales are 300 µm, the side-length and diameter of the largest membranes made. Note that arbitrary membrane geometries are possible with this technique, whereas on Si different micromachining processes must be used to obtain alternative membrane geometry due to constraints of anisotropic wet etching.*

2.5 Conclusion

This chapter describes the interplay between processing parameters and intrinsic film stress for YDZ films. Compressive stress can be tuned independent of temperature by using deposition pressure. This degree of freedom enables the fabrication of stable membrane structures on Si and polymeric based substrates. Adequate compressive stress is needed to counteract film relaxation that could lead to free standing membrane rupture. The origin of the buckling configuration of free standing membranes can be modeled using a simple elastic theory.

3 MODEL SYSTEM DEMONSTRATION

3.1 Introduction

Though there has been decades of research on conventional solid oxide fuel cells (SOFCs),[84] the challenges of producing high performance thin film based SOFCs for low temperature applications are still in relatively early stages.[37, 38, 85] SOFCs with thin film electrolyte membranes and electrodes can be integrated using semiconductor processing technology, making them an interesting field that has potential for facile manufacturing scale up. Moreover, the large decrease in Ohmic loss of thin electrolyte films in such SOFCs can greatly reduce the overall operating temperature, which is typically in the range of 800 –1000 °C for conventional SOFCs. Benefits of decreased temperature operation to the 300 – 500 °C range using electrolyte membranes include reduced start up time, mitigated material degradation or instability issues in stacking architectures, and potential practical realization of portable SOFCs.[86] Creating optimal porosity in metallic or ceramic-metal composite electrodes to mediate the electrochemical reactions occurring at triple phase boundaries (TPBs) is of essence for SOFC performance because both oxidation and reduction reactions occur only at TPBs between the oxidant or fuel, the electrode, and the electrolyte.[87] The maximum power density in SOFCs is a convolution of many factors, but in order to achieve optimal SOFC performance with ultrathin electrolyte membranes, a systematic evaluation of the main cell components, such as the electrodes and electrolyte, is essential. Although large variations, ranging several orders of magnitude, in performance of Pt|$(Y_2O_3)_{.08}(ZrO_2)_{.92}$|Pt (Pt|YDZ|Pt) SOFCs exist within the field,[38] a mechanistic understanding of the governing factors is yet to emerge. Figure 1 graphically depicts performance of planar Pt|YDZ|Pt thin film SOFCs that various research groups have reported thus far.

Figure 3- 1: Survey of power densities for Pt|YDZ|Pt SOFCs

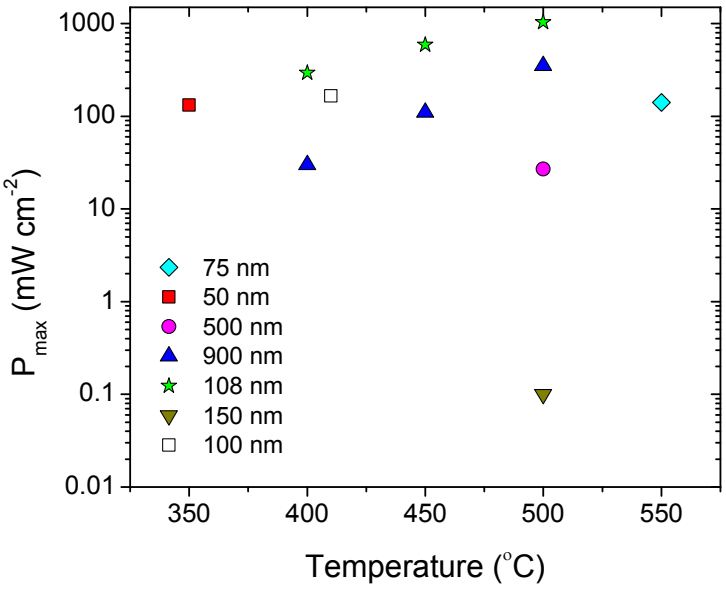

A select survey of the power densities reported in the literature for Pt|YDZ|Pt SOFCs integrating free standing electrolyte membranes.[38] *The legend corresponds to the YDZ thin film thickness.*

Though device fabrication methods and thin film deposition techniques vary amongst researchers, a systematic experimental evaluation of performance and durability in Pt|YDZ|Pt thin film SOFCs has not been addressed in detail. Furthermore, fundamental physical limitations of electrolyte thickness reduction and physical mechanisms that could lead to appreciable loss arising from scaling of solid electrolytes remain unanswered and warrant investigation for advanced design of high performance energy conversion technologies. In this chapter, we use the metal-insulator-metal structure (Pt|YDZ|Pt) to model the limits of charge separation in the context of SOFCs, i.e. insulators separated by potentials in the $0 < V <$ 1.2 V range at elevated temperatures of $573 < T <$ 773 K. Using known mechanisms of electronic transport in insulating thin films we present the possible physical limitations of dense electrolyte thickness reduction on power output, an important metric of such energy conversion technologies. Moreover, we report the effects of sputtered

electrode porosity and electrolyte thickness on thin film SOFC performance. Lastly, we investigate the fixed temperature stability of such devices and discuss mechanisms leading to performance changes.

3.2 Methods

3.2.1 Electrochemical modeling

The model used to fit experimental data is based on electrochemical relationships widely discussed in the literature. As described in Chapter 1, the SOFC cell voltage can be expressed by, $V_{cell} = V_n - \eta_a - \eta_\Omega - \eta_c$, where V_n is the Nernst potential, and η_a, η_Ω, and η_c are voltage losses (i.e. overpotentials) corresponding to the activation (oxidant reduction reaction), Ohmic (electrolyte transport), and concentration (reactant mass transport) processes, respectively. The Nernst potential was calculated using $V_n = V_{OC} + \frac{RT}{nF}\ln\left(\frac{p_{H_2}\sqrt{p_{O_2}}}{p_{H_2O}}\right)$, where V_{OC} is the open-circuit voltage for a given redox couple; R, T, n, and F represent the universal gas constant, temperature, number of electrons transferred, and Faraday's constant, respectively. Assuming reactant activities of 1, partial pressures of hydrogen (p_{H_2}), oxygen (p_{O_2}), and water vapor (p_{H_2O}) are used for the gaseous species. η_a can be described by the concentration independent Butler-Volmer equation, calculated as a function of current density (j) using, $\eta_a = \left(\frac{RT}{nF\alpha j_0}\right)\ln\left(\frac{j}{j_0}\right) - \left(\frac{RT}{nF(1-\alpha)j_0}\right)\ln\left(\frac{j}{j_0}\right)$. α is the charge transfer coefficient, which represents the symmetry (or lack-thereof) of the forward and reverse electrochemical reactions, taking a value $0 < \alpha < 1$. α is a fitting parameter in our model. It is challenging to measure and only limited reports of direct measurement exist in high temperature fuel cells. Therefore, we have adjusted α to fit experimentally measured data (noted in the appendix) and it is consistent with values reported in the literature ranging from 0.3 – 0.6 in the temperature range studied here. The exchange current density (j_0), or current expected at no applied voltage, was

extracted from oxygen reduction reaction (ORR) data in the literature.[88] η_Ω is taken as the product of the current density (j) and the area specific resistance $\left(R_{ASR} = \frac{h}{\sigma_i}\right)$ with h and σ_i representing film thickness and ionic conductivity, respectively. η_c is not observed experimentally, therefore we have removed it from the analysis. Our model appears to fit the data in this study and others well indicating this is a reasonable modification. Though YDZ is widely studied, σ_i varies considerably in thin films due to interface, strain, and impurity considerations. Thus, we have used values consistent with the range found in thin film YDZ, recently reviewed by Jiang and Hertz.[89]

To demonstrate the effect of electrode morphology, we implemented our empirically derived electrochemical model parameters with a modified expression outlined in Ref. 90 for the area specific resistance, $R_{ASR} = \frac{h}{\sigma_i} + \frac{b}{\sigma_i}\left(\frac{b/d - 1}{d/b + 1}\right)$,[90] where b and d represent electrode particle spacing and size, respectively. The effect of electrolyte scaling is strongly affected by electrode geometrical parameters, i.e. microstructure, in such an analysis. The expression for R_{ASR} diverges in the 100 nm thickness regime for $d > b$, which may indicate the inability for a single parameter to completely capture the nature of electrode microstructure on electrolyte thickness scaling adequately. The expected power appears to level off in the sub-100 nm electrolyte thickness range for the case of electrodes exhibiting $d < b$, however an ideal microstructure ($b \sim d$) reduces the previous expression to $R_{ASR} = \frac{h}{\sigma_i}$, which qualitatively matches the scaling behavior that is observed when implementing the parameters obtained in the electrochemical model derived from the experimental data presented herein.

3.2.2 Physical modeling

In order to determine the limitations of electrolyte thickness reduction we model the mechanisms of electronic leakage in an insulating thin film. The transference number of an ionic conductor is defined as, $t_i = \frac{\sigma_i}{\sigma_i+\sigma_e}$, where σ_i and σ_e are the ionic and electronic conductivities, respectively. For the following discussion, YDZ is assumed to have $t_i \sim 1$ across the entire temperature (573 < T < 773 K) and oxygen partial pressure ($10^{-19} < p_{O_2} < 10^{-1}$ atm) range, which is reasonable considering its wide electrolytic domain.[91] This aspect and deviation from ideality is discussed in more detail in Section 3.4. Pt is taken as both electrodes having $t_i \sim 0$, in accordance with experiments in the literature for isolating the role of electrolyte thickness.

The total electronic leakage current density in the insulating electrolyte will be expressed by the sum of individual components,[92] $j_e = j_{FP} + j_{FN} + j_\Omega$, where j_{FP}, j_{FN}, and j_Ω represent current from Frenkel-Poole emission, Fowler-Nordheim tunneling, and Ohmic components, respectively. We do not explicitly consider thermionic emission as it is unlikely in the temperature range of interest (573 K < T < 773 K) and Pt is not a good thermionic emitter.[93] A carrier mean free path in YDZ (effective mass ~$20m_0$)[94] at such low potentials is likely less than 1 nm; as such, ballistic transport is not relevant in this system.

j_{FP} accounts for emission of carriers in trap states promoted by a field enhanced thermal excitation. Current density from Frenkel-Poole emission was estimated following the work of Sze on insulating Si_3N_4 films,[95] $j_{FP} = CE \exp\left(\frac{-q\left(\phi_B - \sqrt{\frac{qE}{\pi\varepsilon_0\varepsilon_d}}\right)}{kT}\right)$ where q, C, ε_0, and ε_d represent the electronic charge, a proportionality constant that is a function of the density of trapping states, the permittivity of free space, and the dielectric constant of YDZ, respectively. The electric field, E, is

given by the cell voltage (V_{cell}) over the film thickness (h), or $E = \frac{V_{cell}}{h}$. We assume a homogenous field across the material and hence the field strength scales with thickness. ε_d of YDZ as a function of temperature was obtained from the literature.[96] ϕ_B is the barrier height of the trap state to which it is assumed a carrier has been promoted into. We have used the shallowest traps reported in the literature, $1.4 < \phi_B < 3.2$ eV below the conduction band,[97] for YDZ to obtain the highest current possible, thereby giving a conservative estimate for power loss. These states are the result of trapped electrons at Zr^{3+} sites bound by surrounding oxygen vacancies.[97] For reference the band gap of YDZ is ~5 eV. As we have noted previously, SOFCs must operate in different gaseous environments and at elevated temperature. The band gap of an insulator will decrease slightly in the temperature range studied here and for YDZ it can increase in hydrogen environments.[98, 99] However, the most important aspect is the trap state density and its position with respect the conduction band edge at elevated temperature and different environments. While this is not explicitly accounted for, the shallow trap state (1.4 eV) likely acts as a conservative estimate in our approach. In accordance with Sze,[95] we take C~10^{-3} (A/cm)/V since there appears to be no data in the literature regarding the density of traps in YDZ at elevated temperature and varying partial pressure environments. We note that C is linearly proportional to j_{FP}, all else constant. Thus a more accurate value of j_{FP} would be possible provided a precise estimation of C, however we note that even modulating C by several orders of magnitude would still result in power loss from j_{FP}being less than from Ohmic processes.

The Fowler-Nordheim tunneling current was found assuming free carriers at the Pt/YDZ interface using the following relations,[100, 101] $j_{FN} = \gamma E^2 \exp\left(\frac{-\beta}{E}\right)$. The expressions for γ and β are as follows, $\gamma = \frac{q^3}{(8\pi h m^* \phi_B)}$ and $\beta = \frac{8\pi\sqrt{2m^*\phi_B^3}}{3qh}$ where h is Plank's constant and m^* is the effective carrier mass in YDZ. The dominant minority carrier can be an electron or hole depending on the

oxygen partial pressure conditions of YDZ at elevated temperature.[91] It is assumed that $m^* \sim 20 m_0$ is equivalent for both carriers.[94] We did not take the effect of temperature into account for tunneling current based on the assumption that $\frac{V_{cell}}{kT}$ is large enough to neglect T dependence.[100] The maximum tunneling current was found to be on the order of 10^{-12} A/cm^2 for $h = 1$ nm.

j_Ω is important at low voltages and high temperatures, as in the case of a SOFC, and electronic current is driven by hopping of thermally activated electrons. However as discussed previously, we take $t_i \sim 1$ for YDZ, therefore, electrons are minority carriers. j_Ω can be expressed as the product of electric field and conductivity. The temperature and partial pressure dependence of electrical conductivity used to estimate electronic Ohmic loss is based on the empirical expression,[91] $\sigma_e = 1.31 \times 10^7 \exp\left(\frac{-3.88}{kT}\right) (p_{O_2})^{-1/4}$. σ_e is dependent on p_{O_2}, thus a range of conductivities may be expected across the electrolyte operating in the $10^{-19} < p_{O_2} < 10^{-1}$ regime. We used the lowest p_{O_2} to maximize σ_e, thereby giving a conservative estimate for power loss. In polycrystalline YDZ, point defects and impurities tend to segregate in grain boundaries,[102] rendering these regions locally electrostatically positive and leading to increased electrical conductivity, or $t_i < 1$, as a function of grain size.[103] We consider mixed conductivity in Section 3.4 since j_Ω appears to be the most significant form of electronic leakage. When adjusting the ionic transference number, the total current density was kept constant and the additional electronic conductivity was modeled as leakage current which reduces the OCV proportionally following Wagner's equation, thus giving an estimate of lost potential power output.

Lastly, we consider dielectric breakdown of the insulator. As described earlier, YDZ has a wide electrolytic range, enabling high chemical stability. At elevated temperatures and large electric fields, dielectric breakdown of YDZ most likely occurs due to thermal or electrical breakdown.[104] At

a given temperature for an insulating film undergoing thermal breakdown, there is little or no thickness dependence for the maximum dielectric field strength, E_d.[95] Thermal breakdown occurs when the heat generated by the electric field induced leakage current exceeds the heat transferred by the material to its surroundings. This relationship leads to a function independent of film thickness which describes the maximum dielectric field strength, E_d, as a function of ambient temperature,[95] $E_d \sim \frac{\pi \varepsilon_0 \varepsilon_d}{q}(\phi_B - AT)^2$, where A is given by a function weakly dependent on T and E_d that can be solved numerically. We find $A \sim 10^{-4}$ V/K, in reasonable agreement with previous work on insulating thin films.[95] Similar to the discussion above, $1.4 < \phi_B < 3.2$ eV, in accordance with optical studies on trap states in YDZ.[97] We estimate E_d to be 8.7, 7.6, and 6.6 MV/cm for temperatures of 573, 673, and 773 K, respectively. Experimentally, studies characterizing the dielectric loss mechanisms of YDZ membranes indicate that electronic leakage is the dominant loss mechanism at SOFC operating conditions.[54] Therefore, to set a conservative range of thickness values where breakdown is expected, we note that room temperature experimental data on electrical breakdown in bulk YDZ (8 mol% doping) suggests $E_d \sim 2$ MV/cm.[105] Using this value as an upper estimate and $V_{cell} = 1.2$ V, the critical thickness range for dielectric breakdown was found to be $1.3 < h <$ 5.5 nm based on thermal and electrical breakdown, respectively.

3.2.3 Experimental fabrication

YDZ electrolyte films were grown by radio-frequency sputtering at a power of 100 W from a stoichiometric 8mol% Y_2O_3 doped ZrO_2 target in 0.53 Pa Ar at a substrate temperature of 550 °C. The corresponding deposition rate measured by x-ray reflectivity was 1.2 nm min^{-1}. As discussed in Chapter 2, films deposited under these conditions led to the proper compressive stress regime necessary for free standing membrane stability. Porous Pt films were grown from an elemental Pt target by sputtering in 10 Pa Ar without substrate heating.

Plane view transmission electron microscope (TEM) samples were prepared by manual polishing of the underlying substrate, then ion milling to electron transparency using a Fischione 10-10 dual-beam ion mill. A JEOL 2100 was used to investigate the local grain structure and crystallinity of YDZ electrolyte films. A Zeiss Supra 55VP scanning electron microscope (SEM) was used to characterize the porous electrode structure of the SOFCs. Quantitative porosity investigations were possible due to the single layer, nano-structured thin films grown. Porosity estimates were made by converting SEM micrographs to binary images, thresholding, and gathering pixel ratios with the National Institutes for Health software, ImageJ. SOFC devices were produced in a similar fashion to the membranes described in Chapter 2: patterning of double side Si_3N_4 coated Si wafers with photolithography, removal of patterned Si_3N_4 by reactive ion etching, selective area etching of exposed Si with a 30 wt. % KOH aqueous solution, deposition of YDZ electrolyte and Pt cathode on the free standing planar Si_3N_4 membrane surface, removal of Si_3N_4 from the below by reactive ion etching, and finally deposition of the Pt anode on Si well side. SOFC performance was tested in a custom dual-chamber measurement station (see Appendix) with argon carrier gas containing 5 % wet hydrogen as fuel and stationary air as the oxidant.

3.3 A mechanistic route to high performance fuel cells

A plane view bright field transmission electron microscope (TEM) image in Figure 2 shows the nano-granular structure of the YDZ electrolyte thin films. The average grain size was estimated to be approximately 20 nm. The high resolution TEM image (Figure 2c) indicates that there are no visible amorphous intergranular impurities in the films, while the selected area electron diffraction pattern (Figure 2b) confirms that the YDZ films are single phase and cubic.

Figure 3- 2: TEM characterization of YDZ

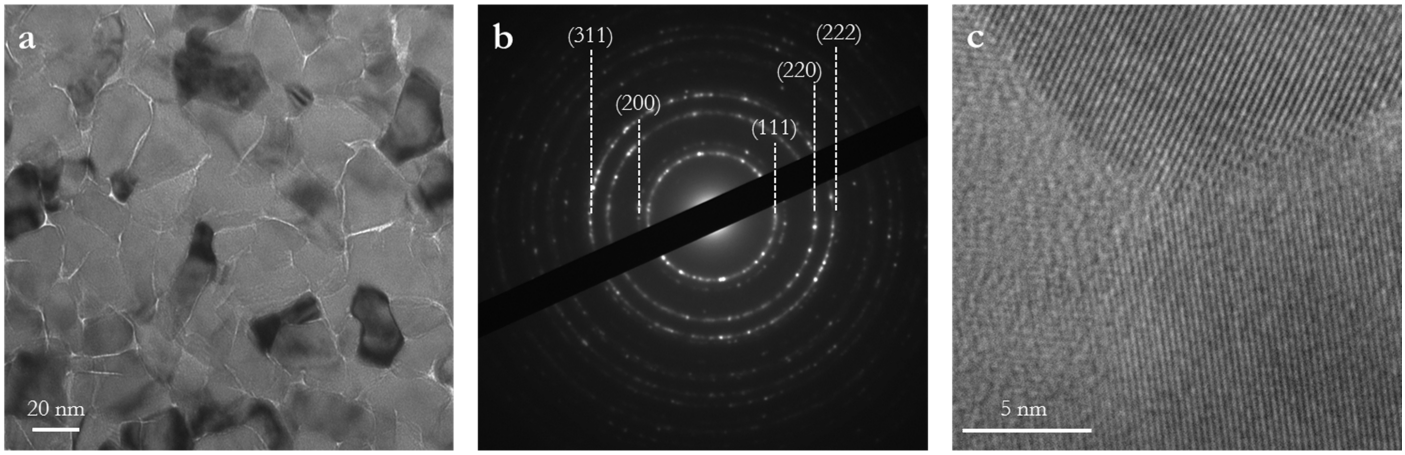

(a) *TEM image of the nano-granular structure of YDZ thin films;* ***(b)*** *SAED pattern of YDZ indicating polycrystalline behavior and indexed to a cubic lattice; and* ***(c)*** *high resolution TEM image of a triple point where three grains converge to form a grain boundary.*

3.3.1 Electrode and electrolyte considerations

Figure 3 shows a schematic of the fuel cell structure used to test SOFCs in this chapter. The electrocatalyst used as both the anode and cathode in this study was Pt.

Figure 3- 3: Fuel cell schematic

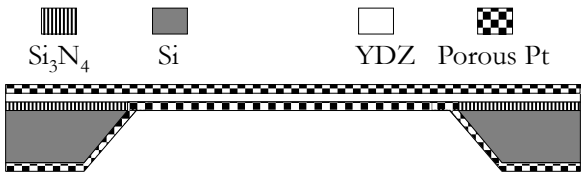

A cross-sectional schematic of the fuel cell structure used to test the model Pt|YDZ|Pt system.

It should be noted that although Pt may be a cost prohibitive catalyst for widespread use, a total Pt loading on each electrode of less than 1.7 $\mu g/cm^2$ was used for the SOFCs studied. As a rough comparison, conventional proton exchange membranes typically use Pt loadings in the hundreds of $\mu g/cm^2$ range.[106, 107] In addition, by using Pt, de-convolution of possible reaction mechanism

pathways is greatly simplified. Since the purely metallic catalyst electrode does not allow for ionic conductivity, there can be only one dominant path for O_2 reduction at the cathode and H_2 oxidation at the anode, namely at the TPBs. To study the effect of electrolyte thickness, a series of three SOFCs with YDZ membrane thicknesses of 27, 54, and 108 nm were fabricated with similar Pt electrodes. The open circuit voltage (OCV) under measurement conditions of these SOFCs is shown in Figure 4a, while Figure 4b illustrates an optical micrograph of the fabricated stack showing a characteristic compressive buckling pattern for the tri-layer structure, similar to YDZ membranes described in Chapter 2, indicating little mechanical influence from the porous metal electrodes.

Figure 3- 4: OCV of SOFCs with YDZ membranes

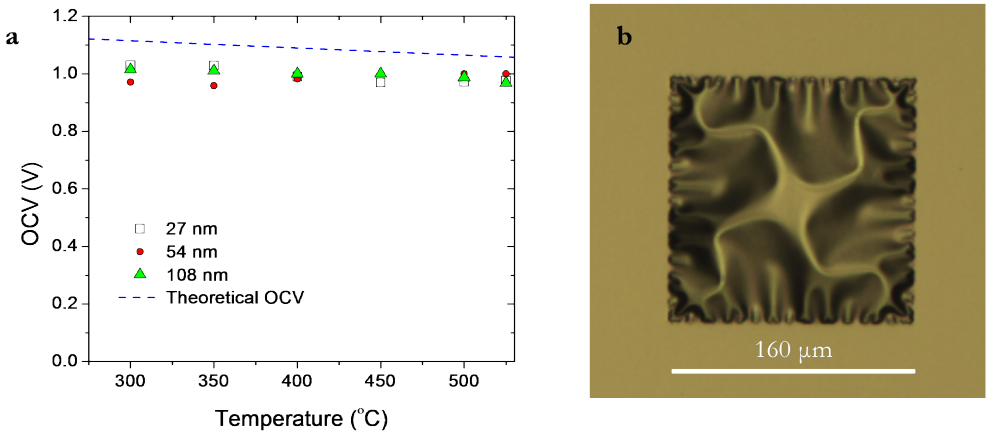

***(a)** A plot of the OCV for model Pt|YDZ|Pt SOFCs with varying electrolyte thickness; and **(b)** a tri-layer free standing structure with 108 nm thick YDZ displaying a common buckling pattern.*

The closeness of the OCVs to the thermodynamic limit in the temperature range tested confirms the high quality electronic insulating nature of the free standing YDZ electrolyte membranes, which is essential for high-performance fuel cells. We do note that one can see variation in the OCV, including deviations from the Nernst potential of up to 200 mV. Reasons for this deviation may be related to slight fuel leakage between the anode and cathode due to minor microstructural defects

subsequently annealed out or testing apparatus sealing variation. However, even in the case of the 27 nm thick YDZ membrane SOFC, an excellent chemical potential is maintained throughout the temperature range investigated.

To evaluate the significance of overall electrode porosity on SOFC performance, several different Pt electrodes were synthesized. Figure 5a illustrates the relationship of Pt film thickness to porosity for films grown under similar conditions in both the cathode and anode. Since the average pore size for all samples was approximately equal to within one standard deviation, the total porosity is an indication of overall TPB length. It can be seen that the different electrodes exhibit markedly dissimilar trends in porosity. This is a direct result of the micro-fabrication method used to synthesize the electrolyte membranes, as it is well known that the deposition surface and atmosphere play a key role in the structure of thin metallic films on oxides.[108] As described in Section 3.2.3, the cathode deposition is on a planar surface, whereas the anode deposition occurs within a confined Si well after patterning. Therefore, it is not unreasonable to expect different adatom arrangement processes for the anode and cathode. 80 nm Pt electrodes were used to further investigate the effect of electrolyte thickness on SOFC performance. Figure 5b shows the relationship of electrolyte thickness and maximum power density at several temperatures. It can be seen that there is not a simple monotonic relationship with increasing temperature. In the low temperature regime, it appears that YDZ at the intermediate thickness of ~50 nm gives maximal performance, similar to reports in the literature.[109] However, there is a clear shift that occurs at higher temperatures, in which thicker YDZ of ~100 nm performs much better. This result is counterintuitive, as one may expect a proportional relationship between scaling of electrolyte thickness and performance. The origin of this aspect is likely related to physical leakage mechanisms described in Section 3.2.2 and 3.4.

Figure 3- 5: Pt electrode characteristics

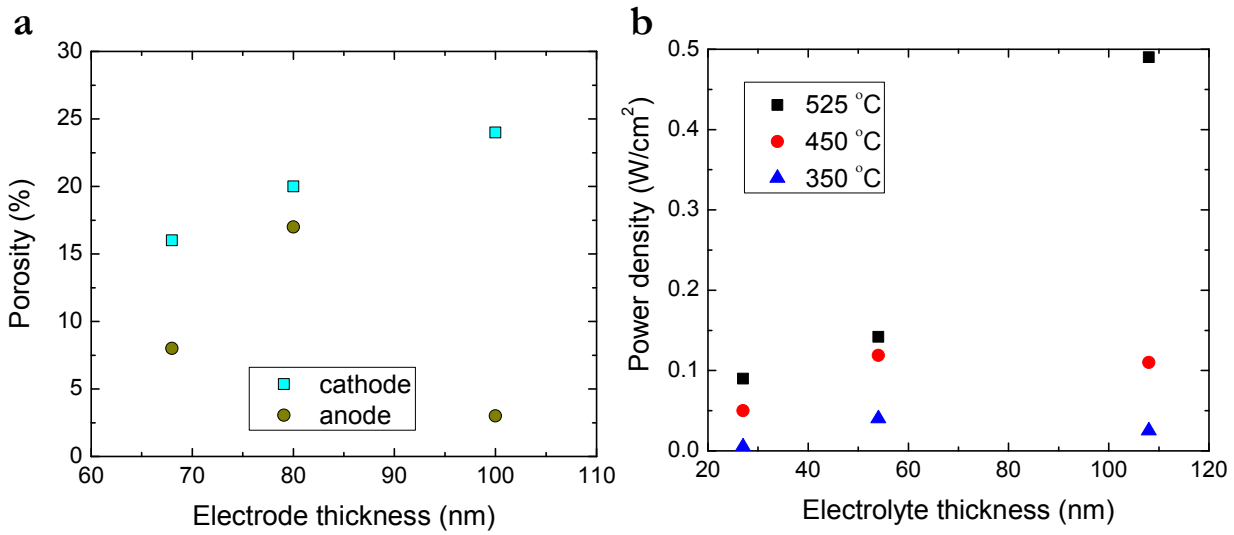

(a) *Effect of Pt thickness on porosity for the cathode and anode in Pt|YDZ|Pt SOFCs; and* ***(b)*** *effect of electrolyte thickness on 80 nm Pt electrodes in Pt|YDZ|Pt SOFCs at 350 °C, 450 °C, and 525 °C.*

To demonstrate the significance of TPB length in porous electrode structures for thin film SOFCs, using the 108 nm thick YDZ electrolyte, two alternate anodes were grown. Figure 6a–d shows the SEM micrographs and accompanying binary converted images (thresholded) of two different 80 nm Pt anodes after measurement having similar total porosity, but distinctly different average pore size. The total perimeter of porous regions, i.e. TPB length, in the Pt film with smaller average pore size is larger than that of its counterpart. Since the only reaction pathway for the anodic reaction, $H_2 + O^{2-} \rightarrow H_2O + 2e^-$, occurs at the TPBs and both porous Pt electrodes are well interconnected, it is follows that exchange current density and TPB length will be directly proportional. Thus, by augmenting the TPB length in the SOFC anode, one can expect a direct performance output enhancement. We have experimentally isolated the role of the TPB in the anode by leaving the Pt cathode structure unchanged for the two SOFCs under comparison.

Figure 3- 6: Optimized Pt microstructure

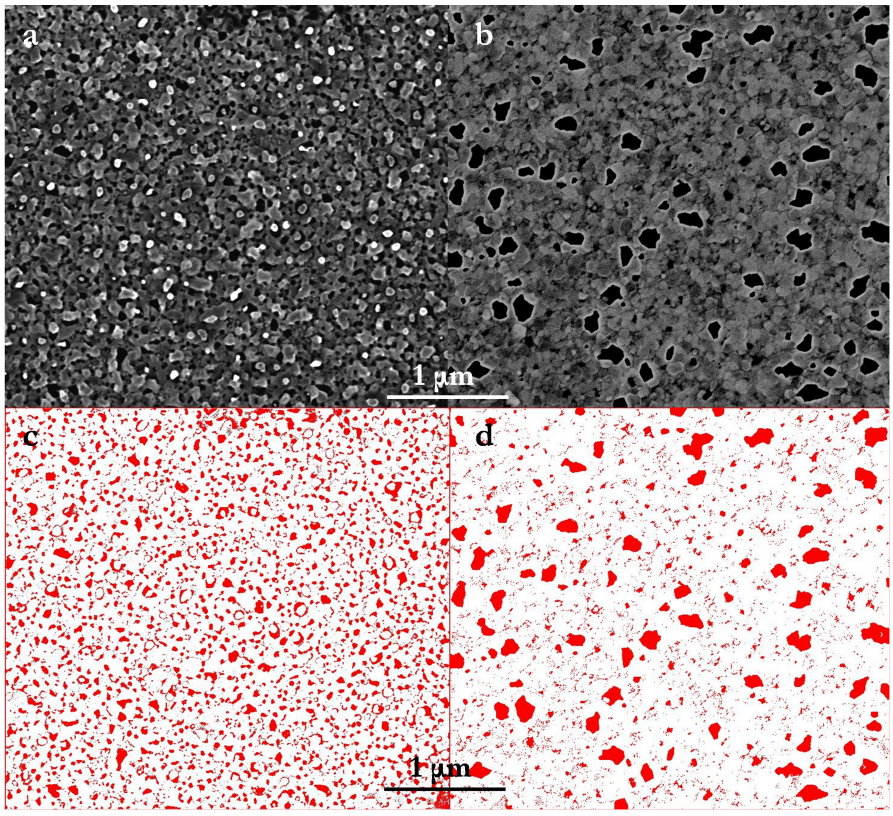

Post fuel cell measurement SEM micrographs and corresponding binary converted image of anode with ***(a)****,* ***(c)*** *increased TPB perimeter having a higher fraction of porosity per unit area and* ***(b)****,* ***(d)*** *standard porosity.*

In Figure 7 we report the maximum power density obtained at 500 °C for two cells with similar total porosity in the anode and cathode, but different TPB length on the anodes. Over a two-fold increase in power density is observed by reducing the average pore size and therefore increasing the TPB length. A power density of 1037 mW cm^{-2} was obtained at 500 °C in this near-ideal thin film SOFC structure with an OCV of 0.968 V.

Figure 3- 7: High performance Pt|YDZ|Pt cells

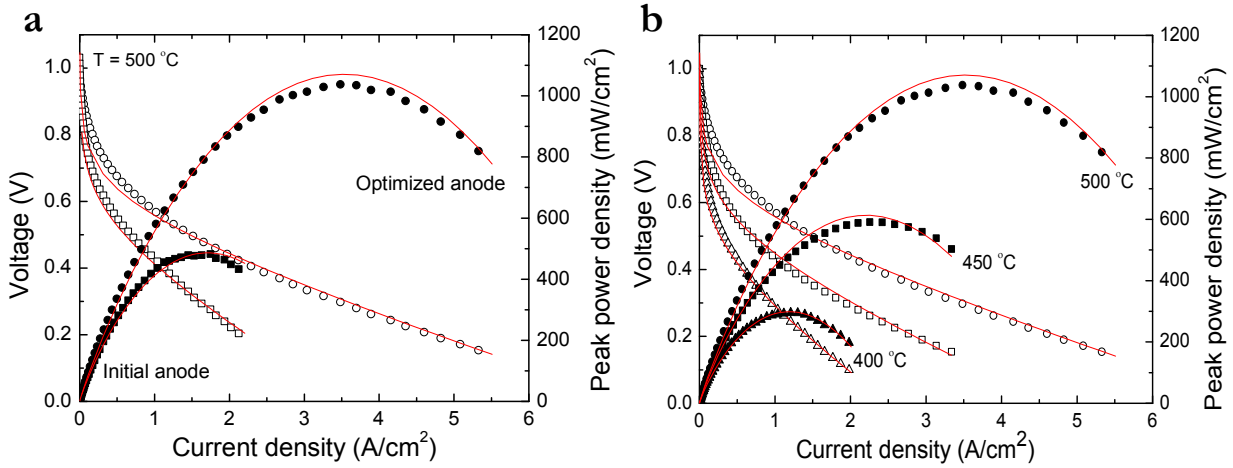

(a) *A comparison of the performance of cells having the same cathode microstructure, electrolyte thickness, but different anode porosity; and* ***(b)*** *the peak power density of a SOFC with optimized Pt anode microstructure and 108 nm YDZ electrolyte. The symbols are experimental data and the red lines are model fits.*

3.3.2 Long term stability

In the case of metal electrodes, such as those used in these model demonstrations, only the TPBs are active reaction sites for oxidation and reduction. Consequently, engineering of the microstructure to create optimal porosity in the electrodes while maintaining an electrically interconnected network is of essence. However, for long term device stability this microstructure must remain intact. We tested this aspect by leaving the SOFC devices at constant temperature for 12 hours. Figure 8 shows the evolution of the SOFC OCV and power density as a function of time, while being held at a constant temperature of 400 °C. It can be seen that the potential across the SOFC is relatively stable, indicating that there is little change in the dense electrolyte membrane separating the anode and cathode. On the other hand, by observing the power density variation, it is clear that there are substantial microstructural changes occurring in the device components.

Performance degradation is seen, indicating instability in the electrode microstructures. After 12 hours of testing, the power density of the cell dropped to about 50 % of its initial value.

Figure 3- 8: Isothermal stability of Pt|YDZ|Pt SOFC

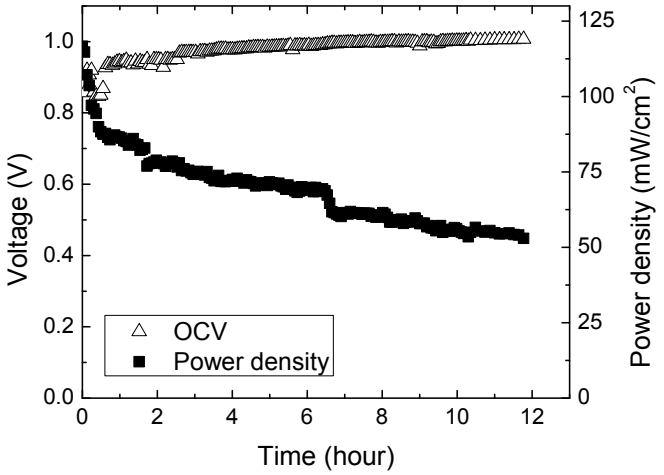

Overall performance and OCV of a Pt|YDZ|Pt SOFC at 400 °C operating continuously for 12 hours with 5% wet H_2 as fuel. Open and closed symbols are for voltage and power density, respectively.

SEM micrographs of the anode and cathode are shown as-deposited, after initial heating to temperature, and at 6 hour intervals in Figure 9a-h. It should be noted that the cell used for microstructural investigation by SEM was not the same cell used for performance measurement, therefore, only the effect of elevated temperature in a reducing or oxidizing environment can lead to the origin of the microstructural change observed in Figure 9. However, it is known that current density in Pt, specifically at TPB interfaces, can play additional role in morphology changes.[110]

Figure 3- 9: SEM microstructure of Pt electrodes

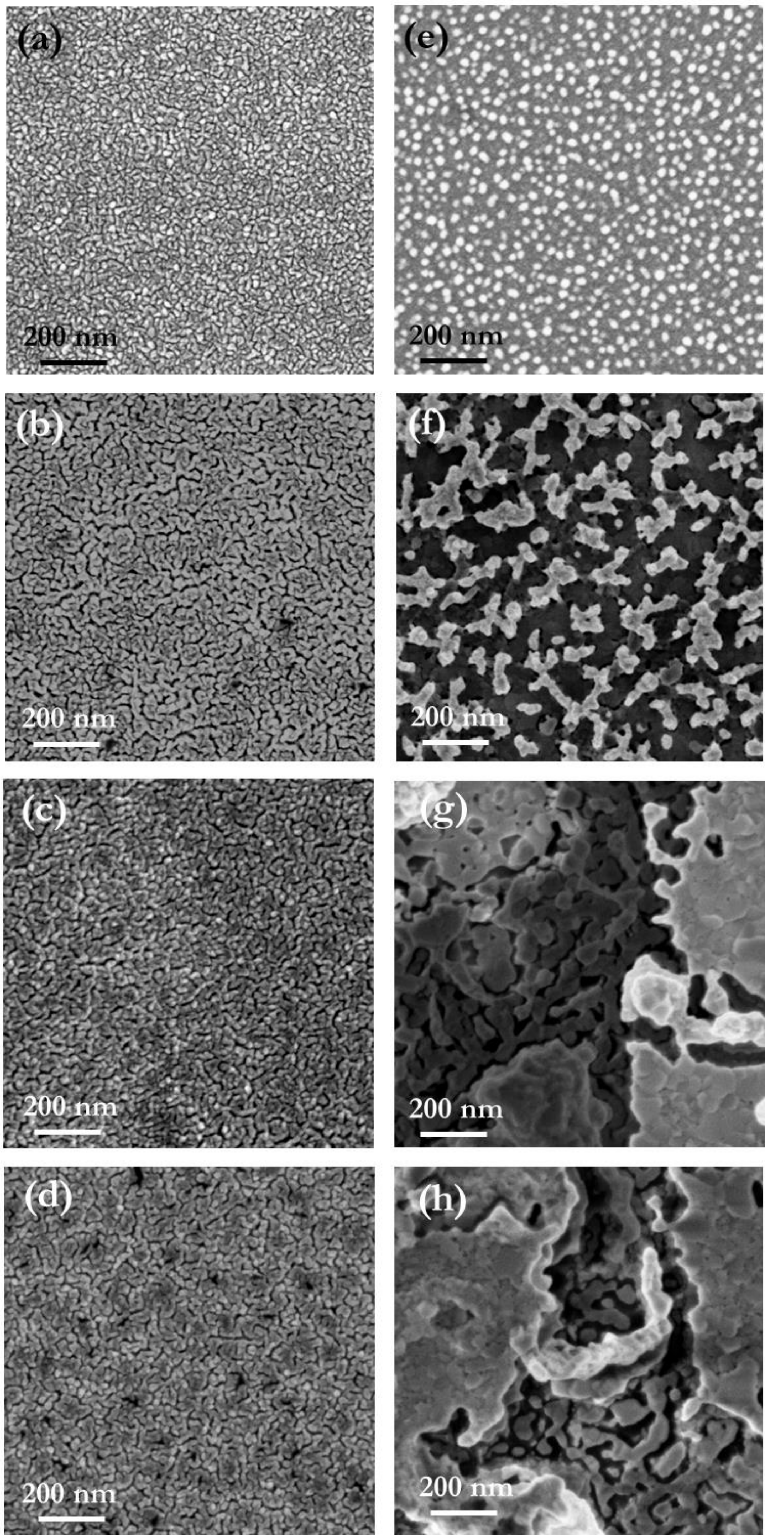

(From top to bottom) SEM micrographs of the cathode ***(a)-(d)*** *and anode* ***(e)-(h)*** *as-deposited, heated up to 400 °C, 6 hours at 400 °C, and 12 hours at 400 °C.*

There is a difference between elevated temperature exposure on the anode and cathode. In air, the cathode seems largely unaffected by the high temperature anneal. Conversely, the anode goes through very interesting microstructural changes, likely due to the coupled effect of elevated temperature and a reducing environment. As seen in the SEM micrographs of the anode, Pt coarsening induced by surface energy minimization results in a large decrease in overall porosity. This leads to the catalytic properties for oxidation associated with Pt/YDZ boundaries being reduced and is manifested by a lowering of measured power density. Previous studies on Pt films on rigid substrates highlight the microstructural instability under SOFC operating conditions,[110, 111] however there has been success in utilizing the de-wetting effect to form regular and stable patterned Pt.[112] Further, it has been shown that alloying Pt with small amounts of Ni doping may enhance its high temperature stability.[113]

To quantify the TPB density and provide justification for random porous networks as high performance electrode materials, take the total number of circular pores in a square area (such as SEM images) as $N_p = \frac{L^2 f_p}{\pi r^2}$ where L is the length of the area analyzed, f_p is the areal fraction of pores or $\frac{\sum pore\ area}{total\ area}$, and r is the average pore radius. It follows that the total TPB length per unit area can be expressed as $L_{tpb} = \frac{N_p}{L^2} 2\pi r = \frac{2 f_p}{r}$. From the thresholded SEM image in Figure 5, r~9 nm and f_p is estimated to be ~20%, resulting in L_{tpb}~ 444,444 cm/cm^2. Characterization techniques developed for traditional SOFC anodes using a combination of SEM, focused ion beam etching and mathematical modeling results in L_{tpb} in the range of 800,000 cm/cm^2 after operation.[27, 114] Alternative experimental approaches to develop regularly patterned metallic electrodes that have been shown to be morphologically stable at elevated temperatures such as nano-sphere lithography,[115-117] exhibit maximum pattern densities of ~43,000 cm/cm^2. Thus, at present random porous networks are over an order of magnitude better in terms of reaction site availability. The

difficulty in optimizing parameters for ideal electrode structures is due to the fact that three components, namely perimeter coverage, surface interconnectivity, and TPB length, must be tuned simultaneously even though they are all functions of electrode thickness. Each component is necessary for current extraction and adequate reactive areas for high performing fuel cells. This is schematically shown in Figure 10. Obtaining the high performance reported in this Chapter and Chapter 5 are a result of parametric experimental optimization.

Figure 3- 10: Complexity in metallic electrode optimization

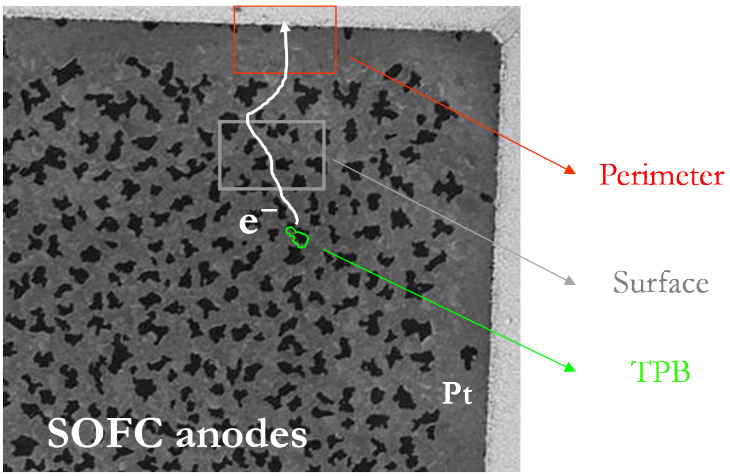

A SEM image of a Pt anode on the backside of a free standing YDZ membrane depicting the three components determining electrode performance, all of which are dependent on deposition conditions such as pressure and thickness.

3.4 Scaling behavior and limitations of ultrathin electrolytes

Using the model experimental platform discussed above, we simulate the fuel cell current-voltage behavior using expressions outline in Section 3.2.1.

3.4.1 Model fit to experimental data

Figure 11 shows model (red line) results and experimental data discussed in Section 3.3. A good fit to the data is shown, implying that the model adequately captures the electrochemical aspect of the SOFC behavior.

Figure 3- 11: Model fits to Pt|YDZ|Pt data

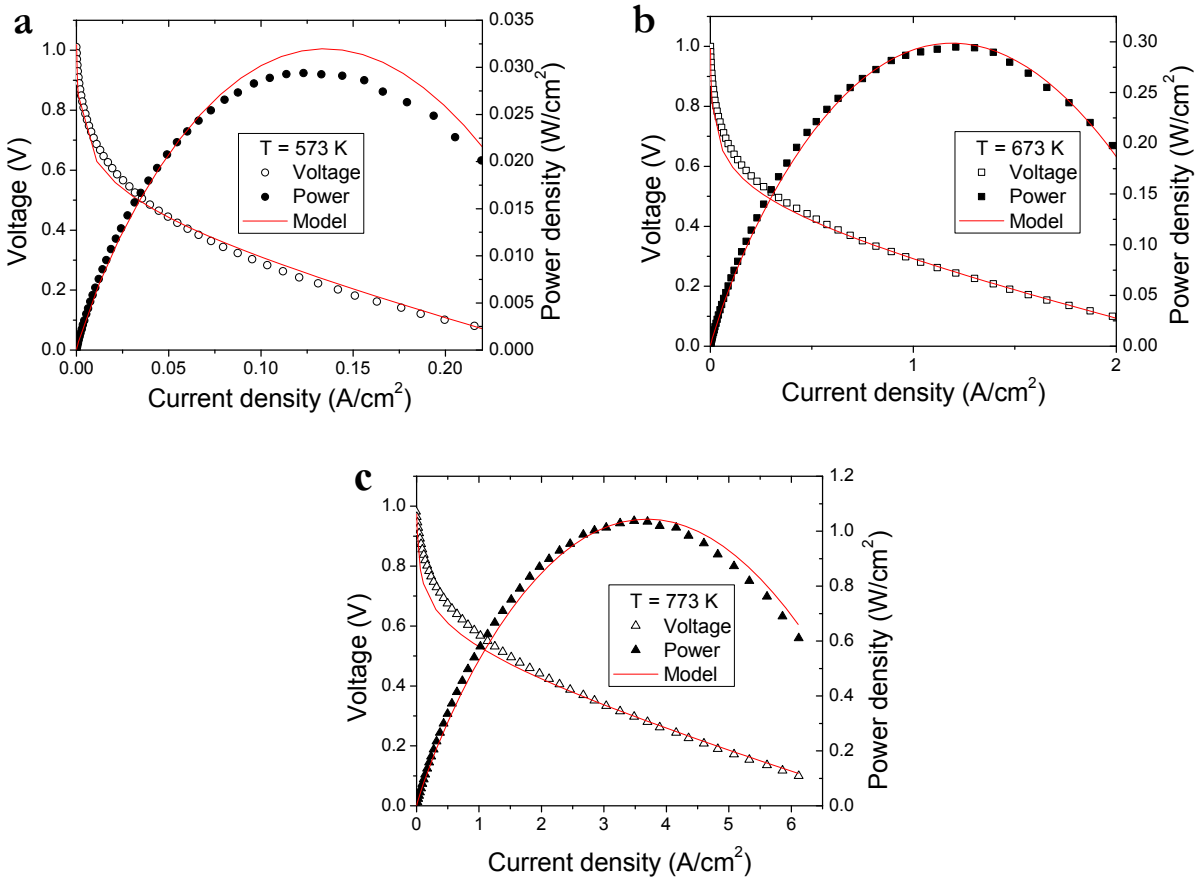

Example current-voltage and current-power curves from Section 3.3 modeled with the expressions outlined in Section 3.2.1 at (a) 573 K, (b) 673 K, and (c) 773 K. The specific electrochemical parameters and inputs used are listed in the Appendix.

Using these empirically fit inputs, the model can be extended to determine the scalability of the high performance SOFCs as the electrolyte thickness is reduced further. In doing so, there are

two criteria for the area specific resistance (ASR) term, which is the key contribution to the Ohmic resistance across the electrolyte. In Figure 12a the influence of electrode morphology, specifically, where b (500 nm) < d (800 nm), b (500 nm) ~ d (500 nm), and b (500 nm) > d (200 nm). As alluded in Section 3.2.1, it can be seen that nanoscale electrodes are desirable and the current relationship for ASR with electrode contributions does not adequately cover the entire phase space.[90] In particular, when particle size exceeds particle spacing, the ASR drops dramatically and the power density diverges, leaving the function of little use in the sub 100 nm thickness range. On the other hand, when the electrode particle size is less than the particle spacing, there appears to be no added benefit to reducing electrolyte thickness. However, when the electrode particle size is approximately equal to the particle spacing, the ASR reduces to the case which we have fit to the experimental data in Section 3.3, shown in Figure 12b with other independent high performance SOFCs integrating nanoscale YDZ electrolyte membranes. As shown, this criterion appears to be the most accurate fit for scaling the performance into the nanometer electrolyte thickness regime.

Figure 3- 12: Scaling of power density in SOFCs with ultrathin electrolytes

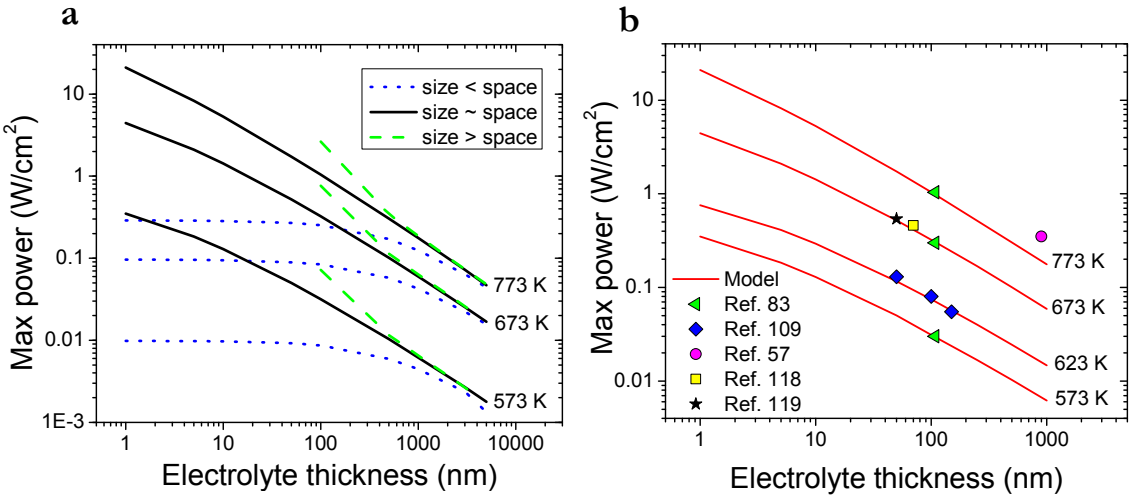

(a) *An alternative approach for a modified area specific resistance term from the literature showing three curves that exemplify the sensitivity to geometrical electrode characteristics such as particle size and particle spacing;*[90] ***(b)*** *the*

maximum power density of state-of-the-art Pt|YDZ|Pt fuel cells using the empirically derived model parameters as a function of electrolyte thickness at several temperatures along with reference data from the literature.[57, 83, 109, 118, 119] *We note that reference data is independent of the parameters used in our model and that Refs. 118 and 119 utilize a yttria-doped ceria interlayer of 6 and 10 nm, respectively.*

As noted in the previous section, the experimental data from this thesis and those shown in Figure 12b utilize metallic electrode as proof-of-concept demonstrations. Therefore, this scaling behavior serves as an upper bound to what can be expected when oxide electrodes are integrated, since additional kinetic, Ohmic, and charge transfer losses may become significant. Furthermore, this type of behavior has assumed a perfect electronic insulator and ionic conductor. The following section will explore the deviation from this physical ideality.

3.4.2 Physical loss mechanisms

Figure 13 presents all of the electronic loss components described in Section 3.2.2 for two different trap states and transference numbers.

Tunneling current results in negligible power loss, and is active at thicknesses that are inconsequential due to limitations set by dielectric breakdown. The dielectric breakdown (by electrical breakdown) sets the limit for minimum suitable electrolyte thickness, which is approximately 6 nm in this study. Emission processes, whether by Schottky or Frenkel-Poole mechanisms, are of less consequence compared to Ohmic loss when ϕ_B= 3.2 eV. If the potential barrier is reduced to a very shallow trap 1.4 eV below the conduction band (Fig. 4(b)) and it is assumed that carriers are excited to this state, emission losses become significant, though the maximum power lost at 773 K is on the order of 10^{-4} W/cm^2. However, this loss is naturally dependent on the distribution of trap states, which are not well characterized at present.

Figure 3- 13: Physical losses in ultrathin electrolyte

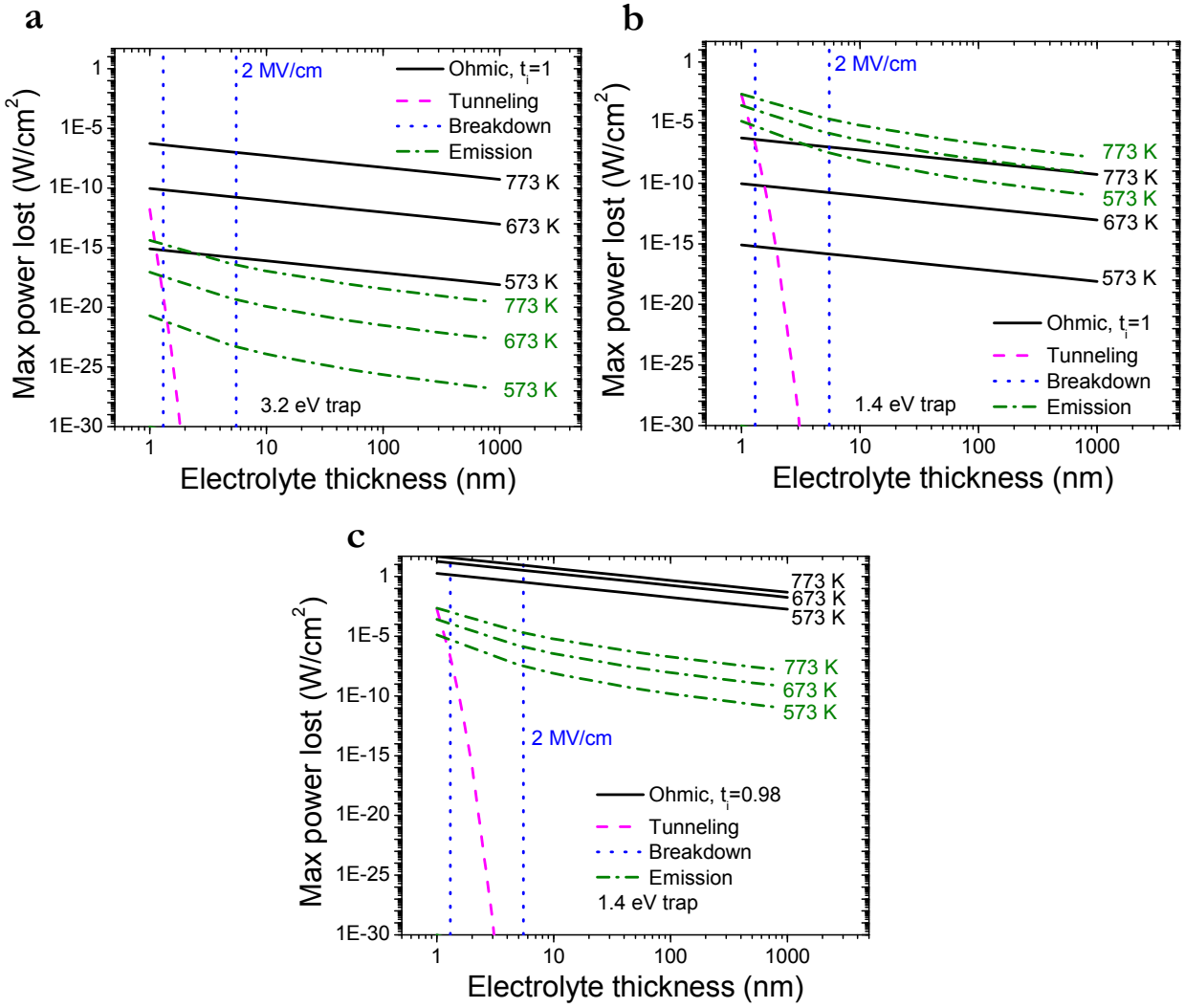

Plots of the electrical loss mechanisms leading to power dissipation by leakage through the electrolyte are shown; ***(a)*** *ideal case with YDZ exhibiting perfect ionic conduction and a trap state of 3.2 eV below the YDZ conduction band for tunneling and emission mechanisms;* ***(b)*** *ideal case with YDZ having* $t_i \sim 1$ *and a trap state of 1.4 eV; and* ***(c)*** *case with mixed electronic-ionic conduction* ($t_i \sim 0.9$) *indicating sizable power dissipation (on the order of* 10^{-1} W/cm^2 *at 10 nm) by electronic leakage and a trap state of 1.4 eV. Note that the Ohmic loss curves for 673 K and 773 K appear close on this scale. Blue lines for dielectric breakdown represent the range of critical fields from 2 – 8.7 MV/cm due to electronic and thermal breakdown, respectively.*

A sample set of data for 54 samples on the probability of observing high OCV characteristics for sputtered YDZ electrolyte membranes is shown in the Appendix. Ohmic contributions appear to be the most important fundamental loss mechanism as the dimension of the electrolyte is reduced. This loss is intimately linked to how t_i is modified in a particular temperature and partial pressure environment. For example, should there be thickness or grain size dependence on the electrolytic domain of YDZ, j_Ω could become significantly larger, thus reducing the expected power density of devices integrating the electrolyte. Figure 13b shows the results of increasing the fraction of electronic conduction by modifying $t_i \sim 0.9$, where appreciable power loss is observed at nanoscale thicknesses.

Thus, the major material concerns for electrolyte thickness reduction are dielectric breakdown strength and minimization of defects that could lead to mixed electronic-ionic conductivity. Mechanisms leading to mixed conductivity can be categorized by either macroscopic (structural defects) or microscopic (atomic scale defects) flaws. On the one hand, macroscopic defects such as pinholes or voids can be experimentally observed at low temperature by dielectric measurements such as capacitance and dielectric loss.[54] On the other hand, microscopic defects or impurities are only observable under measurement conditions (high temperature, large partial pressure gradient) and may lead to an increased concentration of promoted electrons to trap states in YDZ and higher concentrations of trap states, thus also decreasing the breakdown strength, emission losses, and limiting the critical thickness. Lastly, it is important to mention the statistical probability of encountering a critical defect that could be detrimental to the insulating nature of the solid electrolyte. This aspect has not been explored, but is inversely proportional to reduced thickness, i.e. for a given membrane area there is a higher probability of a critical defect that will short the device in thinner electrolytes. Therefore from an experimental perspective, multilayer thin film electrolytes combining directional deposition processes (physical vapor techniques) with

conformal coating processes (atomic layer deposition) can be excellent tools to avoid the aforementioned loss mechanisms and allow continued exploration further into the ultrathin electrolyte regime.[36, 57]

In Figure 14, we combine the results of this work into a potential power output space at 500 °C, showing the high and low boundaries for performance that can be expected as electrolyte thickness is scaled down to nanometer dimensions.[57, 60, 83, 120]

Figure 3- 14: Possible power output space for Pt|YDZ|Pt SOFCs

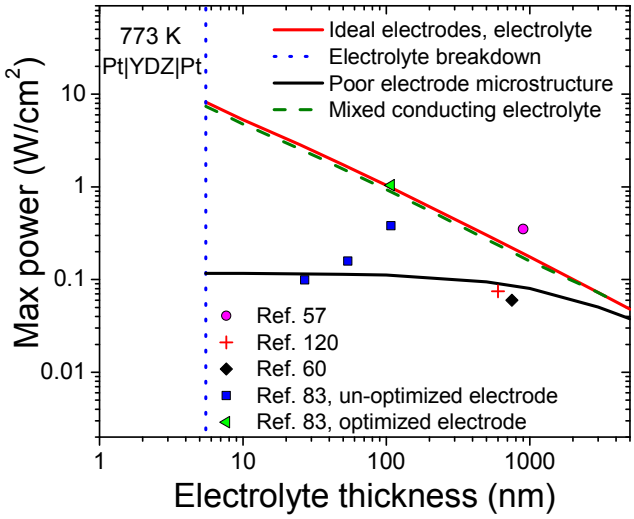

A graphical summary of the maximum power to be expected at 773 K as electrolyte thickness is decreased for $\sigma_i = 2\times10^{-4}$ *S/cm with data from the literature.*[57, 60, 83, 120] *The ideal case is a result of the model using the experimental parameters extracted from fitting data in Ref. 83 and is shown in Fig. 11 and 12b for other temperatures. The cut-off thickness shown is due to electrical breakdown at a critical field,* $E_m \sim$ *2 MV/cm. The mixed conducting electrolyte is characterized by* $t_i \sim$ *0.9. The non-ideal electrode case is based on the expression for* R_{ASR} *in Ref. 90 coupled with our model parameters, having 100 nm particles with a spacing of 500 nm. This boundary is tunable depending on electrode geometry as presented in Fig. 12a, which likely explains the scatter in reported results.*

The high limit is based on the empirical parameters from the model developed in this chapter. Therefore, the results have experimental evidence supporting the expected scaling behavior. Ideal

electrodes and defect free electrolytes are necessary to reach the highest power densities achievable in the nanoscale regime. We note that the microstructure of metallic electrodes, like those used in the experimental demonstrations this work is based on, are unstable at elevated temperature and reducing environments,[83] rendering the operational durability of such structures quite low. Integrating oxide heterostructures that overcome thermomechanical and interface stresses for stable nanoscale membrane demonstrations will be vital to move beyond current state-of-the-art demonstrations.[121] Similar to a recent experimental evaluation of the long term use of thin film electrolytes for SOFCs,[122] we highlight the necessity of stable, nanostructured electrodes that can operate in the low temperature regime ($573 < T < 773$ K) enabled by ultrathin membranes to achieve power densities of several W/cm^2. The results presented in this study could serve as a benchmark that ideal oxide electrodes, both in material chemistry and microstructure, could aim to achieve using nanoscale electrolytes.

While the model appears to fit the best performing Pt|YDZ|Pt devices in the literature accurately and also provide fundamental origins for the observed scatter, there are limitations. We identify two main aspects, namely interface resistance and beneficial mixed conductivity. We have not explicitly considered any charge transfer resistance and assumed a free electron at the electrode-electrolyte interface. The charge transfer resistance at this interface is dependent on conduction band alignment, which is a function of both temperature and environment.[123] Further, physical mechanisms for charge spillover or microstructural changes during operation will affect its value.[124, 125] This aspect becomes even more convoluted as metallic electrodes are substituted with oxide electrodes.[126] These components would certainly reduce the anticipated maximum power density. We have modeled any mixed conductivity as a finite current loss that would reduce the total power density by decreasing the OCV and maintaining a similar current density to the ideal case. However,

if a large enough electronic current is driven in conjunction with an oxide ionic current, they migrate in the same direction. While it inherently reduces the OCV, it may increase the power density at the cost of decreased voltage efficiency. This has been experimentally observed in 100 nm oxide alloy electrolytes that exhibit an OCV of only 0.4 V at 773K, but still produce a power density of over 1 W/cm^2.[82] Therefore, similar to the tunable boundary resulting from electrode microstructure, power loss from a mixed conducting electrolyte will be dependent on the empirically derived expression for conduction of the minority carrier. Actual device applications will determine the range of useful voltages and power density values.

3.5 Conclusion

This chapter has shown that high performance SOFCs integrating ultrathin YDZ membranes requires electrode optimization towards large TPB lengths. Random networks of porous metallic electrodes (Pt) needed to drive high performance are microstructurally unstable in a high temperature reducing environment. Physical limits to dimensionality reduction were considered and electronic leakage by mixed conduction is the key loss mechanism that can dominate at very thin electrolyte dimensions. Dielectric breakdown sets the ultimate limit for functionality of ultrathin membrane based SOFCs.

4 SYNTHESIS AND INCORPORATION OF OXIDE ELECTRODES

4.1 Introduction

Currently, there is an effort to reduce the operating temperature of solid oxide fuel cells (SOFCs). High temperature operation (800–1000 °C) is beneficial in enhancing electrode reaction kinetics and reducing Ohmic resistance across the electrolyte; however, it also increases the possibility of parasitic reactions between cell components, requires high cost metallic interconnects, and creates sealing difficulty for stacking architectures. Reducing SOFC operation temperature is seen as a method to address the aforementioned shortcomings. To counteract the increased Ohmic resistance across the electrolyte during reduced temperature operation, SOFCs utilizing thin film electrolytes are being actively developed though most are in early stages and utilize Pt as both the anode and cathode.[37, 38] As discussed in Chapter 3, the limitation of Pt electrodes, typically synthesized with a porous microstructure, is their cost and microstructural instability due to the Ostwald ripening and dewetting effect.[83, 113] To be cost competitive and functionally reliable, reducing or eliminating Pt loading is of particular importance. We have focused on the cathode since at present no oxide anode material operable in the low temperature regime exists.

A significant barrier to replacing Pt is developing stable oxide electrode materials that have sufficient electronic and ionic conductivity, as well as high catalytic activity in the reduced temperature regime ($T < 500$ °C). In this regard, perovskite oxides that exhibit mixed conduction behavior have been shown to be some of the most promising cathode candidates. The perovskite structure is flexible with regard to doping various transition metals into A- and/or B-sites and can accommodate high oxygen deficiency, allowing the highly correlated ionic, electronic, and electrocatalytic properties to be delicately optimized.[127] Additionally, using thin film mixed

electronic-ionic conductors offers the benefit of extending the triple phase boundary (TPB) of SOFC devices to the entire plane of the cathode electrolyte interface for a dense film. Reactive area can be further enhanced by using a porous mixed conducting oxide. Two exciting material systems under investigation for applications as SOFC electrodes are $La_wSr_{1-w}Co_xFe_{1-x}O_{3-\delta}$ and $Ba_ySr_{1-y}Co_zFe_{1-z}O_{3-\delta}$.

$La_{0.6}Sr_{0.4}Co_{0.8}Fe_{0.2}O_{3-\delta}$ (LSCF) possesses good ionic and electronic conductivity at 500 °C and remains phase stable at elevated temperatures for long periods.[127] The ionic conductivity can be tuned by the Sr dopant concentration by creating oxygen vacancies, while Fe and Co on the B-site largely influence the electrical conductivity governed by small polaron hopping. LSCF has been evaluated in bulk form and appears to be the most stable contender for an oxide cathode.

$Ba_{0.5}Sr_{0.5}Co_{0.8}Fe_{0.2}O_{3-\delta}$ (BSCF) integrated as a SOFC cathode has been shown to exhibit high power density of 400 mW/cm^2 at 500 °C using a ceria based electrolyte and oxide anode.[128] BSCF is based on A-site substitution of Ba^{2+} into $SrCo_{0.8}Fe_{0.2}O_{3-\delta}$. The advantages of this substitution include phase stability (BSCF does not order into a brown-millerite phase) a higher oxygen vacancy concentration, and suitable electronic conductivity.[128, 129] Though this new material system has received much attention in bulk form, the phase appears to be kinetically unstable (decomposition of the cubic phase) at elevated temperatures (700-900 °C) for extended periods of time.[130, 131] Further, reports of thin film BSCF conductivity are limited and there has been no report of integration with thin film SOFCs.

Experimental challenges in fabricating thin film SOFCs that integrate these advanced cathode materials include synthesis of dense single phase nanostructured oxide films that possess mechanical integrity as free standing membranes and good electrical transport properties. In this chapter, we report the high temperature electrical conduction properties of dense nanocrystalline

LSCF and BSCF thin films synthesized by radio frequency sputtering. Additionally, we demonstrate the fabrication of free standing thin film SOFCs incorporating dense nanocrystalline oxide cathodes.

4.2 Experimental methods

LSCF and BSCF thin films were grown by radio frequency (RF) sputtering from a stoichiometric target in 0.65 Pa of Ar at a substrate temperature of 550 °C. Care was taken to grow the films without loss of integrity in the precursor sputter target. X-ray reflectivity (XRR) was used to determine the thickness and growth rate of the films. A detailed study on the effect of deposition temperature and rate on film stress for LSCF and implications for membrane stability is reported in J. Power Sources 195, 5185 (2010). For LSCF films grown at a target power of 20 W, the growth rate was 0.3 nm/min. BSCF films were grown at 90 W and yielded a growth rate of 1 nm/min. Glancing incidence angle X-ray diffraction (XRD) was performed using Bruker D8 Discover instrument. Scans were taken at an incidence angle of 1 ° in omega, using a step size of 0.02 °/s with a CuKα source at 40 kV and 40 mA. Internal stress in the films was determined by measuring wafer curvature changes (Toho FLX-2320-S) and using Stoney's equation,[75] $\sigma_0 = \frac{E_s}{1-\nu_s}\frac{\Delta K}{6}\frac{h_s^2}{h_f}$ where $\frac{E_s}{1-\nu_s}$, ΔK, h_s, h_f, are the substrate biaxial modulus, change in curvature, substrate thickness, and film thickness, respectively. Surface morphology of LSCF thin films was investigated by Carl Zeiss Ultra 55 field emission scanning electron microscopy (SEM). Plane view transmission electron microscope (TEM) samples were prepared by manual polishing followed by ion milling to electron transparency using a Fischione 10-10 dual-beam ion mill. A JEOL 2100 TEM was used to investigate the structure and grain size of the BSCF films. 220-nm-thick Pt strips for conductivity measurements were deposited at a power of 250 W through a shadow mask by direct current sputtering without substrate heating at an Ar pressure of 0.5 Pa. The Pt strips served as contact pads for micromanipulator probes with Pt-plated tungsten tips. The separation between Pt strips was 2.8

mm. In-plane current was measured over a voltage sweep from −10 to 10 mV. Linear regression of the current–voltage plots, which yields film resistance, was used to calculate in-plane conductivity of the films in air from room temperature up to 500 °C at a heating and cooling rate of 2 °C/min. Annealing was carried out in ambient conditions in a Thermolyne 21100 tube furnace with ramping and cooling rates of 5 °C/min. SOFC devices incorporating oxide cathodes were fabricated by patterning Si_3N_4coated Si wafers using photolithography. The patterned wafers were then selectively wet etched in a KOH solution to reveal a free standing Si_3N_4 structure. The electrolyte (YDZ) and cathode were grown on this structure prior to final removal of the Si_3N_4 and deposition of the Pt anode. YDZ was grown sequentially prior to the cathode deposition by RF sputtering at a power of 100 W from a stoichiometric target in 0.51 Pa Ar at substrate temperature of 550 °C. Porous Pt was deposited at a power of 250 W without substrate heating at a pressure of 10 Pa. SOFC testing was performed in a two chamber test station using a mixture of 97% fuel and 3% H_2O and air as the oxidant. Fuel was fed at a rate of 150 ml/min and comprised of Ar carrier gas with 5% H_2.

4.3 Material system: $La_{0.6}Sr_{0.4}Co_{0.8}Fe_{0.2}O_3$

LSCF films grown at room temperature were annealed in air at various temperatures for two hours to determine the temperature at which crystallization, and an accompanying lattice contraction, occurs. Figure 1 shows glancing incidence XRD results of LSCF films grown on YDZ, akin to the SOFC devices discussed in Section 4.3.2, after various heat treatments. As shown, above 450 °C, crystallinity is exhibited and the rhombohedral (R-3c) phase of LSCF (indexed to ICDD 048-0124) appears. While the origin of distortion from the cubic system is not clear, it may be due to oxygen deficiency or slight deviations in exact cation stoichiometry. In order to avoid the large lattice changes associated with crystallization that could have mechanical stability implications, all subsequent films discussed in this chapter were grown at 550 °C.

Figure 4- 1: XRD of LSCF/YDZ films

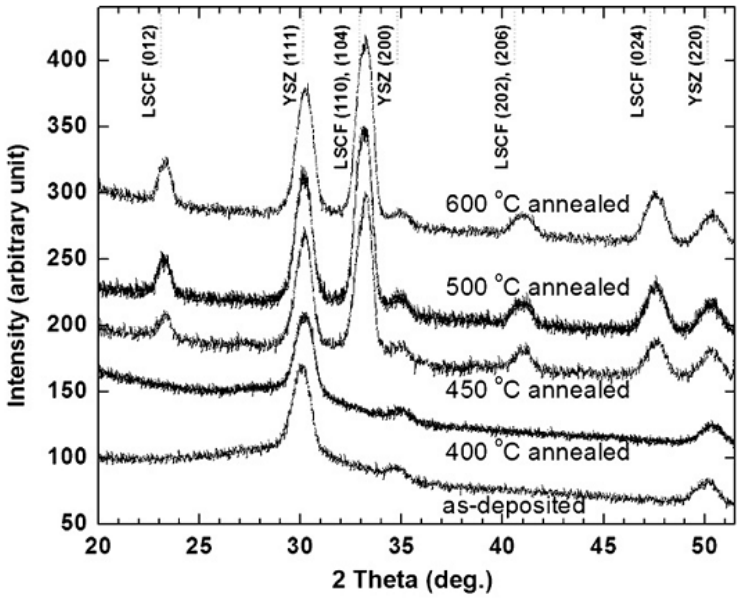

XRD results of several LSCF films grown without substrate heating and subsequently annealed for two hours in air. The formation of crystalline LSCF appears to begin around 450 °C.

Figure 2a shows a planar SEM image depicting the granular microstructure of LSCF films grown at 550 °C and Figure 2b depicts a cross-sectional TEM image of a representative LSCF/YDZ interface. The samples in Figure 1 were also imaged by SEM. Annealing appears to increase the average grain size slightly but no macroscopic cracks are observed, which is promising for mechanical resilience and stability of membranes integrating LSCF. No detectable interfacial layers or macroscopic defects are visible in the TEM image.

Figure 4- 2: LSCF film microstructure

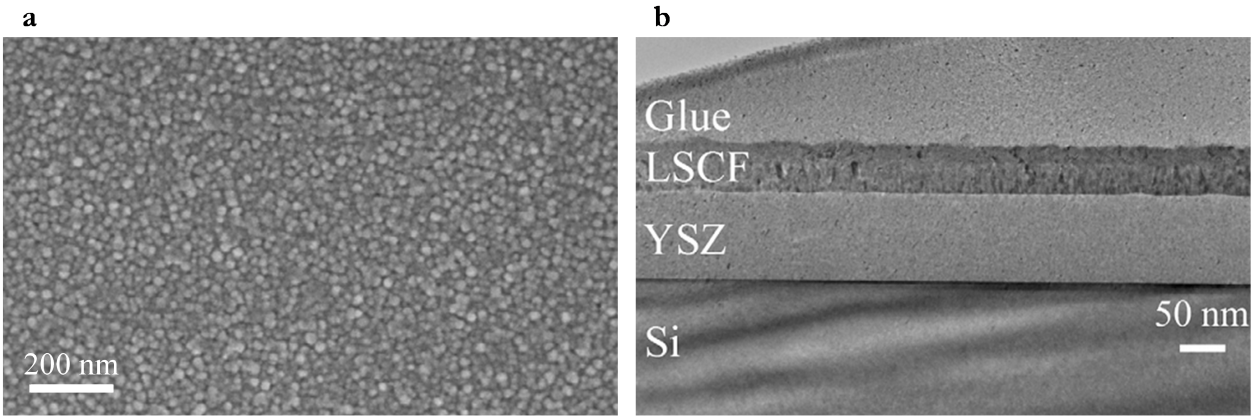

(a) *A SEM image of the surface of a LSCF film grown on YDZ/Si_3N_4/Si and* ***(b)*** *a representative TEM image of the cross section of such a bilayer heterostructure.*

As discussed in Chapter 2, in order to fabricate stable, free standing membranes it is important that the components remain in regimes of compressive residual stress. For YDZ on Si_3N_4 coated Si, the thermomechanical stress (σ_{TM}) is on the order of several hundred MPa. This can be countered with high compressive residual stresses. For metal electrodes, the differences in thermal expansion coefficients (TEC) between electrolyte and electrodes are of little importance since the metals are porous and ductile. However, in the case of oxide electrodes it should be considered. TEC coefficients are typically a function of temperature. As a rough estimate of the additional σ_{TM} generated between the mismatch of YDZ and LSCF, the values at 500 °C are used. LSCF is reported to have a TEC of approximately 20 ppm/K,[132] while YDZ is approximately 10 ppm/K.[48] As such, σ_{TM} of nearly a GPa is expected. The measured biaxial stress as a function of temperature of a bilayer LSCF/YDZ sample is shown in Figure 3. The combined residual stress of approximately –500 MPa at 500 °C implies that the intrinsic film stress is large enough to counteract σ_{TM} at SOFC operating temperatures and place the membrane in a safe compressive stress regime. As shown in Figure 3, the LSCF/YDZ membrane is initially flat due to a nearly neutral stress state. The

incorporation of oxygen into LSCF likely causes a slight lattice contraction by exerting an increased electrostatic attraction amongst its neighboring cations. In other words, by introducing oxygen into the lattice, the oxidation state of the neighboring cations increases and likely reduces the cationic radius, decreasing the unit cell volume. This is macroscopically manifested in an increase in biaxial compression. For membrane stability, the controlling stress states are imperative to ensure rupture does not occur. While we have not measured subsequent thermal cycles, these results indicated that fabrication of an oxide heterostructure membrane that operates at elevated temperature is certainly possible.

Figure 4- 3: Intrinsic stress of LSCF/YDZ

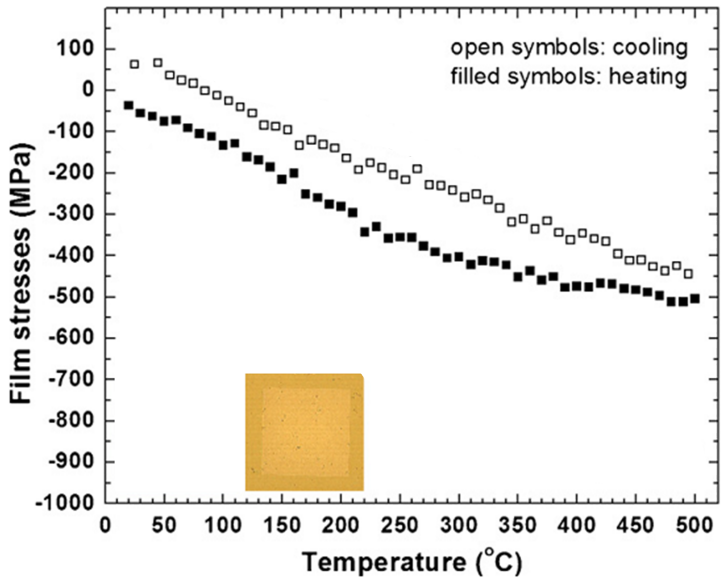

The evolution of biaxial stress in a LSCF/YDZ film on Si_3N_4/Si as a function of temperature. The inset shows a corresponding membrane 160 um in side length released from the underlying support. Note that there is no buckling as expected due to the stress state initially measured.

4.3.1 Electrical conductivity

In addition to having an oxide material that possess some catalytic activity and can be fabricated in membrane form by control of intrinsic stress states, the electrical conductivity is of importance for drawing power from the SOFC. Figure 4 shows the temperature dependent conductivity in air of a 63 nm thick LSCF film, which is above the critical thickness (~10-20 nm) where finite size effects are observed. Electrical conductivity in LSCF is a result of small polaron hopping along Co sites.[127] An expression for electronic conductivity from this mechanism can be given in a similar fashion to ionic conductivity discussed in Chapter 1, namely; $\sigma_e = \frac{A}{T}\exp\left(\frac{-E_a}{kT}\right)$, where A is a material specific constant and E_a is an activation barrier that can be calculated from conductivity data. Although the film is crystalline, the initial electrical conductivity is low at T < 200 °C. This is suspected to be a result of both oxygen deficiency and microstructure. The increase in conductivity above 200 °C on heating is likely associated with increased activity of polaron transport and oxygen uptake. The latter can reduce the number of oxygen vacancies and thus, increase the number of polarons leading to an electrical conductivity increase with temperature.[133] This is confirmed in the cooling trace shown in Figure 4a as the conductivity is an order of magnitude higher than on heating.

Figure 4- 4: Electrical conductivity

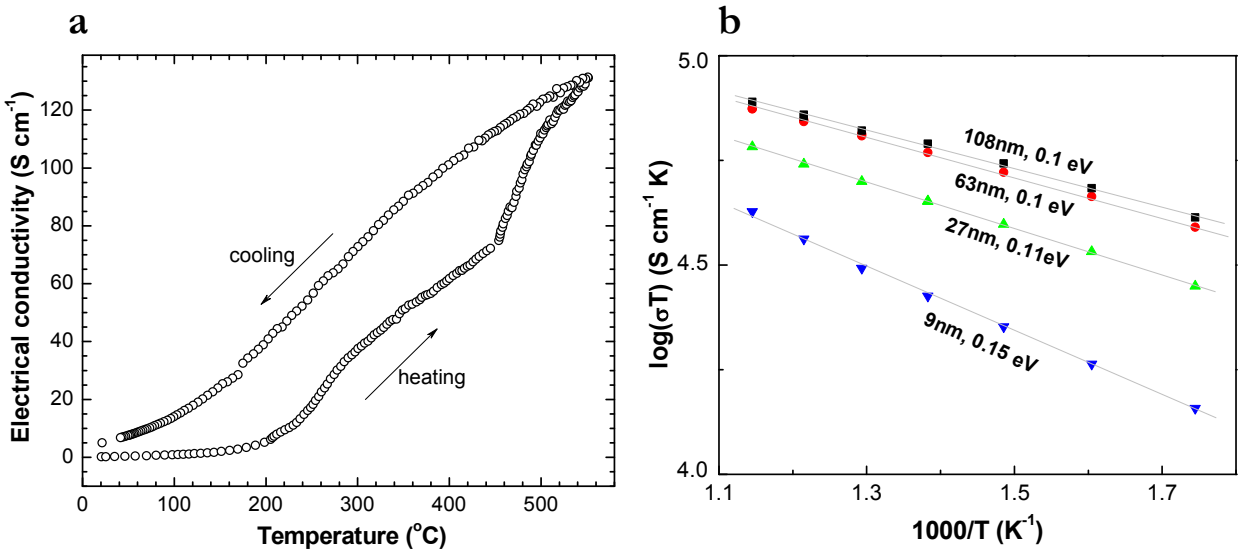

(a) *A representative scan of the electrical conductivity of a 63 nm thick LSCF film and* ***(b)*** *finite size effects of LSCF thin films.*

The LSCF film only reached σ_e~130 S/cm at 500 °C, which is about half the value of bulk at comparable temperatures.[134] E_a was calculated in the 550−200 °C range during cooling, with the results for varying thickness shown in Figure 4b. In the large thickness limit, E_a is in agreement with a bulk values in the 0.08-0.11 eV range.[135] In comparison to previous studies on the conductivity of LSCF films grown at room temperature having larger average grain size, the conductivity is slightly lower,[136, 137] however, in this material system it has been shown that the conductivity in crack-free LSCF thin films is proportional to grain size.[137] Finite size effects for electrical conductivity of metals have been well described by Fuchs[138] and Sondheimer[139]. If electron collisions at film interfaces (substrate-film and film-air) are non-specular, the conductivity will decrease with thickness. This effect becomes more important when the mean free path of the carriers is on the order of the film thickness. In our observations, the oxide grain size (10-20 nm range) appears to set the critical thickness at which the electrical conductivity reduces quickly with an accompanying increase in

hopping activation energy, likely due to incoherent scattering at disordered grain boundaries. This implies that the apparent mean free path of electrons is approximately on the order of the average grain size.

4.3.2 Fuel cell synthesis

A cross-sectional schematic of the steps towards making a fuel cell device integrating a free standing LSCF|YDZ|Pt structure is shown in Figure 5.

Figure 4- 5: Schematic of SOFC integrating LSCF

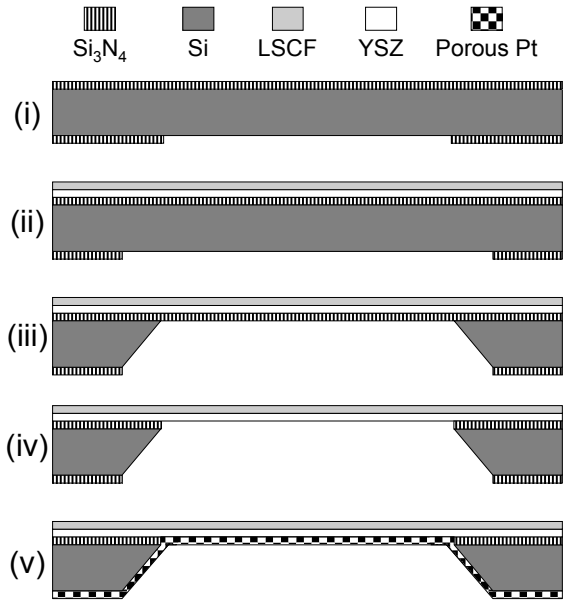

The processing procedure used to make LSCF|YDZ|Pt fuel cell devices. The steps correspond to (i) photolithographic patterning, (ii) deposition of oxide films, (iii) removal of the bulk Si substrate, (iv) removal of the Si_3N_4 support creating a free standing oxide heterostructure, and finally (v) deposition of nanoporous Pt for the anode.

The tri-layer freestanding membrane structures were stable at room temperature and elevated temperatures where measurements were carried out. Figure 6 shows some fuel cell characteristics and Figure 7 depicts representative optical images of a representative LSCF/YDZ/Pt structure during and after SOFC measurement.

Figure 4- 6: SOFC characteristics for LSCF/YDZ/Pt devices

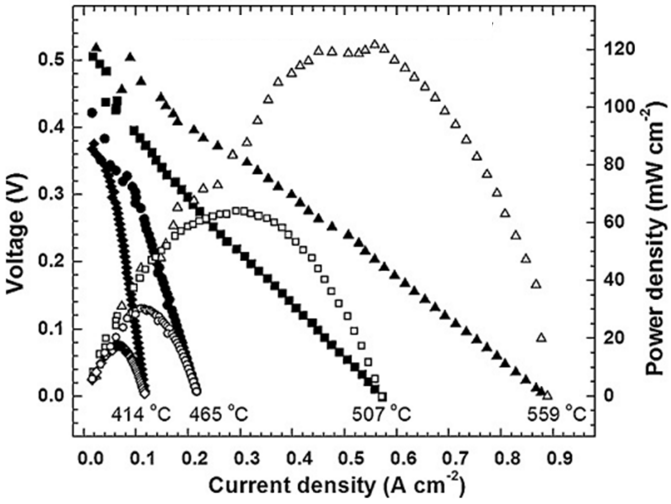

SOFC performance using a 60 nm LSCF|60 nm YDZ|80 nm Pt free standing structure.

Figure 4- 7: LSCF/YDZ/Pt membranes during operation

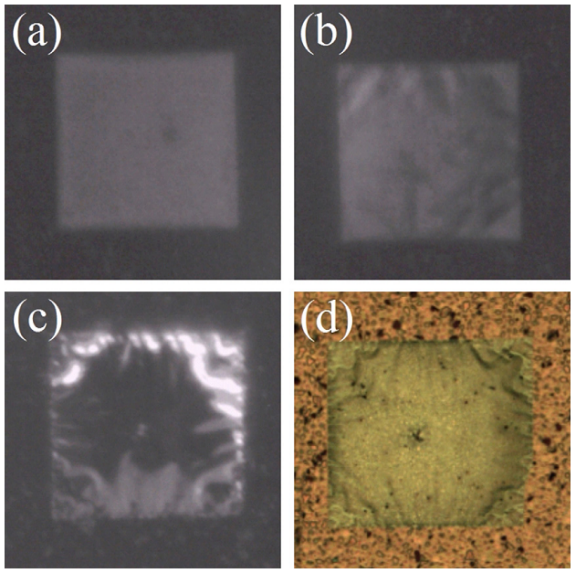

Free standing LSCF|YDZ|Pt structures with 160 μm side length at ***(a)*** *140 °C,* ***(b)*** *150 °C,* ***(c)*** *430 °C, and* ***(d)*** *after testing cooled down to 25 °C.*

The OCV of the fuel cells was ~0.4 V at 400 °C and continued to increase with temperature until the maximum voltage stabilized at ~0.6 V at 560 °C. At this temperature, the maximum power

density observed was 120 mW/cm^2, which is comparable to results in the literature with Pt|YDZ|Pt SOFCs with un-optimized electrodes.[140] However, the OCV is of concern. The ideal value should be ~1 V at elevated temperatures. The voltage can be reduced by fuel crossover via cracks or voids in the structure, though this seems unlikely based on demonstrations of ideal OCV values for Pt|YDZ|Pt SOFCs having 27 nm thick YDZ. As discussed in Chapter 3, leakage currents can also reduce the voltage and it is noted that the YDZ electrolyte is 60 nm. However, the most likely explanation for the deviation from ideality is due to resistive loss in current collection from the cathode and potentially poor electrocatalytic behavior for oxygen reduction in this temperature range. Nevertheless, the integration of a mechanically stable oxide heterostructure is promising for exploring future low temperature oxide electrode materials for SOFCs. Additionally, based on the annealing studies presented in the initial Section, LSCF appears stable at elevated temperature and does not show any interfacial reaction with YDZ.

4.4 Material system: $Ba_{0.5}Sr_{0.5}Co_{0.8}Fe_{0.2}O_3$

Many of the challenges associated with incorporating BSCF into a working thin film SOFC device are similar to those outlined and explored in detail in Section 4.3 for LSCF. Thus, discussion related to oxygen deficiency, cation non-stoichiometry, and finite size effects on electrical conductivity are applicable in this Section and will not be repeated. Glancing incidence XRD of BSCF thin films grown on single crystal (100) YDZ for different film thicknesses is shown in Figure 8. The peaks match well with the cubic (Pm-3m) index (ICDD 055-0563) for BSCF.

Figure 4- 8: XRD of BSCF on sc-YDZ

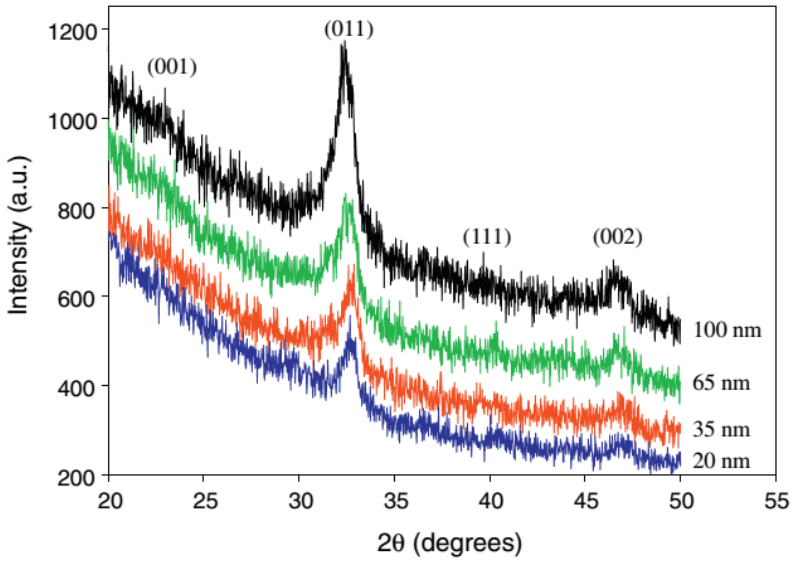

Glancing incidence XRD of BSCF films on (100) YDZ substrates showing increased intensity of reflections with increasing thickness and indexed to ICDD 055-0563.

Plan view TEM images and SAED pattern are shown in Figure 9. Similar to LSCF, a granular microstructure with nanoscale grains on the order of 20-30 nm is observed. The SAED pattern confirms the single phase, polycrystalline cubic nature of the BSCF film.

Figure 4- 9: BSCF film microstructure

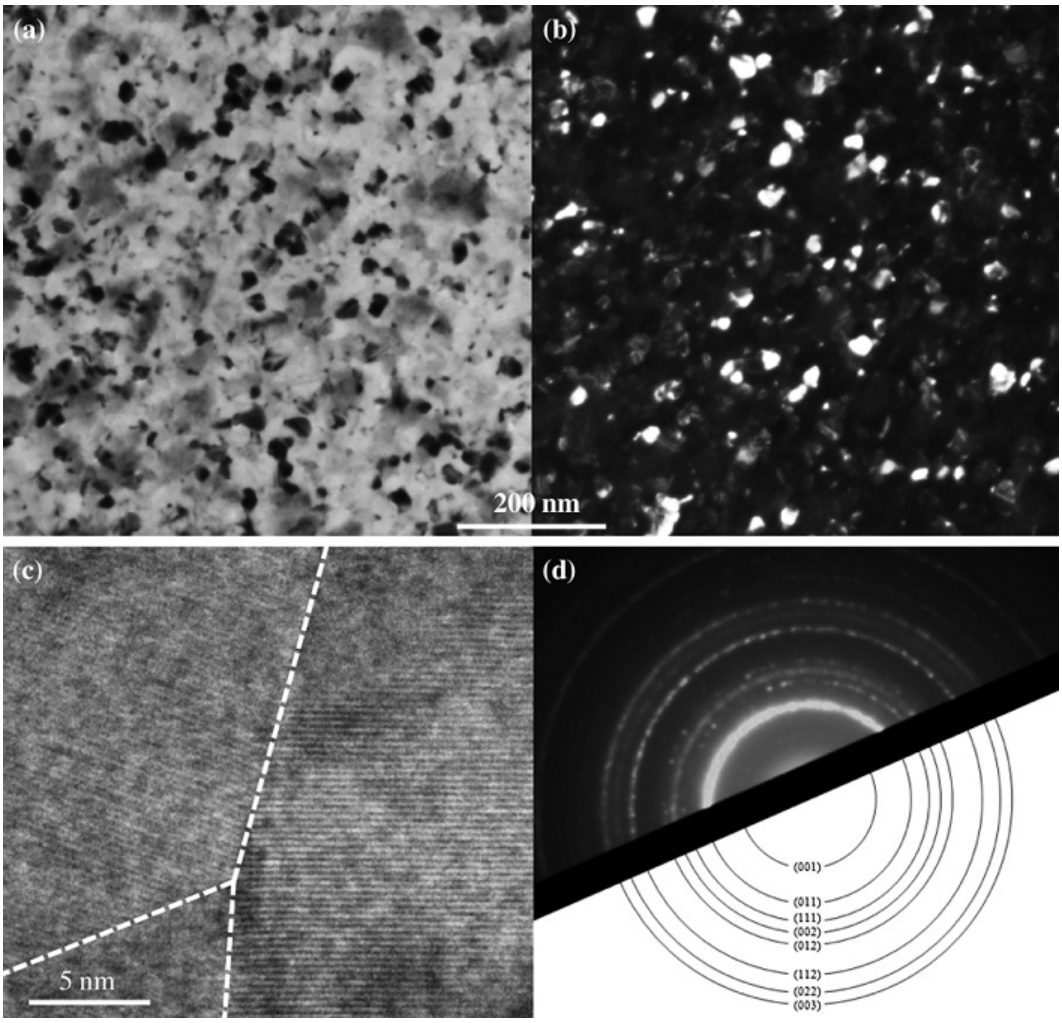

(a) *Bright field TEM image of the granular microstructure of BSCF films;* ***(b)*** *dark field (011) TEM image;* ***(c)*** *high resolution image of a grain boundary triple junction; and* ***(d)*** *a SAED pattern of BSCF indexed to ICDD 055-0563.*

4.4.1 Electrical conductivity

A representative electrical conductivity trace is shown in Figure 10a, while an Arrhenius plot of several BSCF films in the 200-400 °C range is presented in Figure 10b. Similar to LSCF, in this temperature range, small polaron hopping conduction associated with the mixed-valent Co and Fe sites is believed to govern electrical conductivity.[141] The activation energy was extracted from

conductivity data on cooling in the linear 200-400 °C range. In the limit where the BSCF film thickness exceeds the grain size, the activation energy for electron conduction is 0.23 eV, which compares well to a reported value of 0.254 eV for epitaxial BSCF thin films.[142] The value of electrical conductivity is approximately constant for thicknesses above 20 nm and is similar in value to LSCF, indicating adequate electronic conduction for potential SOFC usage. Finite size effects are seen at thicknesses near or below the grain size, likely originating from a similar physical scattering mechanism discussed for LSCF in Section 4.3.1.

Figure 4- 10: Conductivity of BSCF films

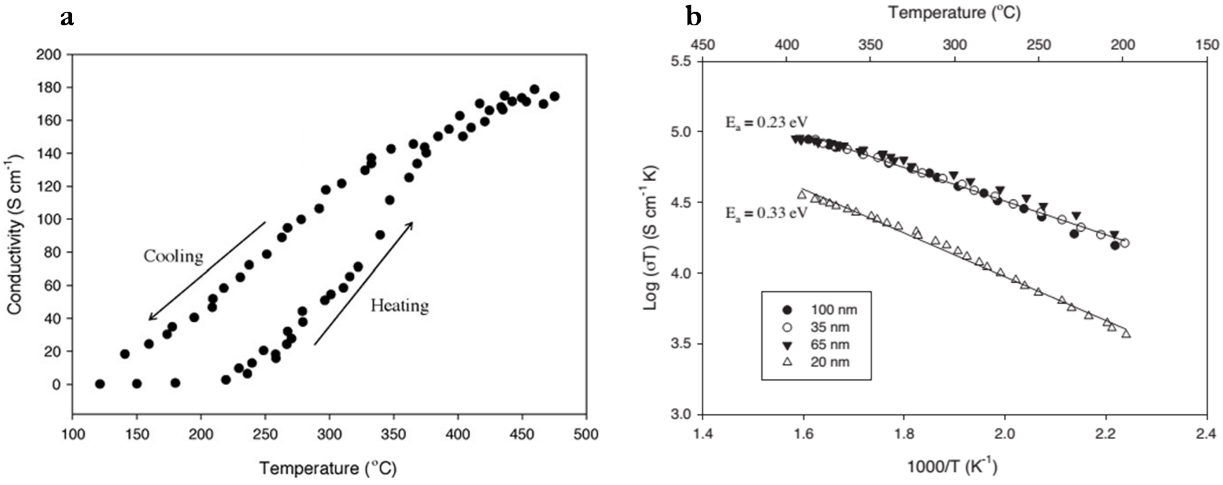

***(a)** A typical conductivity trace of a 65 nm thick BSCF film and **(b)** an Arrhenius plot showing the stark difference in activation barriers for films with thicknesses below the average grain size.*

4.4.2 Fuel cell fabrication

Thin film SOFCs were made using porous Pt as the anode, 100 nm YDZ as the electrolyte, and dense BSCF as the cathode, similar to the schematic in Figure 5. SOFCs with 35, 50, and 100 nm thick BSCF cathodes were fabricated and tested. The maximum power density of such cells decreased monotonically with decreasing cathode thickness. This behavior is believed to be related to a parasitic interfacial reaction with YDZ since the planar surface area of the dense BSCF cathodes

was equivalent. As the thickness is reduced, the reaction product accounts for a larger fraction of the cathode material and subsequently reduces the SOFC performance. An Arrhenius plot of the maximum power density of the best performing SOFCs with 100 nm BSCF as a function of temperature is plotted in Figure 11a. While power density is a convolution of many factors, it fits well to a single activation energy over several orders of magnitude. Using a linear fit to the data, the overall activation energy of the maximum power density for the SOFCs was estimated to be 1.44 eV. Ionic transport through YDZ electrolytes generally occurs with an activation barrier of ~ 1 eV and Pt|YDZ|Pt fuel cells exhibit activation energy of ~ 1 eV.[89, 143] The kinetics of oxygen reduction on the surface of BSCF has been observed to occur with an activation energy in the 1.4–1.7 eV range.[144] Therefore, it is reasonable to infer that thin film BSCF cathodes dominate the overall performance attributes and act as the main limiting mechanism.

Figure 4- 11: Maximum power density of SOFCs with BSCF cathodes

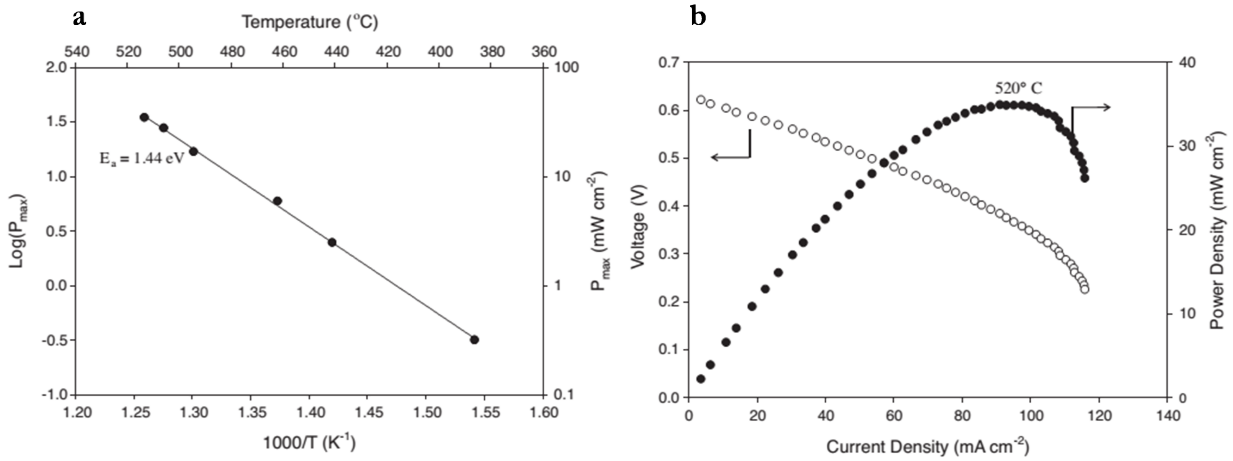

(a) *An Arrhenius plot of the maximum power density for a 100 nm BSCF/100 nm YDZ/80 nm Pt SOFC showing an activation barrier that corresponds to the oxygen reduction reaction on BSCF and* ***(b)*** *an example I-V, I-P curve of the SOFC at the maximum power condition.*

The current–voltage characteristics at the maximum power density for a representative SOFC with a 100 nm thick BSCF cathode is shown in Figure 11b. A maximum power density of 35

mW/cm^2 was achieved at 520 °C. BSCF has been touted as a high performance cathode material;[128] though this performance is lower than LSCF cells tested under similar conditions and we observe characteristics of BSCF that are not ideal. The Nernst potential under measurement conditions at 520 °C should be 1.08 V, however an OCV of 0.63 V was observed, similar to that of LSCF. In light of previously discussed Pt|YDZ|Pt SOFCs exhibiting near ideal OCVs with electrolytes as thin as 27 nm and knowing BSCF reaction kinetics are dominating the performance; it is likely that the OCV deviation is due to poor catalytic activity towards oxygen reduction at these temperatures. The main goal in implementing an oxide cathode such as BSCF is long term stability. XRD results after annealing of the BSCF (100 nm)/YDZ (100 nm) bilayer system at 600 °C, shown in Figure 12, indicates some aspect of instability. All peaks appear to shift to higher values of 2θ after annealing, consistent with a decrease in lattice parameter likely due to oxygen incorporation for initially non-ideal anion stoichiometry. The (012) BSCF orientation appears to be annealed away, possibly due to atomic rearrangement towards a more favorable preferred orientation such as (011). An unidentifiable peak emerges at 2θ~37 °C after only two hours at 600 °C and persists with increasing annealing time. Reaction products of BSCF with YDZ and structural meta-stability of the cubic phase of BSCF have been observed after extended high temperature annealing conditions;[130, 145] yet there have been no investigations into stability in the sub-700 °C regime, especially in such ultra-thin films. Thus, it appears that BSCF may not be compatible with YDZ without a barrier layer such as GDC and additional work on the kinetic stability of this material is required.

Figure 4- 12: XRD of BSCF/YDZ after isothermal annealing

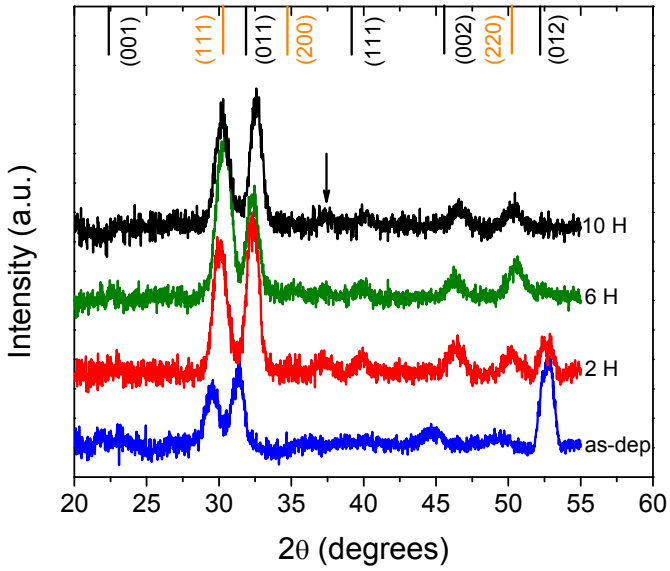

XRD of BSCF (100 nm)/YDZ (100 nm) showing the emergence of an unidentified phase after being annealed at 600 °C for various amounts of time showing the emergence of an unidentified phase around 37° (indicated by arrow). The orange and black lines correspond to ICDD tabulated positions for YDZ and BSCF, respectively.

4.5 Conclusion

In summary, this chapter has shown how the model YDZ membrane system was used to integrate and test advanced oxide electrodes, namely LSCF and BSCF. While both electrodes cannot compete with the high performance shown using Pt, the challenges of integrating free standing oxide heterostructures opens the door for future materials. LSCF shows promise for future development, though it requires additional low temperature catalytic activity. BSCF possibly suffers from a parasitic reaction with YDZ even at low temperatures.

5 NOVEL ELECTROLYTE SYNTHESIS

5.1 Introduction

When the mobile ionic species in SOFCs is oxygen (O^{2-}), ionic conductors capable of sufficiently fast transport generally require elevated temperature (800-1000 °C).[87] The operation temperature must be reduced significantly in order to improve material stability, reduce start-up time, and extend the applications of SOFCs to mobile power units. High performance of SOFCs at reduced temperatures can be achieved by minimizing total loss across the entire cell. Kinetic losses at the anode and cathode make up two of the three main losses. The third loss is associated with O^{2-} ion transport in the electrolyte, which is Ohmic in nature. It can be counteracted by designing electrolyte materials with increased ionic conductivity at low temperature or reducing electrolyte thickness as low as physically possible without significant electronic leakage. For these reasons, free standing thin film solid oxide fuel cells using nanocrystalline $(Y_2O_3)_y(ZrO_2)_{(1-y)}$ electrolyte membranes with Pt electrodes have been recently explored.[37, 38] High performance has been achieved with optimized electrodes and corrugated electrolyte structures.[61, 83] Enhanced kinetics of the oxygen reduction reaction (ORR) and improved TF-SOFC performance at low temperature can be realized by using a Gd doped CeO_2 (GDC) interlayer on the cathode.[109] Additionally, SOFC performance enhancements and faster rates of the ORR have been reported for yttria-doped ceria.[88, 118] $(Gd_2O_3)_{(z)}(CeO_2)_{(1-z)}$ is well known for its superior ionic conductivity at low temperature.[11, 16] Further, CeO_2 has been shown to be an active electrocatalyst for hydrocarbon oxidation.[146]

Chapter 2 outlined the mechanics of YDZ membranes; however, GDC differs from YDZ in that Ce is a mixed valent cation. This aspect has significant electrochemical and mechanical consequences. For example, the elastic modulus (E_m) of GDC is p_{O_2} dependent whereas that of YDZ is not.[58] The stability of free standing GDC membranes in an ambient atmosphere has been

studied previously and it was found that the association/dissociation reaction, $Gd'_{Ce} + V_O^{\cdot\cdot} \Leftrightarrow [Gd'_{Ce}V_O^{\cdot\cdot}]^{\cdot}$, plays a strong role in volumetric deformations at low temperatures (T < 200 °C).[147] Above 250 °C, researchers find that the film does not exhibit anomalous elastic properties.[147] Thus, if a stable free standing GDC membrane is demonstrated at low temperatures and there is adequate residual film stress to counter the thermally generated stress, stable electrolyte membranes for SOFC applications could emerge. In addition to temperature dependent stability, creating a working, high performance SOFC with a free standing electrolyte membrane requires mechanical stability across an oxygen partial pressure gradient. As mentioned, the environmentally dependent E_m for GDC has been attributed to the formation of Ce^{3+} at low p_{O_2}, which leads to an increase in the average bond length altering the elastic modulus.[59] This complex interplay between chemical and mechanical properties makes utilizing free standing GDC membranes for low temperature thin film SOFCs rather challenging. These aspects have limited the choice of materials for research and development in the exploration of physical electrolyte thickness reduction.

In this chapter, we demonstrate two methodologies made possible by physical vapor deposition processes used to integrate GDC into robust membrane structures. Low temperature synthesis of oxide alloys of mixtures of $[(Y_2O_3)_{0.08}(ZrO_2)_{0.92}]_x[(Gd_2O_3)_{0.1}(CeO_2)_{0.9}]_{(1-x)}$ ($YDZ_xGDC_{(1-x)}$), where x represents the volume fraction of each component is demonstrated. Above a critical volume fraction of GDC, these membranes are chemically and mechanically stable during SOFC operation. Traditional processing of similar composite materials requires temperatures of over 1300 °C to achieve solid solution mixtures.[148, 149] Moreover, formation of defects at YDZ-GDC interfaces during high temperature sintering has been reported.[150] The method of co-sputtering addresses these significant issues and has the potential to create nanostructured materials with a controllable ratio of constituents at reduced processing temperatures. To demonstrate compositional control, we explore

co-sputtering with tunable target power grading to achieve nanoscale functionally graded materials. While YDZ and GDC were chosen as the two parent material systems for this study, the methodology presented is widely applicable. We demonstrate mechanically robust, chemically stable, free standing, oxide alloy and compositionally graded thin film electrolyte membranes for SOFC applications. Structural and chemical characterization of the novel electrolytes is presented. Furthermore, high performance SOFCs functioning with hydrogen and methane fuel are shown.

5.2 Experimental methods

Oxide alloy and compositionally graded films were grown by radio frequency sputtering in an AJA Orion system from oxide targets of $(Gd_2O_3)_{0.1}(CeO_2)_{0.9}$ and $(Y_2O_3)_{0.08}(ZrO_2)_{0.92}$ at 550 °C in 0.51 Pa Ar. Oxide alloy samples were also grown without substrate heating. The substrates were rotated during deposition to ensure uniform film coverage and prevent lateral compositional gradients. Growth rate was estimated by using X-ray reflectivity (XRR) for several samples and linearly extrapolated as a function of target power. For oxide alloy films, the target power was kept constant during deposition, creating a homogeneous mixture of both phases. In the compositionally graded films, power to each respective target was ramped such that the appropriate volume fraction of each film would be deposited. The minimum volume fraction of each component corresponds to the lowest power that could sustain stable plasma during growth. Glancing incident X-ray diffraction (XRD) and XRR was carried out on a Bruker D8 diffractometer. Since glancing incident techniques may be biased towards surface regions of the film, values of 0.5, 1, 1.5, and 2° in Ω were tested. No difference in peak positions was observed and all XRD patterns shown in this chapter were taken at Ω = 1 °. Cross-sectional transmission electron micrographs were taken using a JEOL 2100. Samples were prepared by manual lapping and subsequent ion milling to electron transparency using a Fichione 10-10 ion mill. X-ray photoemission spectroscopy (XPS) was done on compositionally

graded films using an Esca SSX-100 spectrometer at a scan rate of 0.02 eV $step^{-1}$. Film surface milling was done with energized Ar ions and spectral areas for Zr d lines and Ce d lines were estimated by peak fitting and integration in CasaXPS as a function of milling time. Based on the fact that nearly complete sputtering of the film took approximately 105 minutes, the average rate was approximately 0.81 nm min^{-1}. Conductivity of oxide alloy films grown at 550 °C was measured using a direct current (DC) method with sputtered Pt electrodes in air as a function of temperature every 2 ° up to 550 °C at a heating rate of 2 °C/min. Si platforms for thin film SOFCs were made using a micro-fabrication process of photolithography, dry etching and wet etching. Pt and Ru electrodes for the SOFCs were deposited by direct current sputtering at 11.3 and 10 Pa without substrate heating, respectively. Fuels used in this study were either pure CH_4 or an Ar carrier gas with 5% H_2. Fuel cell measurements were carried out on a custom built test station using standing laboratory air as the oxidant and fuel saturated with 3% H_2O.

5.3 Oxide alloy membrane, YDZ-GDC

Figure 1 shows the XRD patterns of GDC, $YDZ_{0.2}GDC_{0.8}$, $YDZ_{0.5}GDC_{0.5}$, $YDZ_{0.8}GDC_{0.2}$, and YDZ films grown at 550 °C. The XRD pattern shows the existence of a cubic fluorite crystal structure with varying lattice parameter between that of YDZ and GDC. Similar results were obtained for composites grown without substrate heating, indicating a substantial decrease in processing temperature for such materials. For x = 0.5, the (111) d-spacing can be estimated as 0.305 nm from Vegard's law.[151] This agrees well with the experimentally measured value of 0.30 nm. Similar trends were found for (200) and (220) spacing; the measured and estimated values are plotted in Figure 2.

Figure 5- 1: XRD of oxide alloy films

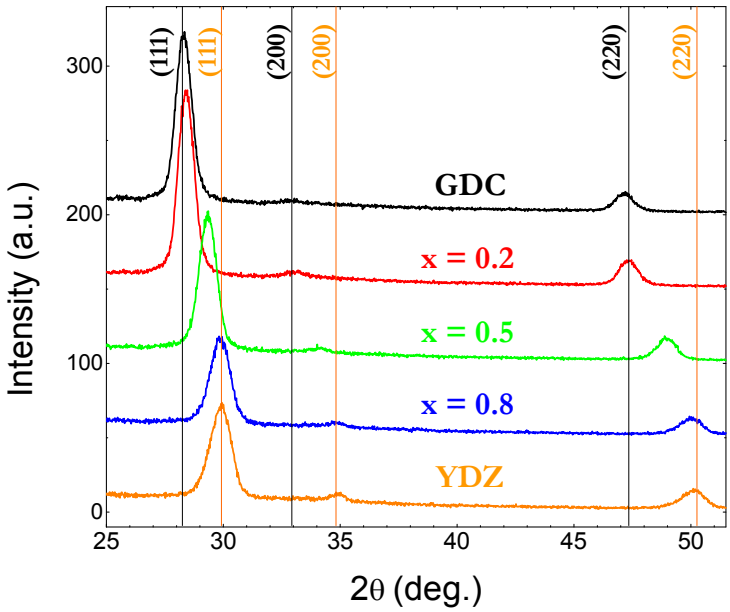

XRD of the oxide alloy series, showing solid solution characteristics. YDZ and GDC are indexed to ICDD 030-1468 and 01-075-0161, respectively.

Figure 5- 2: Lattice parameters of YDZ-GDC alloys

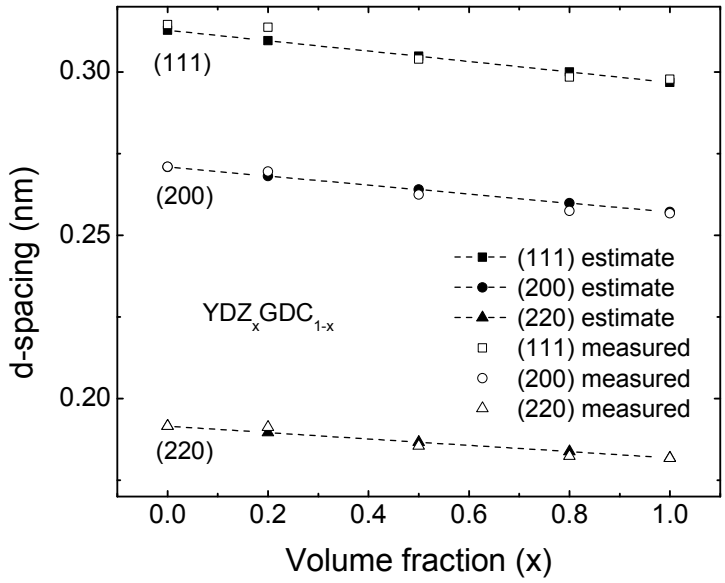

Plot of the d-spacing as a function of composition for YDZ_xGDC_{1-x}, confirming Vegardian behavior.

Figure 3a-b shows a selected area diffraction (SAED) pattern of the x = 0.5 film. Ring patterns confirm the polycrystalline nature observed by XRD. Since the area of investigation is profoundly smaller than that of XRD, average lattice spacing from several spatially separated SAED patterns were necessary to determine an accurate estimate of the various d-spacing in the film. The innermost rings correspond to the smallest reciprocal space length and hence the largest real d-spacing, which in this case should be (111). Based on the results of XRD, a single ring with spacing of approximately 0.305 nm is expected. The measured spacing of 0.31 nm corresponds reasonably well within a single standard deviation of the averaged measurements. The (200) spacing was measured to be 0.26 nm which corresponds to the estimated value of 0.264 nm from Vegard's law. Similarly, (220) spacing was found to be 0.19 nm corresponding well to 0.187 nm from Vegard's law. Figure 3c-d shows bright field and high resolution TEM plan view images of the x = 0.5 film. It can be seen that the alloy exhibits a similar microstructure to pure YDZ films described in Chapter 3 and has an average grain size is on the order of 20 nm. Based on these results, solid solution of YDZ and GDC seems likely in these films.

Figure 5- 3: TEM characterization of YDZ-GDC alloy

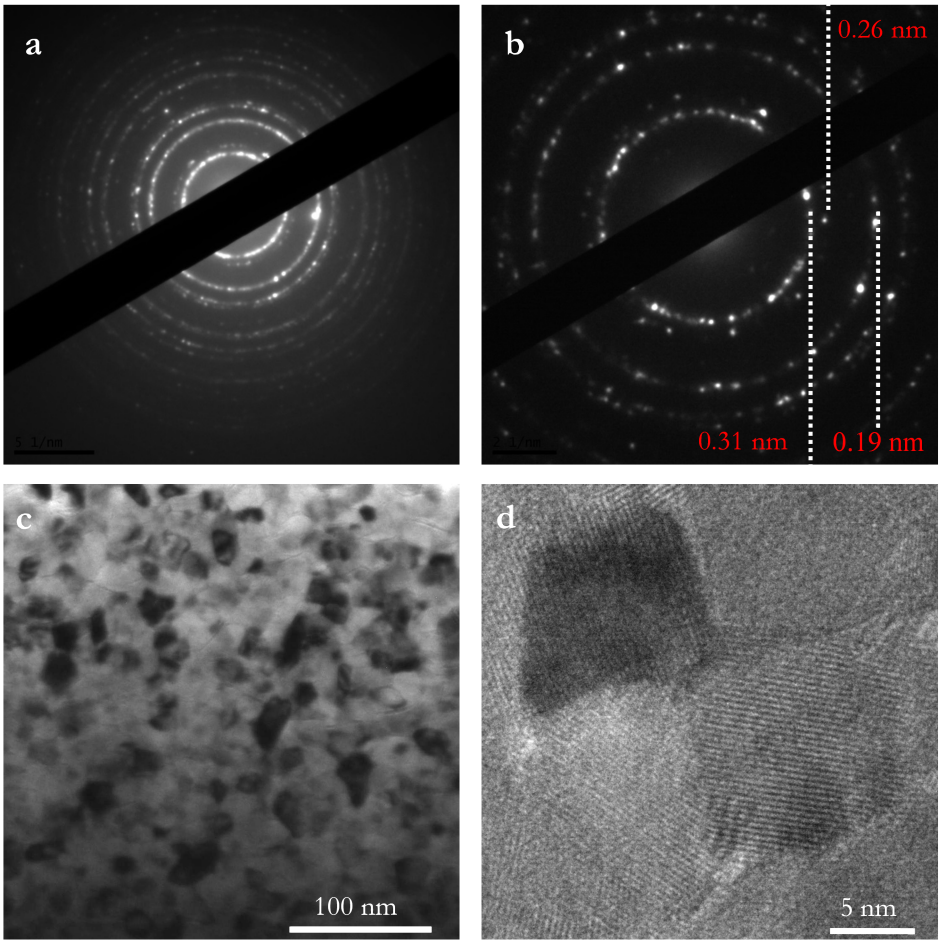

(a) *SAED pattern of a* $YDZ_{0.5}GDC_{0.5}$ *alloy sample with* ***(b)*** *inner most lattice spacing marked.* ***(c)*** *bright field plane view TEM image of the granular microstructure and* ***(d)*** *high resolution TEM lattice image of several grains.*

5.3.1 Electrical properties

Figure 4 shows the total conductivity of the oxide alloy film electrolytes grown at 550 °C on Si_3N_4 coated Si measured in air. Under the oxygen partial pressure conditions of air, both YDZ and GDC are known to be in the ionic conduction regime (i.e. $t_i \sim 1$),[152] however, without blocking electrodes or AC impedance measurements, these results represent the total conductivity of the films.

Figure 5- 4: YDZ-GDC alloy conductivity

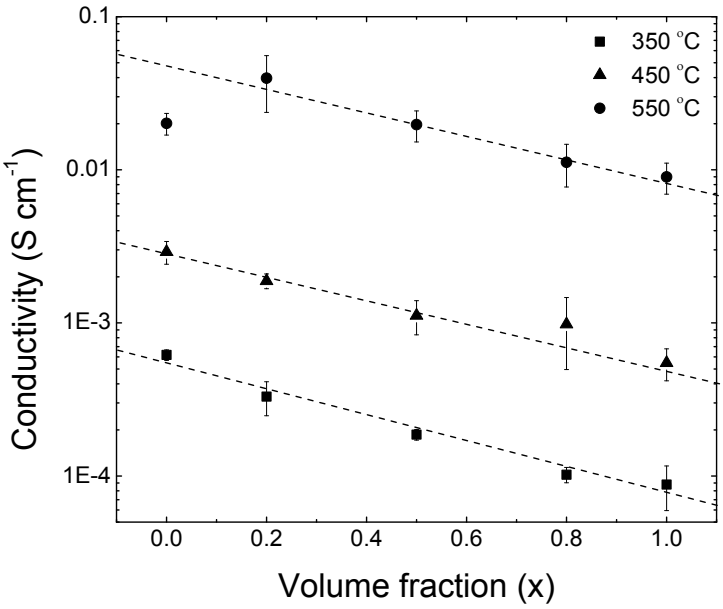

The total conductivity of oxide alloy films measured as a function of composition at 350, 450, and 550 °C. The dashed lines are meant to serve as guides to the eye.

Similar to the thermally activated hopping mechanism discussed in the Section 1.2.1 and 4.3.1, the results in this study can be compared with the activation energy for YDZ and GDC bulk materials reported in the literature. E_a was calculated in the 250 – 550 °C range for all compositions. The estimated value of 1.05 eV for pure YDZ (x = 1) is in agreement with values reported across the literature.[11, 16] A conductivity value of 0.009 S/cm at 550 °C is in the 10^{-1} – 10^{-3} S/cm range reported at 550 °C for thin film YDZ.[89] The large scatter in conductivity values in the literature is hypothesized to be related to film stress. In the case of pure GDC (x = 0), E_a was estimated to be 0.84 eV similar to reports on the grain boundary activation barrier for transport in nanocrystalline GDC thin films.[52] This finding coupled with conductivity of 0.02 S/cm at 550 °C, which is approximately an order of magnitude lower than bulk values, indicates grain boundary dominated transport.[52, 153] This observation is not unreasonable considering the nanostructured polycrystalline

nature of the films depicted in Figure 3. The activation energy for conduction in the solid solution mixtures of YDZ-GDC range from 1.1 to 1.3 eV and decrease monotonically as the fraction of GDC is decreased excluding the pure YDZ and GDC endpoints and match well with bulk reports in the literature.[154] However, bulk solid solution of these phases has been reported to show lower total conductivity than that of each constituent;[154] while we observe a quasi-tunable conductivity across the range of compositions tested in this study.

5.2.1 Oxide alloy membrane stability

The mechanical stability of free standing membranes was evaluated with 100 nm electrolytes grown on micro machined Si_3N_4 coated Si substrates as described in the experimental section. As described in the introduction, low temperature elastic anomalies arising from defect ordering play a role in the stability of GDC membranes in ambient atmosphere. Films grown at 550 °C were released from the underlying patterned substrate, creating a free standing membrane that is bounded by the original substrate. Optical micrographs in Figure 5 show a representative set of mechanical buckling for membranes immediately after being released at 25 °C. As discussed for homogeneous YDZ membranes in Chapter 2, the material response is due to residual strain in the films. It is manifested by non-linear buckling of the free standing structures.

Figure 5- 5: Buckling of YDZ-GDC alloy membranes

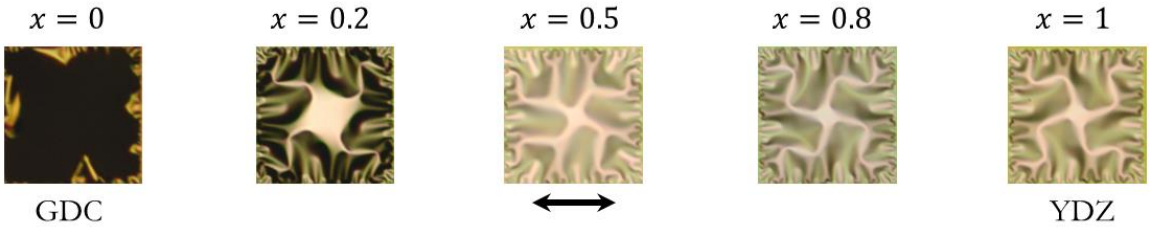

Top view optical micrographs of free standing oxide alloy electrolyte membranes of YDZ_xGDC_{1-x}, showing a failed GDC membrane and expected YDZ pattern at the end points. The scale bar represents 100 μm.

Similar to previous work under congruent boundary conditions, four-fold rotational symmetry in pure YDZ membranes is observed, however, pure GDC membranes fail in all cases. Looking across the composition, there is a distinct shift in macroscopic buckling behavior when crossing the x = 0.5 composition electrolyte. As discussed in Chapter 2, elastic buckling is largely dependent on the residual stress (σ_0) present in the free standing material and aspect ratio $\left(\frac{L}{h}\right)^2$ In this study, the membrane thickness (h) and free standing width (L) were kept constant at 100 nm and 160 μm, respectively. Additionally, the growth rate of each constituent material was maintained at 1 nm/min and the cooling rate equivalent for all films. While σ_0 has not been explicitly measured for GDC films in this thesis, in the context of this study, the only modulation of σ_0 occurs as a material property of $YDZ_xGDC_{(1-x)}$ films as a function of x. Out of plane displacement in the buckling patterns shown in Figure 5 is a clear indication of compressive stress relief and the pattern shown in the case of pure YDZ matches well to expectations based on the simple elastic model presented in Chapter 2. The thermal expansion coefficients of YDZ and GDC are comparable at 550 °C,[48, 155] however, there is a slight difference in the temperature dependence of their expansion coefficients. As shown in Chapter 2 for pure YDZ films grown at different temperatures, σ_{TM} is outweighed by the stress induced during the sputtering process. Therefore, the most likely origins of different σ_0 in these films lies in thermomechanically induced film stress (σ_{TM}) and the stability and co-existence of Ce^{3+} and Ce^{4+}, which largely alters oxygen vacancy concentration. GDC is likely in a similar compressive stress regime to YDZ after deposition; however the elastic modulus of GDC is strongly altered by oxygen vacancy concentration, while that of YDZ is not.[58, 59] By varying the fraction of each component in the single fluorite crystal synthesized, the anion vacancy concentration is modulated and hence, the elastic modulus is a function of composition which leads to varying mechanical buckling behavior of the membranes. The membranes were thermally cycled in air to

determine whether they would be suitable for SOFC application and determine the effect of oxygen incorporation into the materials. In this study, only free standing membranes with compositions having $x \geq 0.5$, survive two heating cycles in the 25 °C – 550 °C range. These results suggest that the mechanical limitations for free standing thin film electrolytes can be overcome by tuning stress in oxide alloy films by altering composition. Other methods to engineer film stress, such as deposition rate or post-growth conditioning, could make it possible to extend the composition range.[42, 137]

5.2.2 Fuel cell fabrication

SOFCs with thin film electrolyte membranes were fabricated using a 100 nm thick $x = 0.5$ material, i.e. $YDZ_{0.5}GDC_{0.5}$. This electrolyte represents the largest departure from pure YDZ ($x = 1$) that is thermo-mechanically stable. The performance and schematic of such free standing structures is shown in Figure 6(a and c). A maximum power density of 1025 mW/cm^2 was obtained with an open circuit voltage (OCV) of 0.413 V at 510 °C. This is among the highest power densities for SOFCs integrating thin film electrolyte membranes reported in this temperature range.[38] Explanation for the deviation of the measured OCV to the Nernst potential of 1.06 V at this temperature is likely due to a percolating electronic path through the membrane. It is known that the mixed valence of Ce leads to a non-negligible electronic contribution to its total conductivity in reducing atmospheres and the addition of YDZ leads to increased electronic conductivity.[11, 156] As discussed in Section 1.2.2, the linear region of the fuel cell I-V curve predominantly corresponds to the Ohmic loss associated with O^{2-} transport across the electrolyte. As shown in Chapter 3, model high performance SOFCs have been fabricated with YDZ electrolyte membranes; however the area specific resistance (ASR) of such SOFCs was on the order of 0.083 Ω cm^2. The SOFCs presented in Figure 6 have an ASR half as large, 0.041 Ω cm^2, showing how mixed conductivity can potentially increase power density at the cost of reducing voltage efficiency. As described in Chapter 3, depending on

application defined power requirements this aspect could be utilized to drive large ionic-electronic currents for large areal power densities.

Figure 5- 6: Oxide alloy fuel cell characteristics

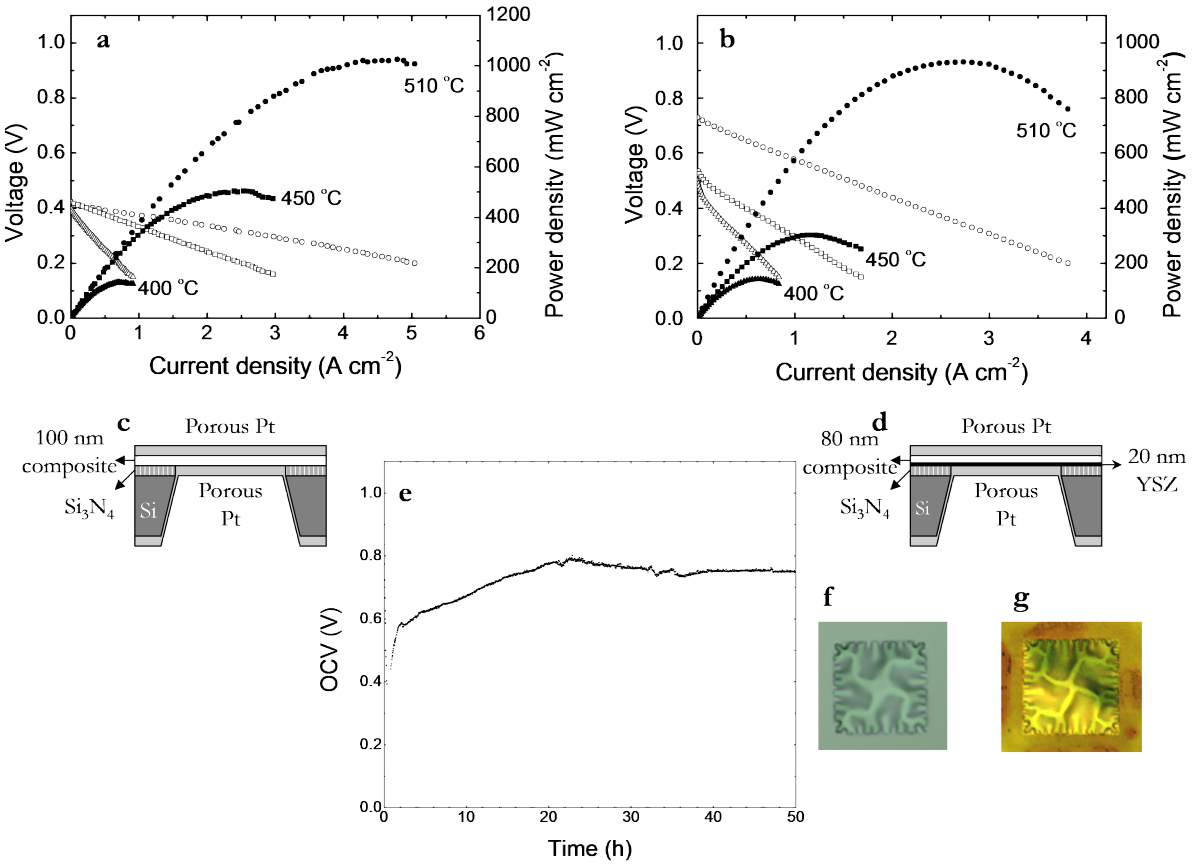

SOFCs with oxide alloy electrolytes. ***(a)*** *and* ***(c)*** *show the performance and schematic of a free standing oxide alloy electrolyte SOFC device;* ***(b)*** *and* ***(d)*** *performance and schematic of a robust SOFC with a YDZ buffer layer to prevent electronic leakage;* ***(e)*** *OCV of structure with YDZ barrier (shown in d) under measurement conditions at 450°C for 50 hours;* ***(f)*** *buckling of structure with YDZ barrier layer before measurement; and* ***(g)*** *after 50 hours of testing.*

The inability to achieve ideal OCV creates a large drop in voltage efficiency and difficulty for applications requiring high voltage; therefore in an attempt to circumvent electronic leakage, a 20

nm buffer layer of YDZ was integrated into the 50-50 structure on the anode side. The performance and schematic of this configuration is also shown in Figure 6(b and d). It is interesting to note that the buckling pattern (shown in Figure 6f) is most similar to pure YDZ and that the pattern appears to refine (Figure 6g) after long term testing. A maximal power output of 930 mW/cm^2 was measured with an increased OCV of 0.73 V, indicating that leakage across the membrane due to the mixed valence of Ce does play a role in the observed OCV deviation and that high power density can still be achieved though at lower current densities, likely dominated by ionic current. Since a 20 nm blocking layer does not completely address the OCV issue, other factors may be of concern. For example, 20 nm YDZ may not provide a large enough barrier against electronic leakage mechanisms discussed in Chapter 2. The thinnest free standing YDZ electrolyte with near ideal OCV reported is based on the work in this thesis and is 27 nm. Additionally, though we do not observe any pin-holes or voids by SEM, deviations of the OCV from the theoretical value in thin film based SOFCs is often attributed to partial fuel crossover or leakage due to microstructural defects.[54, 60, 157] There is interesting temperature dependence of the OCV. Should microstructural defects be initially present and subsequently healed during heating, it may explain the jump in OCV observed. The mechanical stability of the free standing composite membrane was further explored by leaving the device at 450 °C for 50 hours under measurement conditions, i.e. fuel flowing and I-V curves being collected. Similar to the discussion in Chapter 3, performance degradation occurred due to microstructural changes in the electrodes; however Figure 6e shows that a reasonably stable OCV was reached and maintained. This is an encouraging indication of the structural and chemical stability of the free standing nanostructured electrolytes fabricated in this study.

5.3 Compositionally graded membrane, YDZ-GDC

Figure 7 summarizes the nanoscale film deposition technique leveraged in this study as well as nomenclature and structure of samples and devices studied herein. In contrast to the homogeneous films discussed in Section 5.2, here we study two cases of films that are functionally graded. The composition for each parent constituent is $Gd_{0.1}Ce_{0.9}O_{2-\delta}$ (GDC) and $Y_{0.16}Zr_{0.84}O_{2-\delta}$ (YDZ). 92-8 samples refer to films that have $v_{GDC} = 0.92$ at the film substrate interface (anode) and $v_{GDC} = 0.08$ at the film air interface (cathode), where v_{GDC} is the volume fraction of GDC. Likewise, 8-92 samples refer to films having $v_{GDC} = 0.08$ at the film substrate interface (anode) and $v_{GDC} = 0.92$ at the film air interface (cathode). All films have a thickness of approximately 85 nm as determined by XRR. As shown in the optical micrographs in Figure 1f, the free standing membranes of these electrolytes are both stable, implying that we have overcome some of the compositionally induced difficulties discussed in Section 5.2 by synergistically combining two materials with different physical properties.

Figure 5- 7: Overview of compositionally graded films

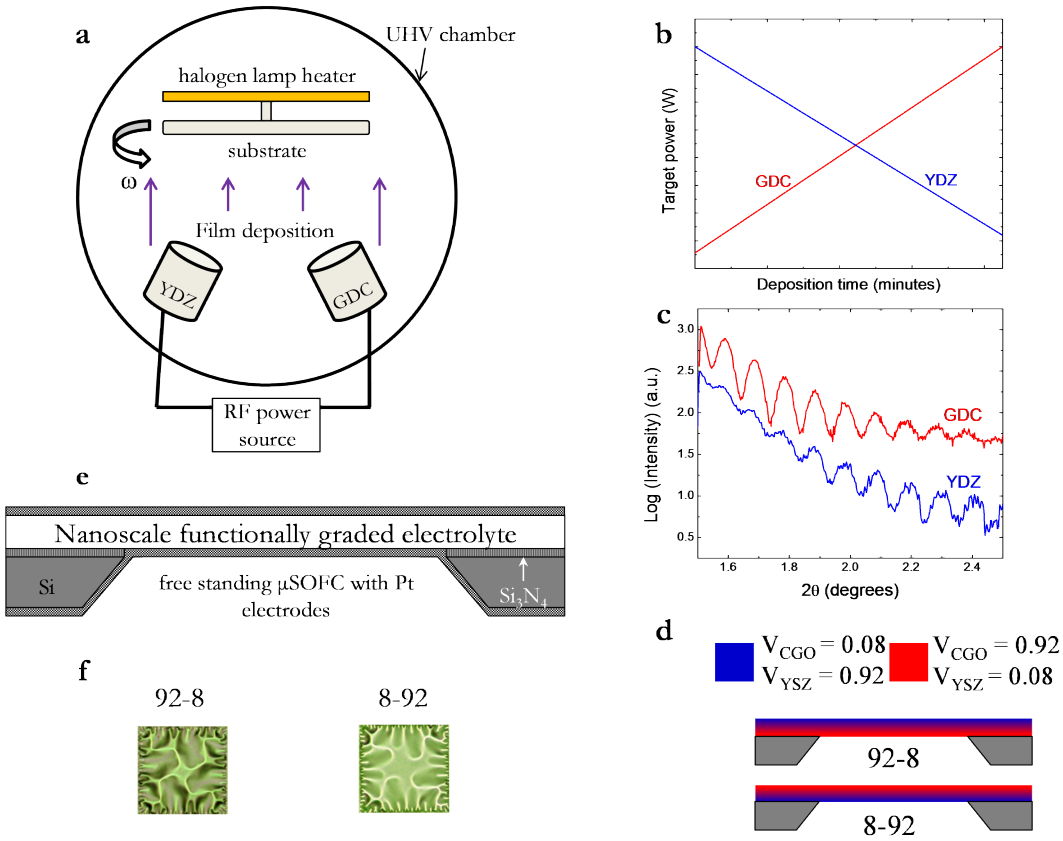

(a) Schematic of the co-sputtering physical vapor deposition process used for graded film growth; (b) linear target power dependence during growth for YDZ and GDC films; (c) representative x-ray reflectivity plots of homogenous YDZ and GDC films used to estimate nominal growth rates; (d) illustration showing the structure of gradient films studied; (e) the final SOFC structure using the nanoscale compositionally graded electrolyte membranes; and (f) optical micrographs of the self-supported, tri-layer structure showing macroscopic buckling patterns similar to those described in Chapter 2 and Section 5.2.

5.3.1 Characterization

Nanoscale compositional variation in the graded films was characterized by X-ray photoelectron spectroscopy (XPS). Due to the relatively short free electron escape path, XPS probes near surface regions within a few nm. Ar sputtering was used to mill the sample surface periodically to investigate the XPS characteristics of the compositionally graded films through the thickness. The

ratio of CeO_2 3d and ZrO_2 3d lines were used as an indication of how relative concentration of each element varies through the film thickness. Figure 8a shows a plot of the normalized (to the expected initial volume fraction) ratio of CeO_2 and ZrO_2 as a function of sputtering time for an 8-92 film (i.e. low GDC at the film-substrate interface). A nearly linear variation of composition as a function of sputtering time is observed, consistent with the linear grading of target power during film deposition outlined in the experimental section. Complexity remains in determining the exact stoichiometry as a function of thickness due to the existence of several oxidation states of CeO_2 and slightly different sputtering rates of each element. However, the raw XPS spectra for select intervals of sputtering time are shown in Figure 8b and Figure 8c shows a magnified view of ZrO_2 3d lines, indicating the strong depth dependence of ZrO_2 concentration. Based on the average Ar milling rate of the film, which was estimated from the total film thickness over the time needed to reach substrate non-trivial silicon signals, each interval of collected XPS spectra probes compositional variation over approximately 4 nm.

Figure 5- 8: XPS of graded electrolyte film

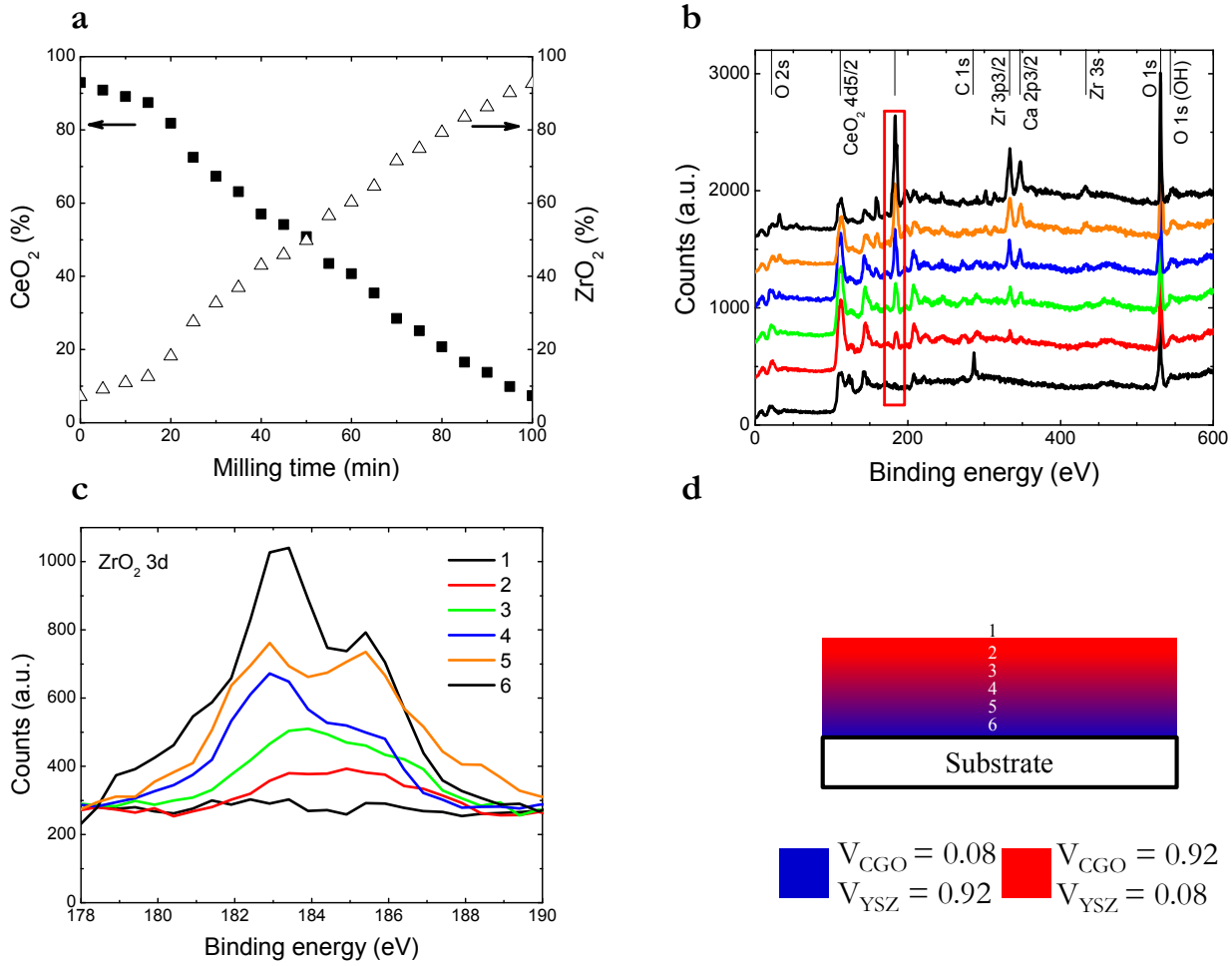

(a) *Depth dependent compositional ratio of Ce and Zr from XPS spectra for 8-92 (low GDC at film-substrate interface) electrolyte. Square and triangle symbols refer to normalized percentage of CeO_2 and ZrO_2, respectively.* ***(b)*** *Raw XPS spectra of the 8-92 films at select intervals of sputtering with peaks indexed according to the National Institute of Standards and Technology (NIST) XPS database. Ca impurities are seen at increasing ZrO_2 content, likely originating from sintering aids or impurities in the precursor YDZ sputtering target;* ***(c)*** *a close-up view of ZrO_2 3d lines for selected sputtering times showing the substantial change ZrO_2 content as a function of depth;* ***(d)*** *a schematic of the 8-92 film with labels depicting the approximate positions of XPS scans shown.*

Cross-section transmission electron micrographs (TEM) of a representative 92-8 film (high GDC at the film-substrate interface) are shown in Figure 9a-c. A continuous columnar structure is seen along the film growth direction. This is similar to the microstructure observed for homogeneous GDC

and YDZ films grown by physical vapor deposition.[35, 158] Scanning electron microscopy (SEM) indicated that macroscopically, films appeared to be free of observable cracks or voids that could restrict optimal electrochemical performance. Figure 9d shows the surface morphology of as-grown films taken using a charge compensated SEM. Surfaces with high volume fraction of GDC or YDZ exhibit similar granular microstructural features with grain size in the 15–25 nm range, much like homogeneous YDZ films and oxide alloys discussed in Chapter 3 and Section 5.2, respectively.

Figure 5- 9: Microstructural characterization of graded films

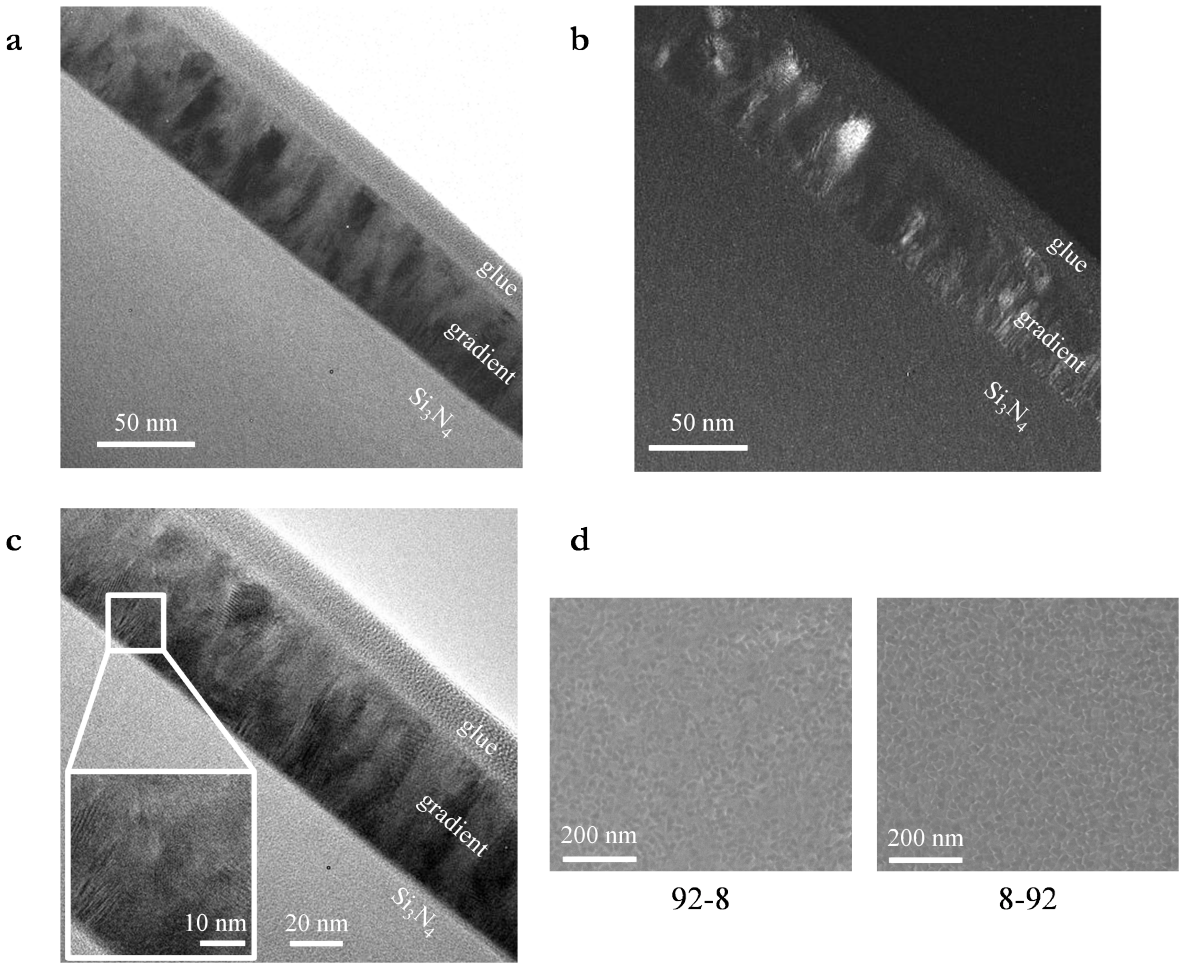

(a) *Cross-sectional bright field TEM image of 92-8 (high GDC at substrate-film interface) electrolyte;* ***(b)*** *dark field (111) TEM image;* ***(c)*** *high resolution bright field image showing the columnar, granular, polycrystalline nature of the films; and (d) charge compensated SEM image depicting the surface morphology of as-deposited films.*

Figure 10a shows glancing incidence x-ray diffraction (XRD) patterns taken on as-deposited thin films. Films of the parent phases, GDC and YDZ, are shown for reference. They exhibit a polycrystalline, single phase, fluorite crystal structure within the limits of detection. The estimated cubic lattice parameter for GDC and YDZ was found to be 0.298 nm and 0.315 nm, respectively; matching well to tabulated values of 0.297 nm and 0.313 nm from the international center for diffraction data (ICDD 030-1460 for YDZ and 01-075-0161 for GDC). Interestingly, the graded electrolyte structure shows indication of two phase co-existence. Unlike the previously discussed co-sputtered GDC-YDZ that show evidence of solid solution,[82] the graded films show character of both GDC and YDZ phases. In particular, the (220) reflection clearly shows the existence of two peaks. A Gaussian fit of two separate peaks for the (111) reflection also appears reasonable during whole pattern fitting. Due to the absence of any reflections at 2θ~43° or splitting of the high angle (004) plane (not shown), the presence of the tetragonal phase (ICDD 01-070-4431), within the limits of XRD detection is unlikely.

Figure 5- 10: XRD of graded electrolyte

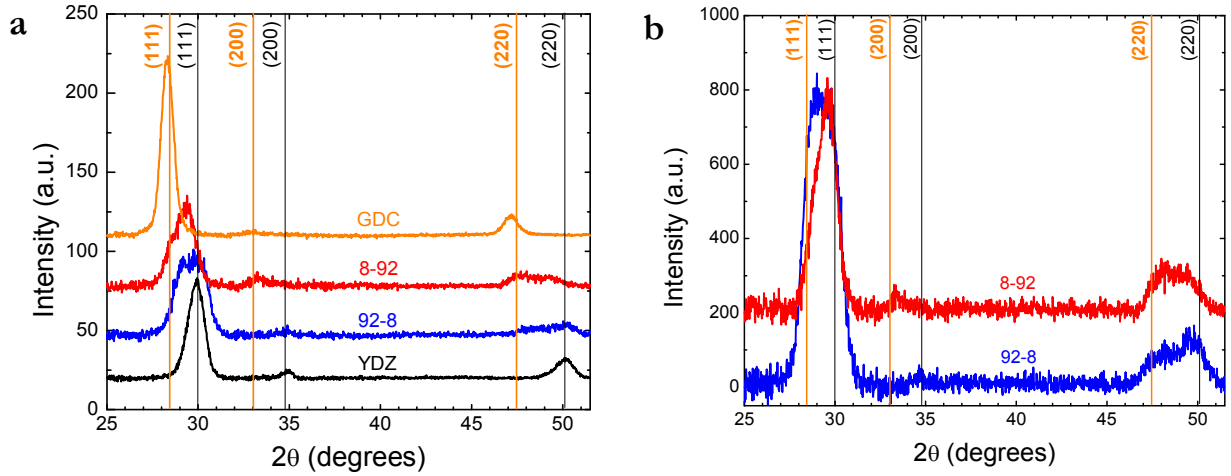

(a) *XRD patterns of YDZ, GDC, 92-8, 8-92 electrolytes taken from as-deposited films;* ***(b)*** *XRD patterns of graded electrolytes after annealing at 600 °C for 24 hours exhibiting the co-existence of two cubic crystals. Solid lines represent tabulated ICDD peak positions for GDC and YDZ.*

To test the possibility of phase metastability, the films were annealed in air at 600 °C for 24 hours. In the context of ZrO_2 based materials, this is a relatively low temperature; however, with regard to applications as new electrolytes for low temperature thin film SOFCs, this is in the high range of operating temperatures. Figure 10b shows the XRD pattern of the films post annealing. While slight shift in peak positions occur, likely originating from oxygen incorporation, the (220) peaks are most clear in showing that co-existence of two phases remains.

5.3.2 Fuel cell integration and testing with H_2

To demonstrate the functionality of the graded electrolyte membranes, SOFCs integrating both thin film electrolyte membrane configurations (8-92 and 92-8) were fabricated. Figure 11a-b shows the performance of such devices using hydrogen (H_2) fuel. A maximum power density of 1177 mW/cm^2 and 412 mW/cm^2 at 520 °C was demonstrated using the 92-8 (high GDC at film-substrate interface; fuel cell anode) and 8-92 (low GDC at film-substrate interface; fuel cell anode) electrolytes, respectively. As discussed in previous Chapters, numerous processes can influence power density; however, the temperature dependence fits well to a single activation energy (E_a). In this study, E_a was found to be 1.59 eV and 1.01 eV for μSOFCs with 92-8 and 8-92 electrolytes, respectively. Activation for 8-92 (low GDC at anode) electrolytes is comparable to the 1.07 – 1.11 eV range for similar cells with Pt electrodes using co-sputtered YDZ-GDC solid solution and homogenous YDZ electrolyte.[82, 83, 140] On the other hand, the activation energy for 92-8 (high GDC at anode) electrolytes is not, which is likely related to complex transport behavior, discussed below.

Figure 5- 11: SOFC characteristics using graded electrolytes and H_2 fuel

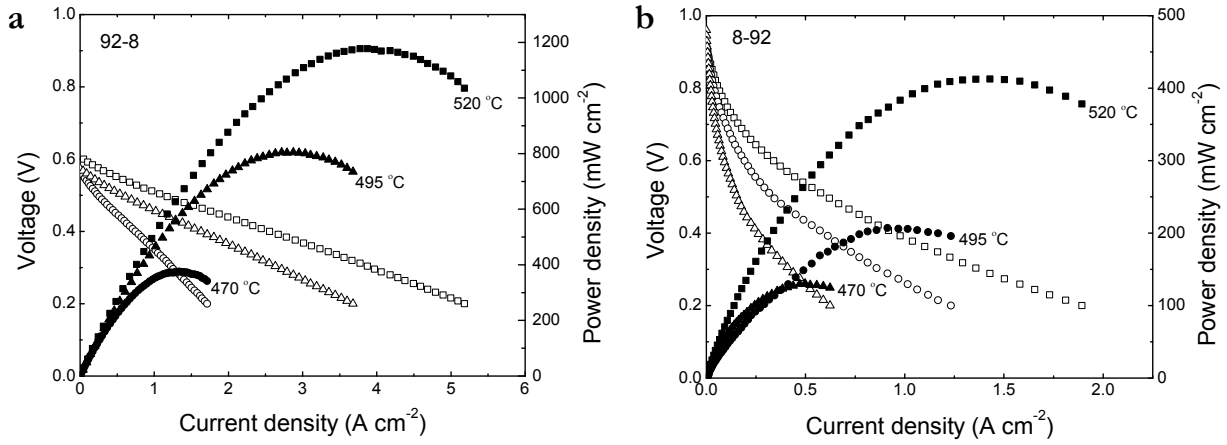

Low temperature SOFC fuel cell performance using hydrogen as fuel and standing air as the oxidant for ***(a)*** *free standing 92-8 (high GDC at anode) electrolytes and* ***(b)*** *8-92 (low GDC at anode) electrolytes; open and closed symbols represent I-V and I-P characteristics, respectively.*

The open circuit voltage (OCV) represents the thermodynamic potential that is generated by a difference in electrochemical potential on either side of the electrolyte. In the temperature range investigated here, the OCV should be approximately 1 V. At zero overpotential, SOFCs integrating the 8-92 (low GDC at anode) structure exhibit an OCV of 0.95 V, close to the theoretical value. On the other hand, SOFCs with 92-8 (high GDC at anode) electrolytes do not exceed 0.60 V. The OCV is affected by catalytic activity of the electrodes or leakage through the electrolyte. Unlike the oxide electrodes explored in Chapter 4, Pt is a good electrocatalyst for both oxygen reduction and hydrogen oxidation. Therefore, the deviation from ideal OCV is an indication of either electronic leakage or fuel permeation across the electrolyte. The difference between the sample with v_{GDC} = 0.08 and v_{GDC} = 0.92 on the anode surface points to a composition related issue and discounts the likelihood of fuel permeation. As discussed in Section 5.2, the co-existence of Ce^{3+} and Ce^{4+} in reducing atmosphere, such as the anode environment, may give rise to a non-negligible electronic carrier concentration and therefore, mixed conductivity.[11]

Based on XRD results above, the graded structure appears to be a two-phase composite, albeit complex in compositional variation. Generalized effective medium (GEM) theory describes how macroscopic properties of composite materials can be expressed as a function of the properties and volume fraction of each constituent component.[159] In a two-phase composite where one phase is electronically insulating and the other conducting, there exists a limit in which a long range conductive path will emerge. This limit, known as the percolation threshold, is close to $v_{conductor}$ = 0.15 in experimental studies of discrete spherical particles.[159, 160] Under the reducing anodic conditions, if GDC is considered to be the electronically conducting phase, the fact that SOFCs with v_{GDC} = 0.08 at the anode have a near ideal OCV and SOFCs with v_{GDC} = 0.92 at the anode are leaky is consistent with a possible percolative electronic path through the thickness; arising from mixed conduction in CeO_2 due to a high fraction of Ce^{3+} at the anode surface. It is also noted that particle size, shape, and distribution will affect the threshold value.

The second main difference between the curves in Figure 11 is the current density. At 520 °C, SOFCs with 92-8 (high GDC at anode) electrolytes exhibit current density over two times that of SOFCs with 8-92 (low GDC at anode) electrolytes. In addition to electrolyte conductivity and mixed conductivity in the 92-8 case, electrode morphology can play a significant role in determining current density. The work in Chapter 3 has indicated the sensitivity of anode microstructure in such devices, therefore; Pt electrodes were grown simultaneously for all samples. Figure 12a-d shows the electrode morphology after testing, for both electrolyte configurations.

Figure 5- 12: SEM of Pt electrode morphology after operation

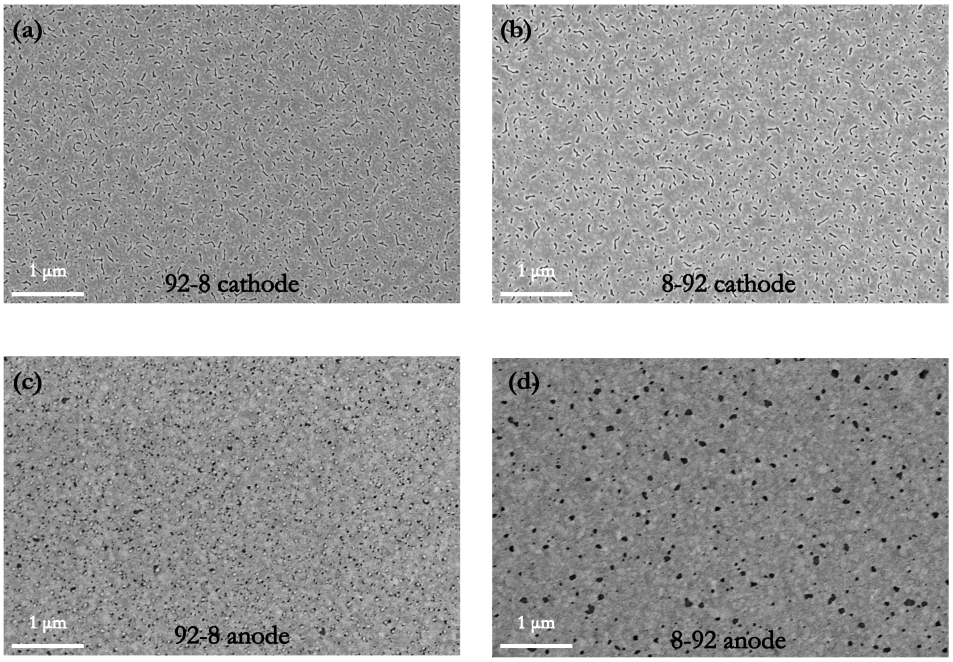

SEM images of the nanoporous Pt ***(a)*** *92-8 cathode,* ***(b)*** *8-92 cathode,* ***(c)*** *92-8 anode, and* ***(d)*** *8-92 anode after fuel cell measurements in hydrogen. A difference in morphology can be seen in the anodes due to the dominant surface at the electrode/electrolyte interface.*

The cathode morphology is similar in both cases, however, the pore size and number distribution on the anode is clearly different. Surface energy of both the metal and oxide surface are important in determining equilibrium microstructural rearrangement. Further, increased Pt mobility in reducing environments has been shown in Chapter 3 and work characterizing Pt self-diffusion in the presence of H_2.[83, 161] Studies comparing Pt and a Pt-Ni alloy indicated different microstructural characteristics at high temperature on congruent, i.e. similar surface microstructure, roughness, and composition, YDZ surfaces.[113] We have a comparable case, albeit with a single metal surface (Pt) and two alternate oxide surfaces, one with a high volume fraction of GDC and the other with a high volume fraction of YDZ. The microstructural coarsening on the latter is similar to what has been seen previously; however, there is a noticeable difference in the microstructure of the surface with a high volume

fraction of GDC, pointing to the significance of the surface energy interaction between Pt and the oxide surface.

5.3.3 Fuel cell integration and testing with CH_4

Aliovalently doped ceria has been used as a catalyst and matrix support for methane oxidation, and exhibits the ability to suppress coking (solid carbon formation).[162] Here, we leverage two methods to reduce coking, namely lower temperature operation and a small fraction of doped ceria at the electrode/electrolyte interface using the compositionally graded electrolyte. In doing so, high performance direct methane SOFCs have been realized. In order to mitigate electronic leakage due to the reducing environment of the anode, SOFCs with 8-92 (low GDC at the anode) electrolytes were fabricated with nanoporous Ru anodes for direct methane operation. For the sake of completeness, 92-8 (high GDC at anode) electrolytes were also tested and confirmed the hypothesis that a critical volume fraction of GDC at the anode/electrolyte interface is vital in avoiding a percolative electronic path. At 520 °C, such devices exhibited a maximum power density of 280 mW/cm^2 with OCVs that never exceeded 0.4 V. Conversely, the performance of SOFCs with 8-92 electrolytes, shown in Figure 13 at several temperatures, exhibited high performance characteristics.

Figure 5- 13: SOFC characteristics using graded electrolyte and CH_4 fuel

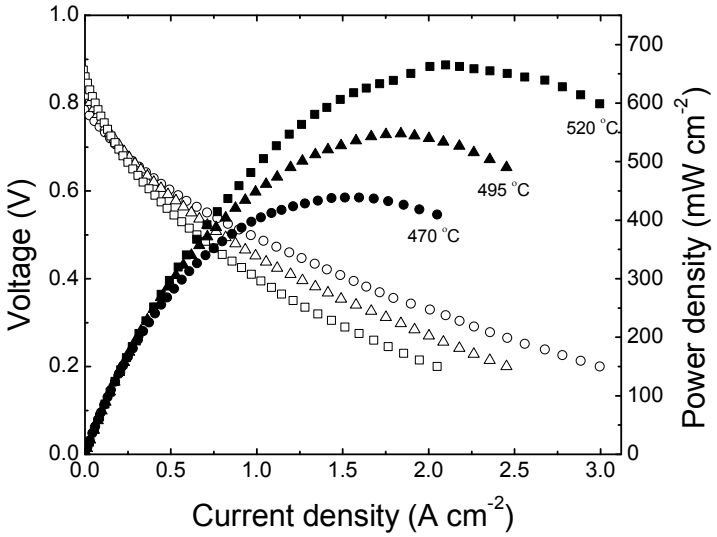

SOFC performance using methane as fuel with a free standing 8-92 (low GDC at anode) electrolyte membrane. Open and closed symbols represent I-V and I-P characteristics, respectively.

An OCV of 0.85 V and a maximum power density of 665 mW/cm^2 were obtained at 520 °C. At lower temperature, around 350 °C, the OCV was as high as 0.95 V, but dropped and stabilized at 0.85 V at 400 °C. Under these testing conditions the complete and partial oxidation of methane is expected to result in an OCV of 1.13 V and 1.05 V at 500 °C. Previous research has shown that complete oxidation is unlikely to occur in one step, which may contribute to the deviation from ideal OCV in the SOFCs presented here.[163] SEM micrographs (not shown) show no evidence of macroscopic carbon deposition, such as carbon fibers, that has been observed previously in direct methane thin film SOFCs.[164] Though this does not completely discount the possibility of coking, it is an encouraging indication of suppression. In this temperature range, the graded structure demonstrated a peak power density higher than previous reports of thin film SOFCs with homogeneous electrolyte compositions.[38] If the temperature dependence of the maximum power density for devices having 8-92 graded electrolyte and pure YDZ is considered as an activated

process, the kinetic barrier for peak power density at reduced temperatures appears to be lower in 8-92 electrolyte (~0.72 eV) compared with similar cells using a homogenous YDZ thin film electrolyte (~0.97 eV).[165] As mentioned previously, the barrier for similar cells with homogeneous YDZ electrolytes operating with H_2 as fuel is typically on the order of 1 eV. SOFCs operating in methane with 8-92 electrolytes appear to have a lower barrier, likely related to the presence of CeO_2 at the electrolyte/anode interface. This electrochemically active oxide may lead to an increased number of active sites for oxidation.[146]

5.4 Conclusion

This chapter has shown that new approaches to electrolyte fabrication can increase the potential design space for materials used as ultrathin components in SOFCs. Oxide alloys of YDZ and GDC were fabricated at relatively low temperatures and exhibit high performance using model Pt electrodes. Compositionally graded electrolytes combine the mechanical integrity of YDZ with the unique properties of GDC to demonstrate mechanically stable, potentially multi-functional membranes.

6 SUMMARY

6.1 Main results of thesis

We have studied free standing oxide membranes for use as electrolytes in ultrathin SOFCs. We find that compressive film stress induced buckling is a necessary design component for mechanically robust membrane structures. Control of thin film stress via deposition pressure and film thickness has enabled the demonstration of membrane structures consistent with numeric models based on simple elastic theories. The integration of brittle oxide membranes onto a widely used polymeric system (Kapton by DuPont) was shown. Model Pt|YDZ|Pt structures were studied to demonstrate the ultimate performance possibilities at reduced electrolyte thicknesses down to 27 nm. The fuel cell performance did not monotonically increase with decreasing electrolyte thickness at temperatures above 450 °C. An empirically based physical model for mechanisms limiting the power output of such SOFCs was developed and implies that electronic leakage due to defects is the dominant origin for reduced power density. Further, electrode microstructure plays a vital role on the scaling characteristics of the electrolyte. Optimization of Pt anode microstructure in a Pt|YDZ|Pt cell enabled the demonstration of a planar SOFC having a 108 nm thick electrolyte exhibiting a power density of over 1 W/cm^2 at 500 °C using hydrogen fuel. Our model shows that dielectric breakdown is the crucial material property that sets the boundary for electrolyte thickness reduction, limiting ideal charge separation to a thickness of ~6 nm. Complex oxide electrode materials (LSCF and BSCF) were meticulously grown, characterized, and integrated onto the free standing membrane structures by stress control. These devices represent the first free standing oxide heterostructures reported to date and utilize the YDZ membrane system as a platform to test new electrode materials at reduced temperatures. LSCF shows promise as a low temperature cathode, while BSCF does not appear to be viable long term candidate due to poor performance and possible parasitic reactivity with YDZ. Finally, using a co-sputtering technique, novel electrolyte materials

combining YDZ and GDC were created. Oxide alloys of these materials appear to enable a tunable conductivity and devices integrating such electrolytes exhibit high current densities, due to mixed conductivity, while also producing over 1 W/cm^2 at 500 °C. Compositionally graded electrolytes with cation concentration varying on the nanoscale were developed and characterized. These materials synergistically combine properties of YDZ and GDC parent phases, making them thermo-mechanically stable and electrochemically active. SOFCs with these electrolytes exhibit high power densities using hydrogen fuel, but also show a power density of nearly 0.7 W/cm^2 at 520 °C using methane fuel.

6.2 Outlook and future work

Oxide membranes are a powerful experimental platform; this thesis has advanced the understanding and application of canonical oxide ion conductors for SOFC applications. Potential future research directions building on ideas and results in this thesis are outlined below.

1. **Influence of stress on ionic conductivity.** In recent years the influence of mechanical stress on ionic conductivity has been of large interest.[166-168] Processing will influence film stress and therefore must be well characterized. Regarding conductivity, oxide membranes are well positioned as a research platform to provide unambiguous experimental data (i.e. no substrate interfacial phenomena) on cross-plane conductivity to determine the role of film stress on ionic conductivity. For example, recently Garbayo el. al. have shown that the lateral ionic conductivity of 60 nm YDZ films is an order of magnitude smaller than the cross plane conductivity in YDZ membranes of the same thickness.[169]
2. **Stable patterned electrodes with adequate TPB length.** High performance SOFCs were only possible using porous electrodes with large TPB lengths, on the order of 100,000 cm/cm^2. Using polymer sphere lithography, researchers have shown that patterned metallic

electrodes can be fabricated and are stable at elevated temperatures;[117] however pattern densities are on the order of 10,000 cm/cm^2.[115] Photolithography will likely not be able to move beyond this pattern density and has been explored in the past for isolated half-cell experiments.[125] E-beam lithography or advanced self-assembly techniques to create high density patterns of nanoscale electrodes could advance the engineering of high power devices and the science of interface change transfer mechanisms.

3. **Low temperature oxide electrodes.** While metallic electrodes are excellent for proof-of-concept device demonstrations, unless patterned structures can be fabricated, they are unstable over extended periods of time. Further, they can be cost prohibitive for widespread adoption. This thesis has opened up the low temperature SOFC regime (down to 300 °C) using classic electrolyte materials. In order to take advantage of this temperature reduction, new oxide electrodes that are catalytically active, stable, and have adequate electronic conductivity must be developed. At the nanoscale, such electrodes can be monolithically integrated into the entire stack by using a compositionally graded structure. Moreover, new electrodes that have multiple functionality,[170] such as catalytic activity and charge storage characteristics could enable hybrid energy conversion and storage devices.
4. **Exploration of transport mechanisms in graded electrolyte.** Compositional grading on the nanoscale is a powerful tool to develop materials with synergistic properties. However, complex transport phenomena must be addressed in detail. The classic fundamentals for ionic transport are characterized by a brick-layer model,[171] which assumes a homogeneous material (grain interior) surrounded by a finite boundary layer (grain boundary). Advanced transport models integrating knowledge from composite structures, such as generalized effective medium theory, should serve as building blocks to determine how mixed ionic-electronic transport can be understood in nanoscale graded materials. Additionally, surface

sensitive experiments characterizing the electrochemical advantage of heterogeneous oxide interfaces would be an excellent way to migrate from decorated surface structures currently being pursued in isolation from devices,[172] to fully integrated advanced energy conversion technologies.

5. **Mechanics of membranes at large system pressures and temperatures.** Classic work on the buckling configurations of micromachined square Si_3N_4 membranes is corroborated by our numerical simulations.[68] The analysis was extended to include pressure induced membrane buckling transitions up to 40 kPa.[173] For a square Si_3N_4 membrane having side length of 1.04 mm, a buckling pattern transition was observed at ~25 kPa. Understanding the underlying physics of this aspect in depth and the limitations of membrane (both supported and unsupported) is necessary to advance oxide membranes that can operate at elevated temperature and varying environments. It is of particular significance since large system pressures (on the order of hundreds of kPa) will be needed for industrial applications in fuel cells and gas separation technology.[38]
6. **Demonstration of gas separation capability.** Membrane based gas separation technologies have long touted the benefits of thickness reduction for higher ionic throughput in selectively permeable oxide materials. Mixed conducting complex oxides, $0< t_i <1$, such as LSCF and BSCF have applications in industrial processes for conversion of CH_4.[174-176] Using several mixed conducting membranes in series can allow simultaneous generation and separation of H_2 and N_2.[177] Oxide membranes having $t_i = 1$ have use in the production of high purity oxygen from air,[178] and generating H_2 with an external current applied (i.e. in electrolytic mode).[179] The operating principle of the latter is similar to SOFCs, but utilized in regenerative mode to produce H_2 from H_2O via electrolysis. In order to be economically feasible, these processes require large volumes of feedstock, high geometric

membrane area, and operation at large system pressures, all of which constitute worthy research topics in the context of oxide membranes.

While this thesis has demonstrated some promising initial results, significant engineering challenges remain for complete integration. Collaborative researchers in Europe have attempted to create a full battery replacement system using a thin film SOFC.[65] Additionally, the start-up company Nectar (formerly Lilliputian) has developed proprietary methods to seal, insulate, and package a SOFC device for remote commercial recharging of consumer products.[63] Nevertheless, interdisciplinary programs that push traditional limits will be vital in bringing fresh perspectives to bridge the gaps needed to move forward. High level issues that warrant investigation include thermal, fuel, and power management, as well as integration of miniature devices onto functional substrates, for example as synergistic power generating heat sinks.

7 REFERENCES

1 S. Arrhenius, Philosophical Magazine Series 5 **41**, 237 (1896).
2 IPCC, http://www.ipcc.ch/pdf/assessment-report/ar4/syr/ar4_syr_spm.pdf, (2007).
3 Turbine, http://www.mpoweruk.com/steam_turbines.htm.
4 EIA, http://www.eia.gov/tools/faqs/faq.cfm?id=107&t=3.
5 W. R. Grove, Philosophical Magazine Series 3 **14**, 127 (1839).
6 C. Borgnakke and R. E. Sonntag, *Fundamentals of Thermodynamics* (Wiley, 2012).
7 DOE, http://www1.eere.energy.gov/hydrogenandfuelcells/fuelcells/fc_types.html#comparison.
8 B. C. H. Steele and A. Heinzel, Nature **414**, 345 (2001).
9 W. Nernst, Elektrochem. **6** (1900).
10 C. Wagner, Naturwissenschuften **31**, 265 (1943).
11 J. B. Goodenough, Annual Review of Materials Research **33**, 91 (2003).
12 V. V. Kharton, F. M. B. Marques, and A. Atkinson, Solid State Ionics **174**, 135 (2004).
13 J. W. Fergus, Journal of Materials Science **38**, 4259 (2003).
14 W. Jung, J. L. Hertz, and H. L. Tuller, Acta Materialia **57**, 1399 (2009).
15 D. Marrocchelli, P. A. Madden, S. T. Norberg, and S. Hull, Chemistry of Materials **23**, 1365 (2011).
16 J. W. Fergus, Journal of Power Sources **162**, 30 (2006).
17 H. L. Tuller and A. S. Nowick, Journal of The Electrochemical Society **122**, 255 (1975).
18 V. V. Kharton, et al., Journal of Materials Science **36**, 1105 (2001).
19 J. A. V. Butler, Transactions of the Faraday Society **19**, 729 (1924).
20 J. A. V. Butler, Transactions of the Faraday Society **19**, 734 (1924).
21 T. Erdey-Gruz and M. Volmer, Z. Phys. Chem. A **150**, 203 (1930).
22 H. H. Bauer, Journal of Electroanalytical Chemistry and Interfacial Electrochemistry **16**, 419 (1968).
23 C. H. Hamann, A. Hamnett, and W. Vielstich, *Electrochemistry* (Wiley, 1998).
24 S. A. Barnett, Energy **15**, 1 (1990).
25 R. P. O'Hayre, *Fuel cell fundamentals* (John Wiley & Sons, 2006).
26 S. B. Adler, J. A. Lane, and B. C. H. Steele, Journal of The Electrochemical Society **143**, 3554 (1996).
27 J. R. Wilson, et al., Nature materials **5**, 541 (2006).
28 J. Joos, T. Carraro, A. Weber, and E. Ivers-Tiffée, Journal of Power Sources **196**, 7302 (2011).
29 A. V. Virkar, J. Chen, C. W. Tanner, and J.-W. Kim, Solid State Ionics **131**, 189 (2000).
30 S. H. Chan, K. A. Khor, and Z. T. Xia, Journal of Power Sources **93**, 130 (2001).
31 S. de Souza, S. J. Visco, and L. C. De Jonghe, Solid State Ionics **98**, 57 (1997).
32 X. Chen, N. J. Wu, L. Smith, and A. Ignatiev, Applied Physics Letters **84**, 2700 (2004).
33 K. Kerman, T. Tallinen, S. Ramanathan, and L. Mahadevan, Journal of Power Sources **222**, 359 (2013).
34 J. Will, A. Mitterdorfer, C. Kleinlogel, D. Perednis, and L. J. Gauckler, Solid State Ionics **131**, 79 (2000).
35 D. Beckel, A. Bieberle-Hütter, A. Harvey, A. Infortuna, U. P. Muecke, M. Prestat, J. L. M. Rupp, and L. J. Gauckler, Journal of Power Sources **173**, 325 (2007).
36 J. H. Shim, et al., Journal of Materials Chemistry A **1**, 12695 (2013).
37 A. Evans, A. Bieberle-Hütter, J. L. M. Rupp, and L. J. Gauckler, Journal of Power Sources **194**, 119 (2009).
38 K. Kerman and S. Ramanathan, Journal of Materials Research **29**, 320 (2014).

[39] M. F. Ashby and D. R. H. Jones, *Engineering Materials 1: An Introduction to Properties, Applications and Design* (Elsevier Science, 2005).
[40] V. T. Srikar, K. T. Turner, T. Y. Andrew Ie, and S. M. Spearing, Journal of Power Sources **125**, 62 (2004).
[41] Y. Tang, K. Stanley, J. Wu, D. Ghosh, and J. Zhang, Journal of Micromechanics and Microengineering **15**, S185 (2005).
[42] N. Yamamoto, D. J. Quinn, N. Wicks, J. L. Hertz, J. Cui, H. L. Tuller, and B. L. Wardle, Journal of Micromechanics and Microengineering **20**, 035027 (2010).
[43] Y. Safa, T. Hocker, M. Prestat, and A. Evans, Journal of Power Sources **250**, 332 (2014).
[44] A. Evans, et al., Fuel Cells **12**, 614 (2012).
[45] K. Kerman, Q. Van Overmeere, M. Karpelson, R. J. Wood, and S. Ramanathan, ACS Nano **7**, 10895 (2013).
[46] K. V. L. V. Narayanachari and S. Raghavan, Journal of Applied Physics **112**, 074910 (2012).
[47] L. B. Freund and S. Suresh, *Thin Film Materials: Stress, Defect Formation and Surface Evolution* (Cambridge University Press, 2003).
[48] H. Hayashi, T. Saitou, N. Maruyama, H. Inaba, K. Kawamura, and M. Mori, Solid State Ionics **176**, 613 (2005).
[49] Y. Okada and Y. Tokumaru, Journal of Applied Physics **56**, 314 (1984).
[50] S. Giraud and J. Canel, Journal of the European Ceramic Society **28**, 77 (2008).
[51] I. Kosacki, T. Suzuki, V. Petrovsky, and H. U. Anderson, Solid State Ionics **136–137**, 1225 (2000).
[52] H. Huang, T. M. Gur, Y. Saito, and F. Prinz, Applied Physics Letters **89**, 143107 (2006).
[53] A. Karthikeyan, M. Tsuchiya, C.-L. Chang, and S. Ramanathan, Applied Physics Letters **90**, 263108 (2007).
[54] S. Rey-Mermet and P. Muralt, Solid State Ionics **179**, 1497 (2008).
[55] A. C. Johnson, A. Baclig, D. V. Harburg, B.-K. Lai, and S. Ramanathan, Journal of Power Sources **195**, 1149 (2010).
[56] S. Rey-Mermet, Y. Yan, C. Sandu, G. Deng, and P. Muralt, Thin Solid Films **518**, 4743 (2010).
[57] C.-W. Kwon, J.-W. Son, J.-H. Lee, H.-M. Kim, H.-W. Lee, and K.-B. Kim, Advanced Functional Materials **21**, 1154 (2011).
[58] Y. Wang, K. Duncan, E. D. Wachsman, and F. Ebrahimi, Solid State Ionics **178**, 53 (2007).
[59] K. L. Duncan, Y. Wang, S. R. Bishop, F. Ebrahimi, and E. D. Wachsman, Journal of the American Ceramic Society **89**, 3162 (2006).
[60] U. P. Muecke, et al., Advanced Functional Materials **18**, 3158 (2008).
[61] C.-C. Chao, C.-M. Hsu, Y. Cui, and F. B. Prinz, ACS Nano **5**, 5692 (2011).
[62] M. Tsuchiya, B.-K. Lai, and S. Ramanathan, Nat Nano **6**, 282 (2011).
[63] S. B. Schaevitz, 824802 (2012).
[64] B.-K. Lai, A. C. Johnson, M. Tsuchiya, and S. Ramanathan, 767916 (2010).
[65] A. Bieberle-Hütter, et al., Journal of Power Sources **177**, 123 (2008).
[66] A. Bieberle-Hutter, et al., Lab on a Chip **12**, 4894 (2012).
[67] D. J. Quinn, B. Wardle, and S. M. Spearing, Journal of Materials Research **23**, 609 (2008).
[68] V. Ziebart, O. Paul, and H. Baltes, Microelectromechanical Systems, Journal of **8**, 423 (1999).
[69] C. D. Baertsch, K. F. Jensen, J. L. Hertz, H. L. Tuller, S. T. Vengallatore, S. M. Spearing, and M. A. Schmidt, Journal of Materials Research **19**, 2604 (2004).
[70] R. J. Wood, B. Finio, M. Karpelson, N. O. Pérez-Arancibia, P. Sreetharan, and J. P. Whitney, 83731J (2012).

71 S. Timoshenko, *Theory of elasticity* (McGraw-Hill book company, inc., 1934).
72 L. L. D. Landau, E. M. Lifshitš, A. M. Kosevitch, and L. P. Pitaevskiĭ, *Theory of Elasticity 7* (Butterworth-Heinemann Limited, 1986).
73 T. Tallinen, J. A. Astrom, and J. Timonen, Nat Mater **8**, 25 (2009).
74 T. Tallinen, J. Ojajärvi, J. A. Åström, and J. Timonen, Physical Review Letters **105**, 066102 (2010).
75 G. G. Stoney, Proceedings of the Royal Society of London. Series A **82**, 172 (1909).
76 H. Windischmann, Journal of Applied Physics **62**, 1800 (1987).
77 F. Spaepen, Acta Materialia **48**, 31 (2000).
78 P. J. Withers and H. K. D. H. Bhadeshia, Materials Science and Technology **17**, 355 (2001).
79 E. Chason, B. W. Sheldon, L. B. Freund, J. A. Floro, and S. J. Hearne, Physical Review Letters **88**, 156103 (2002).
80 J. A. Thornton and D. W. Hoffman, Thin Solid Films **171**, 5 (1989).
81 H. Windischmann, Critical Reviews in Solid State and Materials Sciences **17**, 547 (1992).
82 K. Kerman, B.-K. Lai, and S. Ramanathan, Journal of Power Sources **202**, 120 (2012).
83 K. Kerman, B.-K. Lai, and S. Ramanathan, Journal of Power Sources **196**, 2608 (2011).
84 S. C. Singhal, Solid State Ionics **135**, 305 (2000).
85 S. J. Litzelman, J. L. Hertz, W. Jung, and H. L. Tuller, Fuel Cells **8**, 294 (2008).
86 A. Weber and E. Ivers-Tiffée, Journal of Power Sources **127**, 273 (2004).
87 S. Singhal, S. C. Singhal, and K. Kendall, *High-temperature Solid Oxide Fuel Cells: Fundamentals, Design and Applications: Fundamentals, Design and Applications* (Elsevier Science, 2003).
88 Z. Fan and F. B. Prinz, Nano Letters **11**, 2202 (2011).
89 J. Jiang and J. Hertz, J Electroceram **32**, 37 (2014).
90 J. Fleig, H. L. Tuller, and J. Maier, Solid State Ionics **174**, 261 (2004).
91 J. H. Park and R. N. Blumenthal, Journal of The Electrochemical Society **136**, 2867 (1989).
92 C. A. Mead, Physical Review **128**, 2088 (1962).
93 I. Langmuir, Physical Review **2**, 450 (1913).
94 H.-I. Yoo and J.-H. Hwang, Journal of Physics and Chemistry of Solids **53**, 973 (1992).
95 S. M. Sze, Journal of Applied Physics **38**, 2951 (1967).
96 N. H. Perry, S. Kim, and T. O. Mason, Journal of Materials Science **43**, 4684 (2008).
97 V. M. Orera, R. I. Merino, Y. Chen, R. Cases, and P. J. Alonso, Physical Review B **42**, 9782 (1990).
98 S. M. Sze and K. K. Ng, *Physics of Semiconductor Devices* (Wiley, 2006).
99 V. R. PaiVerneker, A. N. Petelin, F. J. Crowne, and D. C. Nagle, Physical Review B **40**, 8555 (1989).
100 R. H. Fowler and L. Nordheim, in *Proc. R. Soc. London, Ser. A*, 1928), p. 173.
101 J. Cai and C.-T. Sah, Journal of Applied Physics **89**, 2272 (2001).
102 X. Guo and Y. Ding, Journal of The Electrochemical Society **151**, J1 (2004).
103 O. J. Durá, M. A. López de la Torre, L. Vázquez, J. Chaboy, R. Boada, A. Rivera-Calzada, J. Santamaria, and C. Leon, Physical Review B **81**, 184301 (2010).
104 N. Klein and H. Gafni, Electron Devices, IEEE Transactions on **13**, 281 (1966).
105 O. Jongprateep, V. Petrovsky, and F. Dogan, Journal of metals, materials and minerals **18**, 9 (2008).
106 M. Lefèvre, E. Proietti, F. Jaouen, and J.-P. Dodelet, Science **324**, 71 (2009).
107 H. A. Gasteiger, J. E. Panels, and S. G. Yan, Journal of Power Sources **127**, 162 (2004).
108 C. T. Campbell, Surface Science Reports **27**, 1 (1997).
109 H. Huang, M. Nakamura, P. Su, R. Fasching, Y. Saito, and F. B. Prinz, Journal of The Electrochemical Society **154**, B20 (2007).
110 E. Mutoro, S. Günther, B. Luerßen, I. Valov, and J. Janek, Solid State Ionics **179**, 1835 (2008).

[111] H. Galinski, T. Ryll, P. Elser, J. L. M. Rupp, A. Bieberle-Hütter, and L. J. Gauckler, Physical Review B **82**, 235415 (2010).
[112] N. Baumann, E. Mutoro, and J. Janek, Solid State Ionics **181**, 7 (2010).
[113] X. Wang, H. Huang, T. Holme, X. Tian, and F. B. Prinz, Journal of Power Sources **175**, 75 (2008).
[114] J. R. Wilson, M. Gameiro, K. Mischaikow, W. Kalies, P. W. Voorhees, and S. A. Barnett, Microscopy and Microanalysis **15**, 71 (2009).
[115] E. C. Brown, S. K. Wilke, D. A. Boyd, D. G. Goodwin, and S. M. Haile, Journal of Materials Chemistry **20**, 2190 (2010).
[116] Y. B. Kim, C.-M. Hsu, S. T. Connor, T. M. Gür, Y. Cui, and F. B. Prinz, Journal of The Electrochemical Society **157**, B1269 (2010).
[117] A. Y. Lin and P. C. McIntyre, Electrochemical and Solid-State Letters **14**, B96 (2011).
[118] Z. Fan, J. An, A. Iancu, and F. B. Prinz, Journal of Power Sources **218**, 187 (2012).
[119] J. An, Y.-B. Kim, J. Park, T. M. Gür, and F. B. Prinz, Nano Letters **13**, 4551 (2013).
[120] R. Tölke, A. Bieberle-Hütter, A. Evans, J. L. M. Rupp, and L. J. Gauckler, Journal of the European Ceramic Society **32**, 3229 (2012).
[121] I. Garbayo, V. Esposito, S. Sanna, A. Morata, D. Pla, L. Fonseca, N. Sabaté, and A. Tarancón, Journal of Power Sources **248**, 1042 (2014).
[122] H.-S. Noh, K. J. Yoon, B.-K. Kim, H.-J. Je, H.-W. Lee, J.-H. Lee, and J.-W. Son, Journal of Power Sources **247**, 105 (2014).
[123] D. Tsiplakides and C. G. Vayenas, Journal of The Electrochemical Society **148**, E189 (2001).
[124] A. Mitterdorfer and L. J. Gauckler, Solid State Ionics **117**, 187 (1999).
[125] R. Radhakrishnan, A. V. Virkar, and S. C. Singhal, Journal of The Electrochemical Society **152**, A927 (2005).
[126] S. B. Adler, Solid State Ionics **135**, 603 (2000).
[127] C. Sun, R. Hui, and J. Roller, J Solid State Electrochem **14**, 1125 (2009).
[128] Z. Shao and S. M. Haile, Nature **431**, 170 (2004).
[129] Z. Shao, W. Yang, Y. Cong, H. Dong, J. Tong, and G. Xiong, Journal of Membrane Science **172**, 177 (2000).
[130] D. N. Mueller, R. A. De Souza, T. E. Weirich, D. Roehrens, J. Mayer, and M. Martin, Physical Chemistry Chemical Physics **12**, 10320 (2010).
[131] C. Niedrig, S. Taufall, M. Burriel, W. Menesklou, S. F. Wagner, S. Baumann, and E. Ivers-Tiffée, Solid State Ionics **197**, 25 (2011).
[132] A. Petric, P. Huang, and F. Tietz, Solid State Ionics **135**, 719 (2000).
[133] S. Wang, M. Katsuki, M. Dokiya, and T. Hashimoto, Solid State Ionics **159**, 71 (2003).
[134] Y. Teraoka, H. M. Zhang, K. Okamoto, and N. Yamazoe, Materials Research Bulletin **23**, 51 (1988).
[135] J. W. Stevenson, T. R. Armstrong, R. D. Carneim, L. R. Pederson, and W. J. Weber, Journal of The Electrochemical Society **143**, 2722 (1996).
[136] B.-K. Lai, K. Kerman, and S. Ramanathan, Journal of Power Sources **195**, 5185 (2010).
[137] B.-K. Lai, A. C. Johnson, H. Xiong, and S. Ramanathan, Journal of Power Sources **186**, 115 (2009).
[138] K. Fuchs, Proc. Cambridge Phil. Soc. **34**, 100 (1938).
[139] E. H. Sondheimer, Advan. Phys. **1**, 1 (1952).
[140] A. C. Johnson, B.-K. Lai, H. Xiong, and S. Ramanathan, Journal of Power Sources **186**, 252 (2009).
[141] Z. Yáng, A. Harvey, A. Infortuna, J. Schoonman, and L. Gauckler, Journal of Solid State Electrochemistry **15**, 277 (2011).

142 M. Burriel, C. Niedrig, W. Menesklou, S. F. Wagner, J. Santiso, and E. Ivers-Tiffée, Solid State Ionics **181**, 602 (2010).
143 K. Kerman, B.-K. Lai, and S. Ramanathan, Advanced Energy Materials **2**, 655 (2012).
144 L. Wang, R. Merkle, and J. Maier, ECS Transactions **25**, 2497 (2009).
145 Z. Duan, M. Yang, A. Yan, Z. Hou, Y. Dong, Y. Chong, M. Cheng, and W. Yang, Journal of Power Sources **160**, 57 (2006).
146 W. C. Chueh, Y. Hao, W. Jung, and S. M. Haile, Nat Mater **11**, 155 (2012).
147 A. Kossoy, A. I. Frenkel, Y. Feldman, E. Wachtel, A. Milner, and I. Lubomirsky, Solid State Ionics **181**, 1473 (2010).
148 G. A. Tompsett, N. M. Sammes, and O. Yamamoto, Journal of the American Ceramic Society **80**, 3181 (1997).
149 M. Price, J. Dong, X. Gu, S. A. Speakman, E. A. Payzant, and T. M. Nenoff, Journal of the American Ceramic Society **88**, 1812 (2005).
150 A. Tsoga, A. Gupta, A. Naoumidis, and P. Nikolopoulos, Acta Materialia **48**, 4709 (2000).
151 L. Vegard, Z. Physik **5**, 17 (1921).
152 A. Podpirka and S. Ramanathan, Journal of the American Ceramic Society **92**, 2400 (2009).
153 A. S. Nowick, A. V. Vaysleyb, and I. Kuskovsky, Physical Review B **58**, 8398 (1998).
154 X. D. Zhou, B. Scarfino, and H. U. Anderson, Solid State Ionics **175**, 19 (2004).
155 H. Hayashi, M. Kanoh, C. J. Quan, H. Inaba, S. Wang, M. Dokiya, and H. Tagawa, Solid State Ionics **132**, 227 (2000).
156 G. Kim, J. M. Vohs, and R. J. Gorte, Journal of Materials Chemistry **18**, 2386 (2008).
157 J. H. Joo and G. M. Choi, Journal of Power Sources **182**, 589 (2008).
158 M. Tsuchiya and S. Ramanathan, Applied Physics Letters **91** (2007).
159 R. Zallen, *The Physics of Amorphous Solids* (Wiley, 1998).
160 H. Scher and R. Zallen, The Journal of Chemical Physics **53**, 3759 (1970).
161 S. Horch, H. Lorensen, S. Helveg, E. Lægsgaard, I. Stensgaard, K. W. Jacobsen, J. K. Nørskov, and F. Besenbacher, Nature **398**, 134 (1999).
162 O. A. Marina and M. Mogensen, Applied Catalysis A: General **189**, 117 (1999).
163 E. P. Murray, T. Tsai, and S. Barnett, Nature **400**, 649 (1999).
164 B.-K. Lai, K. Kerman, and S. Ramanathan, Journal of Power Sources **196**, 6299 (2011).
165 Y. Takagi, B.-K. Lai, K. Kerman, and S. Ramanathan, Energy & Environmental Science **4**, 3473 (2011).
166 A. Kushima and B. Yildiz, Journal of Materials Chemistry **20**, 4809 (2010).
167 D. Marrocchelli, S. R. Bishop, H. L. Tuller, and B. Yildiz, Advanced Functional Materials **22**, 1958 (2012).
168 J. L. M. Rupp, Solid State Ionics **207**, 1 (2012).
169 I. Garbayo, A. Tarancón, J. Santiso, F. Peiró, E. Alarcón-Lladó, A. Cavallaro, I. Gràcia, C. Cané, and N. Sabaté, Solid State Ionics **181**, 322 (2010).
170 Q. Van Overmeere, K. Kerman, and S. Ramanathan, Nano Letters **12**, 3756 (2012).
171 H. L. Tuller, Solid State Ionics **131**, 143 (2000).
172 E. Mutoro, E. J. Crumlin, M. D. Biegalski, H. M. Christen, and Y. Shao-Horn, Energy & Environmental Science **4**, 3689 (2011).
173 K. Torsten and P. Oliver, Journal of Micromechanics and Microengineering **12**, 475 (2002).
174 J. Zaman and A. Chakma, Journal of Membrane Science **92**, 1 (1994).
175 R. W. Baker, Industrial & Engineering Chemistry Research **41**, 1393 (2002).

[176] U. Balachandran, B. Ma, P. Maiya, R. Mieville, J. Dusek, J. Picciolo, J. Guan, S. Dorris, and M. Liu, Solid State Ionics **108**, 363 (1998).
[177] T. Norby and Y. Larring, Solid State Ionics **136–137**, 139 (2000).
[178] P. N. Dyer, R. E. Richards, S. L. Russek, and D. M. Taylor, Solid State Ionics **134**, 21 (2000).
[179] M. A. Laguna-Bercero, Journal of Power Sources **203**, 4 (2012).
[180] H. D. Wiemhöfer and U. Vohrer, Berichte der Bunsengesellschaft für physikalische Chemie **96**, 1646 (1992).
[181] D. Wright, J. Thorp, A. Aypar, and H. Buckley, Journal of Materials Science **8**, 876 (1973).

APPENDIX

I've collected some worthwhile information that was used and developed during this thesis. While this Section is not exhaustive, I hope it will serve as a useful resource to assist any student or researcher working in a similar area. Some of the material in this Section resulted in unfinished projects; therefore I request that published work from this thesis (such as J. Mater. Res. 29, 320 (2014)) be kindly referenced for any procedure used.

MODELING PARAMETERS

The model discussed in Chapter 3 is based on a combination of electrochemical and physical relationships which require material properties. The table below summarizes the key values used in our model, which are fitted to experimental data from this thesis and in agreement with values in the literature.

Long name	**Symbol**	**573 K**	**673 K**	**773 K**
Ionic conductivity (S/cm)	σ_i	$7x10^{-6}$	$7x10^{-5}$	$1.75x10^{-4}$
Charge transfer coefficient	α	0.29	0.37	0.46
Exchange current density (A/cm^2)	j_0	$1.9x10^{-5}$	$8.8x10^{-5}$	$2.9x10^{-4}$
Effective mass	m^*	$20m_e$	$20m_e$	$20m_e$
YDZ Dielectric constant	ε_d	50	52	55

The band gap and work function of YDZ is temperature and environment dependent, however, we have approximated it as constant in our calculations due to inconsistent reports and relatively minute changes in the outputs. The figure below briefly summarizes the structure used in the model, band gap and trap states, and an experimental sampling of the probability of encountering a detrimental defect for a given membrane area (160 x 160 μm).

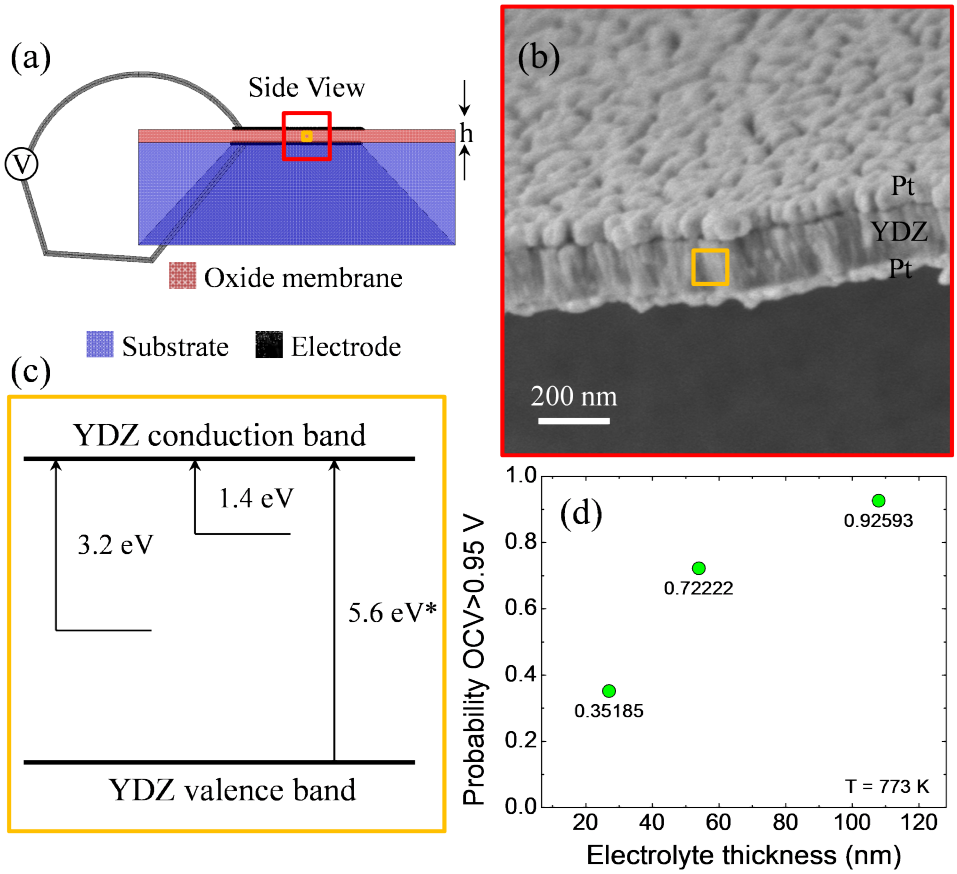

(a) *Schematic of experimental structures used to probe free standing oxide membranes used to demonstrate proof-of-concept thickness reduction of solid electrolytes into the sub-100 nm regime.* ***(b)*** *A cross-sectional scanning electron microscope image of a Pt|YDZ|Pt membrane structure depicting the nanoscale electrode spacing not previously considered.* ***(c)*** *A simplified band diagram for YDZ at 300 K based on experimentally determined optical trap states.*[97] *The band gap decreases with increasing temperature, though by less than 4% of its original value in the 300 – 773 K range.*[91] *As a note indicated by *, at 300 K the band gap of YDZ has been reported to be in the range 4.1 – 5.6 eV.*[91, 97, 180, 181] ***(d)*** *The experimentally determined probabilities (over 50 samples for each thickness) of measuring OCV of > 0.95 V at 773K using air and H_2 fuel in a Pt|YDZ|Pt heterostructure, which is a rough measure of the distribution of heterogeneous defects for a given membrane area.*

GENERAL MEMBRANE FABRICATION

1. Typically order DSP Si wafers with 200 nm LPCVD nitride deposited on both sides from University Wafer
2. Use CAD to create mask design and contact a certified mask writer in CNS
3. Transfer of design onto sample by photolithography
    a. Spin coat at 3000 RPM for 45 seconds and bake at 115°C for 120 seconds
    b. Using Süss Tech MJB-4 exposing tool, align mask, sample and expose (flood exposure) for 2.5 seconds
    c. Set up two beakers under hood; one for DI H_2O and one for 'CD-26' developer
        i. Remove weakened photo resist by placing sample in CD-26 solution for 60 seconds while gently shaking
        ii. After seeing pattern exposed, move to DI H_2O for rinse, then rinse with running DI H_2O
        iii. Dry with N_2 gun and then place on hot plate at 150°C for 120 seconds
4. Use south bay reactive ion etching (RIE) unit in CNS to etch away patterned Si_3N_4
    a. Place test piece of Si_3N_4 coated wafer into chamber and pump down in a similar fashion to prior steps
    b. Once below 40 mtorr, turn on switch for O_2 (flow control) and set at 1.2 SCCM (this will be 012 on the screen)
    c. Set CF_4 flow control at 15 SCCM (150 on screen)
    d. Adjust chamber pressure to 75 mtorr using the turbo pump valve on the left side
    e. Set RF power by pressing RF power, then adjusting the 2 front knobs to a FWD power (top) of ~100 W and reflected power (bottom) of <30 W
        i. Note: Using the FWD and reflected power outlined here will lead to ~100 nm/min etch rate

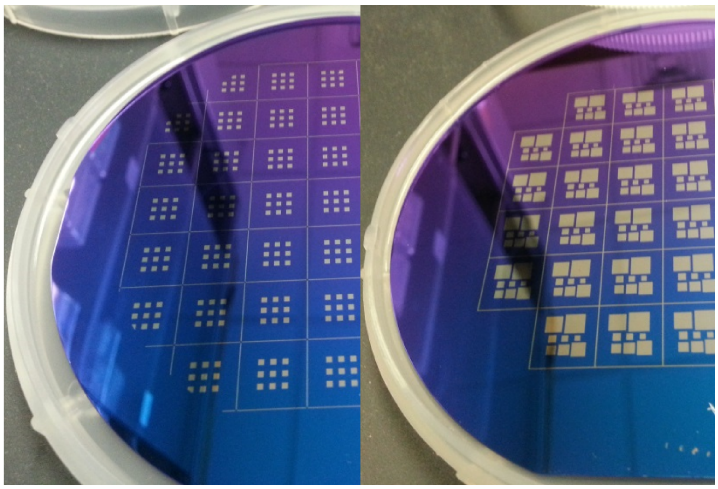

Example of backside patterned wafers after RIE.

5. Make 30 wt% KOH solution using KOH crystals

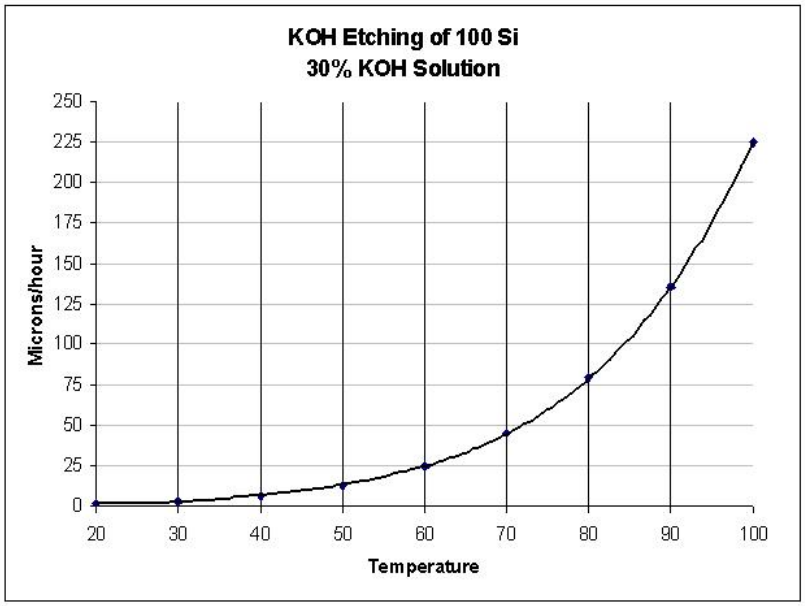

30 wt% KOH etch rate as a function of temperature.

a. When ~50 nm of Si is left in the membranes, remove the wafer and place in several water baths at temperatures higher than the KOH solution to clean the wafer
    i. After the last bath, rinse copiously with DI H_2O

b. Carefully cleave or cut wafer into individual pieces and use white O-rings (McMaster-Carr) to hold each piece
c. Place small samples into clean KOH solution to etch away the remaining Si and expose the nitride memory
    i. Watch samples closely during this step to ensure they do not interfere with one another and puncture memories
d. Once the pattern is clear on the polished nitride side, remove the samples through successive H_2O baths
e. Dry extremely quickly after boiling H_2O bath using a heat gun at 250°F (120°C)
f. Ensure there is no visible residue on the surface visually and with an optical microscope

6. Deposit films of interest
7. Use RIE to remove backside Si_3N_4 similar to step 3

Image of 1x1 cm chips with patterned windows. The left image shows free standing Si_3N_4 windows and the right shows release of the substrate supported for the oxide membrane. Note the color change on the backside and broken window.

LIFT-OFF PROCEDURE FOR PATTERNED STRUCTURES

1. Spin LOR3A (3000RPM/30sec), bake at 150 °C for 120 sec

2. Depending on your feature size, spin another layer LOR3A, bake again

- each layer of LOR3A should be ~300 nm under these conditions

3. Similar to previous procedure, spin S1813 (3000RPM/30sec), bake at 115 °C for 2min

4. Depending on feature lateral resolution (PL should go to about 1 μm features)

- Determine the proper dosage and exposure time. As a starting point, for a 20 um grid spacing, I used 3.6 s in MJB4

5. Develop 40sec in CD-26, but you may need to optimize for specific dose conditions. This will etch exposed S1813, but not LOR. Rinse copiously in DI H_2O and N_2 dry

6. Bake at 150 °C for 120 sec

7. Develop in CD-26, the exact time will depend on your undercut. For example 120 seconds works for a ~500 nm undercut. Rinse in DI H_2O and N_2 dry

8. Deposit the dense metallic grid using either sputtering or e-beam. For Pt both processes have good adhesion, but other metals may vary.

9. Liftoff the excess metallization using remover PG at 80 °C for at least 5 hours, typically leave overnight. Do not sonicate fine features! This will tear the edges (see below) and create rough interfaces.

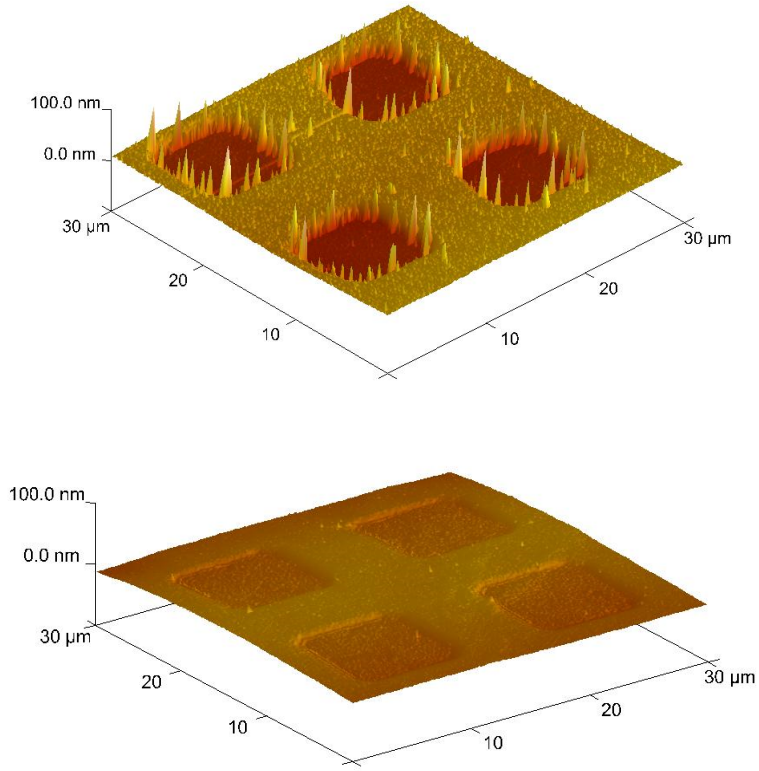

Example of bad lift off (top) and good lift off (bottom) using the grid procedure.

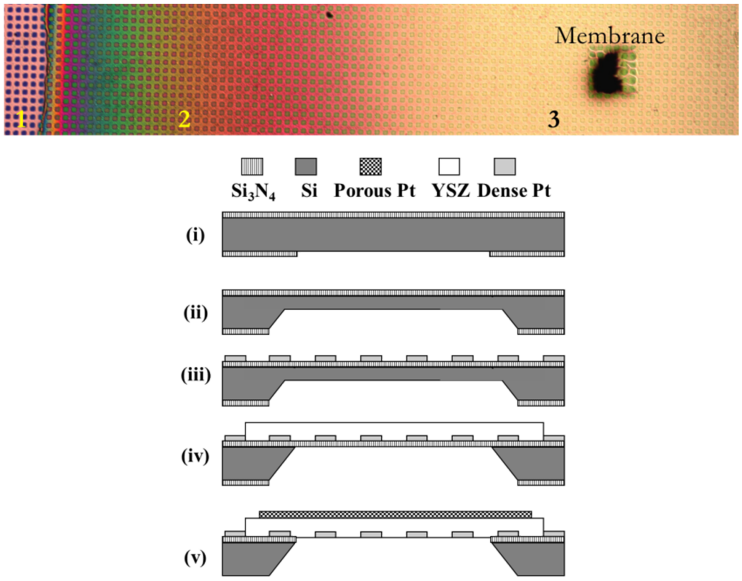

Example tri-layer grid structure micrograph (top) showing (1) dense Pt, (2) dense Pt grid covered by YDZ, (3) Pt-grid/YDZ/porous Pt; and schematic processing diagram (bottom).

KAPTON DRY ETCHING

DuPont recommends etching Kapton (type HN) using a wet chemical bath comprised of (by weight) (32) KOH, (400) Ethanol, and (100) water. Using this formulation softened the Kapton films into a 'gum' type state, but did not selectively etch. When using it with an additional adhesive used to bond Kapton to a support, a severe reaction was encountered. Therefore, a dry etching procedure was devised and is summarized below.

The work of G. Turban and M. Rapeaux, J. Electrochem. Soc. 130, 2231 (1983) was an excellent starting point for these trials.

Using the CNS south bay RIE system:

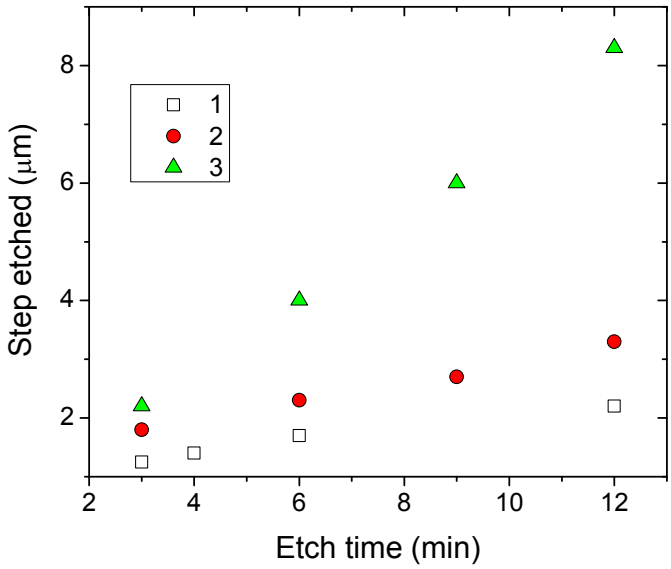

(1) *CF_4 flow rate: 15, O_2 flow rate: 12, total pressure: 100 mTorr, etch rate ~0.08 μm/min;* ***(2)*** *CF_4 flow rate: 20, O_2 flow rate: 100, total pressure: 100 mTorr, etch rate ~0.16 μm/min;* ***(3)*** *CF_4 flow rate: 12, O_2 flow rate: 100, total pressure: 200 mTorr, etch rate ~0.68 μm/min*

DRIE PROCESS FOR HIGH ASPSECT RATIO ETCH

(Developed by S. Xuza during senior thesis, please cite J. Electroceram. DOI: 10.1007/s10832-014-9917-1)

This process was made by using the DRIE at the MTL at MIT. There is a DRIE that is now functional in CNS, however, we did not get to work with this unit.

1. Coat DSP Si wafer with SPR 220 (3500 RPM/30 sec), bake at 115 °C for 60 sec
2. Expose pattern and develop with CD-26
3. Hard bake pattern at 110 °C for 30 minutes
4. Mount wafer on SOI handle wafer using a solution of CrystalBond and acetone (20/80 by weight). Cover the edges of the wafer using Kapton tape
5. DRIE (at MIT, using MTL facilities, unit STS-1) of Si using MIT-59 recipe
6. Isotropic etch SF6-14 recipe for 20 seconds at the end of each etch cycle. At end of DRIE process, leave ~100 μm for final processing
7. PR strip using Baker PRS 3000 at 80 °C for 30 minutes, rinse in IPA, then H_2O
8. Remove Bosch polymer on sidewalls using BOE (5:1) for 5 minutes
9. Dice the wafer and prepare for final etch
10. Global isotropic etch to smooth sidewalls and remove breaks using STS-1. Conditions (SF_6 180 sccm; O_2 18 sccm; coil power 600 W; plate power 30 W; pressure 13 mTorr; 5 minutes)
11. Final HNA etch to expose membranes. 2 minutes in $HF:HNO_3:CH_3COOH$ (2:7:1)

SELECTIVE TRIALS AT E-BEAM PATTERNING

This process was successful for obtaining a square grid with 300 nm squares with 300 nm spacing. As seen in the micrograph, the spacing is smaller than expected, due to the e-beam spreading below the resist surface and thereby exposing a larger area. Additional testing will likely be needed to get an advanced e-beam procedure. Write a pattern in CAD and convert to a GDS file before starting.

1. Spin EL9 at 4000 RPM for 40s
2. Bake 5 minutes at 180 °C
3. Spin 950 A4 at 4000 RPM for 40 seconds
4. Bake 5 minutes at 180 °C
5. Exposure with Raith 150 after SEM calibration and write field alignment
6. 400 μC/cm^2 with a step of 0.006 μm using the 20 μm aperture
7. Alternatively, 400 μm/cm2 at a step of 0.1 μm with the 120 μm aperture
8. Develop in MI-BK 123 for 60 seconds, then Isopropyl alcohol for 60 seconds, and gently rinse with DI H_2O
9. Metallize and remove resist with warm (40 °C) acetone overnight

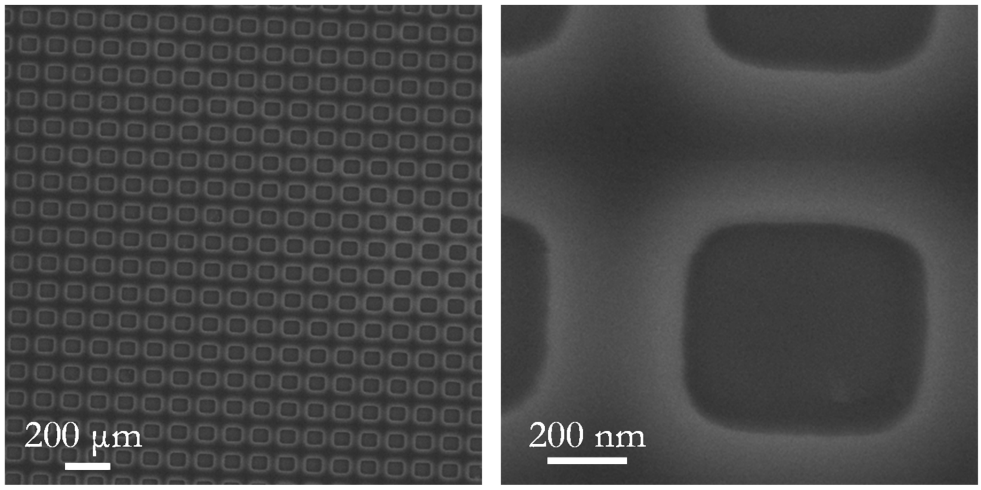

Example of a grid (not metalized) written with this procedure.

USEFUL DIAGRAMS AND TIPS

Using KOH to wet etch Si requires some simple calculation to determine what the size of a desired feature will be. The diagram below shows a schematic of the relevant directions and angles. In order to determine the side-length (L) of a square membrane fabricated in this way, the following expression is useful:

$$L_{BS} = L + 2t_s \tan(\theta)$$

Where L_{BS} is the backside side-length that should be patterned using lithography for a given Si wafer thickness (t_s). θ is the angle between <100> and <111> in radians. For example, in the case of a 500 μm thick (100) wafer, to achieve a front side membrane with L =200 μm, L_{BS} should be approximately 908 μm.

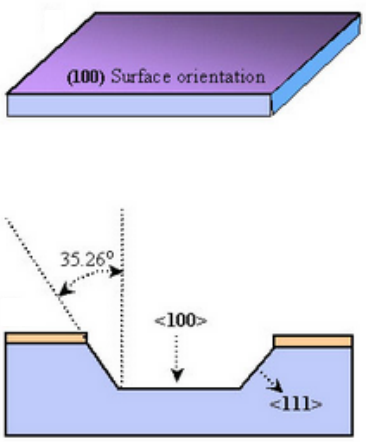

Final oxide membrane based devices fabricated in this way rely heavily on the etched structure and therefore, clean and repeatable processes are necessary for high performance.

Fuel cell test station

(Developed by A. Johnson during environmental fellowship, please cite J. Power Sources 186, 252 (2009))

This diagram is for reference if replacements or adjustments need to be made. All machining was done at the Rowland machine shop.

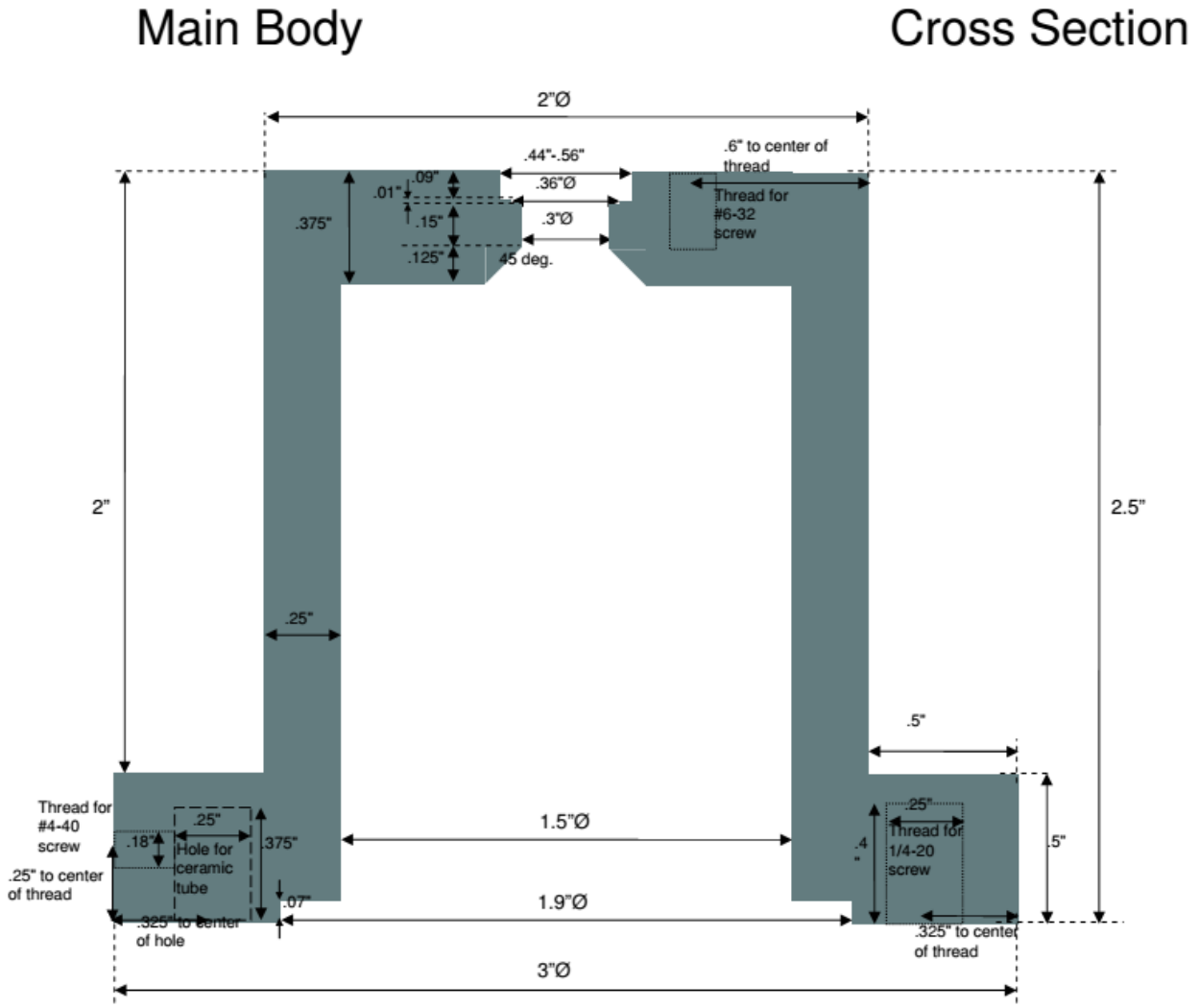

Main Body

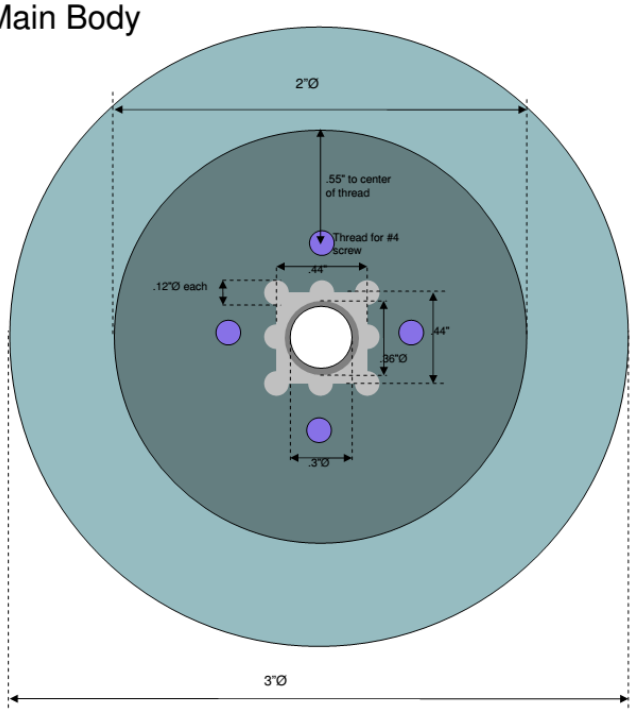

Top View

Main Body

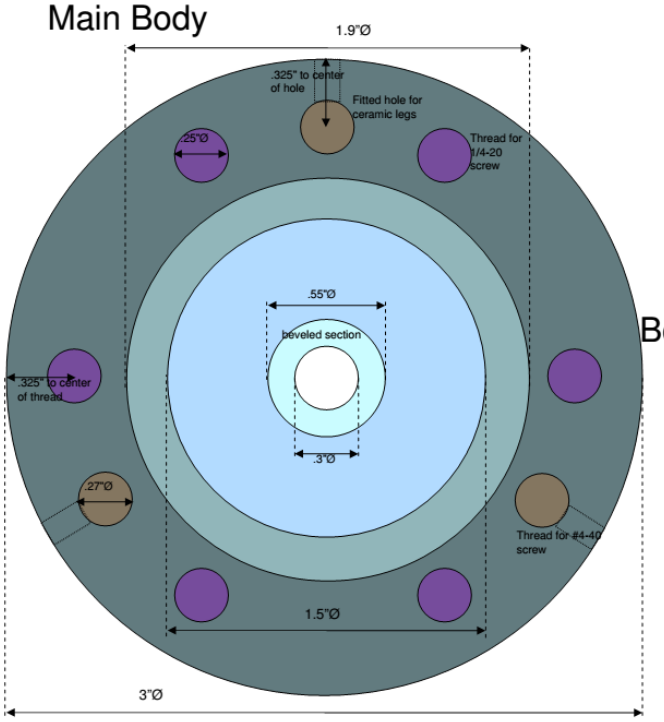

Bottom View

Porous Pt anode deposition

This discussion pertains to the deposition 'ideal' anodes for high performance. The conditions that worked well during this thesis were 75 mTorr Ar, 250 W target power, 8-10 minutes using CNS AJA-3. The deposition rate of Pt fluctuates as the target ages, so it is important to track the usage carefully. Additionally, note that the high pressure deposition will reduce the deposition rate dramatically, so it must be calibrated accordingly. Further, the deposition rate in the Si well (assuming a 160 μm square sample) is about half of that on a flat surface.

The figure below shows a nice summary of where an ideal microstructure could fall. All the images were taken after operation. If the anode is too thick (110 nm), there is no porosity and hence no TPBs and poor performance. If the anode is too thin (30 nm), there is a high amount of porosity, but the electrical conductivity at the membrane substrate interface is low because of bad perimeter coverage. An ideal anode microstructure sits somewhere between these extremes, having good porosity and adequate thickness to allow high currents to be driven out of the device.

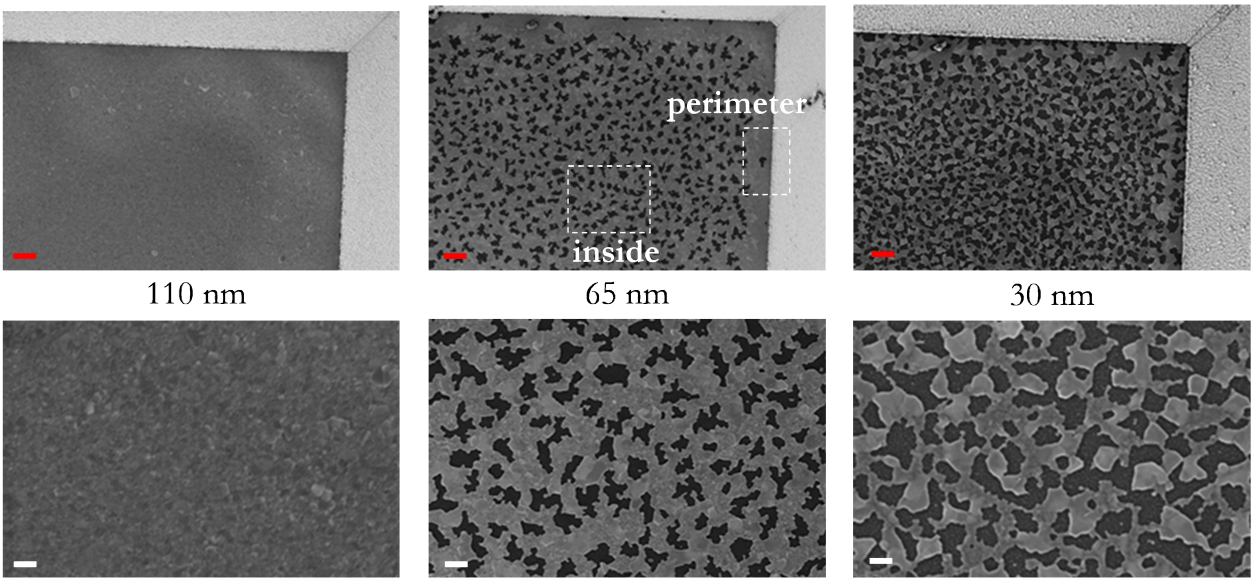

A depiction of the main issue with optimizing Pt in a well (wet etched Si) structure. The red and white scale bars represent 1 μm and 200 nm, respectively.

Thin film SOFCs with circular membranes made by DRIE was explored in the late stages of this thesis for high area utilization devices. The electrode complexities in this case are similar, but it is important to note that the physical shadowing effect from the tapered side wall is no longer in place. Thus, lower thicknesses are likely relevant for adequate porosity, however, the straight side walls make current collection difficult. I did not pursue this aspect in detail, but it will require some effort to get high performing devices at scale for such structures. There is some discussion and initial SOFC devices reported in J. Electroceram. DOI: 10.1007/s10832-014-9917-1 for reference.

PEER-REVIEWED PUBLICATIONS DURING PHD WORK

Performance of solid oxide fuel cells approaching the two-dimensional limit,

J. Appl. Phys. 115, 174307 (2014)

K. Kerman, S. Ramanathan

Free standing yttria-doped zirconia membranes: geometrical effects on stability,

J. Electroceram. DOI: 10.1007/s10832-014-9917-1 (2014)

K. Kerman, S. Xuza, S. Ramanathan

(Invited) Complex oxide nanomembranes for energy conversion and storage: A review,

J. Mater. Res. 29, 320 (2014)

K. Kerman, S. Ramanathan

Monolithic integration of nanoscale oxide membranes on polymeric scaffolds through stress control,

ACS Nano 7, 10895 (2013)

K. Kerman, Q. Van Overmeere, M. Karpelson, R.J. Wood, S. Ramanathan

Elastic configurations of self-supported oxide membranes for fuel cells,

J. Power Sources 222, 359 (2013)

K. Kerman, T. Tallinen, S. Ramanathan, L. Mahadevan

Nanoscale compositionally graded thin-film electrolyte membranes for low-temperature solid oxide fuel cells, Adv. Energy Mater. 2, 656 (2012)

K. Kerman, B.K. Lai, S. Ramanathan

Free standing oxide alloy electrolytes for low temperature solid oxide fuel cells,

J. Power Sources 202, 120 (2012)

K. Kerman, B.K. Lai, S. Ramanathan

Thin film nanocrystalline $Ba_{0.5}Sr_{0.5}Co_{0.8}Fe_{0.2}O_3$: Synthesis, conductivity, and micro-solid oxide fuel cells, J. Power Sources 196, 6214 (2011)

K. Kerman, B.K. Lai, S. Ramanathan

$Pt/Y_{0.16}Zr_{0.84}O_{1.92}/Pt$ thin film solid oxide fuel cells: Electrode microstructure and stability considerations, J. Power Sources 196, 2608-2614 (2011)

K. Kerman, B.K. Lai, S. Ramanathan

Thermopower in quantum confined La-doped $SrTiO_3$ epitaxial heterostructures,

Appl. Phys. Lett. 103, 173904 (2013)

K. Kerman, S. Ramanathan, M. Ishii, Y. Kotaka, H. Aso, K. Kurihara, R. Schafranek, A. Vailionis, J.D. Baniecki

Orientation dependent oxygen exchange kinetics on single crystal $SrTiO_3$ surfaces,

Phys. Chem. Chem. Phys. 14, 11953 (2012)

K. Kerman, C. Ko, S. Ramanathan

Natural gas powered thin film solid oxide fuel cells with nanoporous ruthenium anodes,

J. Power Sources 243, 1 (2013)

Y. Takagi, K. Kerman, C. Ko, S. Ramanathan

Energy storage in ultra-thin solid oxide fuel cells, Nano Lett. 12, 3756 (2012)

Q. Van Overmeere, K. Kerman, S. Ramanathan

Ultra-thin film solid oxide fuel cells utilizing un-doped nanostructured zirconia electrolytes,

J. Power Sources 213, 343 (2012)

C. Ko, K. Kerman, S. Ramanathan

Low temperature thin film solid oxide fuel cells with nanoporous ruthenium anodes for direct methane operation, Energy Environ. Sci. 4, 3473 (2011)

Y. Takagi, B.K. Lai, K. Kerman, S. Ramanathan

Methane-fueled thin film micro-solid oxide fuel cells with nanoporous palladium anodes,

J. Power Sources 196, 6299 (2011)

B.K. Lai, K. Kerman, S. Ramanathan

Nanostructured $La_{0.6}Sr_{0.4}Co_{0.8}Fe_{0.2}O_3/Y_{0.08}Zr_{0.92}O_{1.96}/La_{0.6}Sr_{0.4}Co_{0.8}Fe_{0.2}O_3$ (LSCF/YDZ/LSCF) symmetric thin film solid oxide fuel cells, J. Power Sources 196, 1826 (2011)

B.K. Lai, K. Kerman, S. Ramanathan

On the role of ultra-thin oxide cathode synthesis on the functionality of micro-solid oxide fuel cells: Structure, stress engineering and in-situ observation of fuel cell membranes during operation,

J. Power Sources 195, 5185 (2010)

B.K. Lai, K. Kerman, S. Ramanathan

Hall effect measurements on epitaxial $SmNiO_3$ thin films and implications for antiferromagnetism,

Phys. Rev. B 87, 125150 (2013)

S. Ha, R. Jaramillo, D.M. Silevitch, F. Schoofs, K. Kerman, J.D. Baniecki, S. Ramanathan